

FACULDADE DE ENGENHARIA DA UNIVERSIDADE DO PORTO



FEUP FACULDADE DE ENGENHARIA
UNIVERSIDADE DO PORTO

**Numerical simulation of the
reconstruction of mechanical
components using a Directed Energy
Deposition additive manufacturing
process**

Nuno Miguel Araújo Ferreira

Master in Mechanical Engineering

Supervisor: Prof. Marco Parente

Co-Supervisor: Prof. Abílio Jesus

October, 2022

Abstract

Additive manufacturing has gained increasing relevance in recent years. This manufacturing method is used to make prototypes, tools, and other fully functional products. This unconventional manufacturing process is an essential complement to existing traditional processes. Its appearance has changed the way engineering design is seen as it allows the production of components that would be impossible to produce using traditional manufacturing processes.

Within this new universe that is additive manufacturing, metal processing is currently at the forefront of this development. Due to process evolution and continuous improvements, these techniques are now capable of producing high-strength parts with good mechanical characteristics. On the other hand, some challenges still need to be overcome such as the high residual stresses produced, which can have a significant impact on fatigue characteristics and cause geometric distortions.

The use of numerical models is presented as a solution that allows for accurately and efficiently predicting the behavior of the parts. Computational simulation allows anticipating the residual distortions and stresses of a component however the simulation process presents several challenges and limitations that need to be overcome.

This dissertation uses numerical simulation software to study some additive metal manufacturing technologies, namely the Powder Bed Fusion process and the Directed Energy Deposition process. Abaqus was the software used to simulate these processes. Abaqus has an Additive Manufacturing - AM module, an interface that allows the user to prepare complex additive manufacturing simulations. The achievement of results for the prediction of distortions and residual stresses is achieved through a thermomechanical analysis of finite elements. These manufacturing technologies are characterized by the high number of parameters that influence numerical simulation, so one of the objectives was to try to understand the influence of some of these parameters.

At an early stage, the focus of this dissertation was the study of a benchmark bridge, obtained by the Powder Bed Fusion process. A comparison was made between the numerical and experimental data related to residual stresses and the deflection of the benchmark bridge when gradually removing in simulation finite element method the part from the substrate, allowing us to conclude the accuracy of the developed model.

The GEAR3D project consists of the 3D reconstruction of large gear teeth for the wind power sector, via direct laser deposition, ensuring mechanical properties equal to or greater than those of the new components. Within this project, a parametric study was carried out to evaluate the influence on the numerical results of residual stresses and distortion, for a given gear specimen.

Keywords: Additive manufacturing, Powder Bed Fusion, Directed Energy Deposition, Residual Stresses

Resumo

O fabrico aditivo tem ganho nos últimos anos cada vez mais relevância. Este método de fabrico é utilizado para fazer protótipos, ferramentas e outros produtos totalmente funcionais. Este processo de fabrico não convencional apresenta-se como um complemento essencial aos processos tradicionais existentes. O seu aparecimento alterou a forma como o design de engenharia é perseguido uma vez que permite a produção de componentes que seriam impossíveis de produzir utilizando os processos tradicionais de fabrico.

Dentro deste novo universo que é o fabrico aditivo, o processamento de metais encontra-se atualmente na vanguarda deste desenvolvimento. Devido à evolução do processo e a melhorias contínuas, estas técnicas são agora capazes de produzir peças de alta resistência e com boas características mecânicas. Por outro lado, alguns desafios ainda precisam de ser ultrapassados como as elevadas tensões residuais produzidas, que podem ter um impacto significativo nas características de fadiga e causar distorções geométricas.

A utilização de modelos numéricos apresenta-se como uma solução que permite prever com precisão e eficiência o comportamento das peças. A simulação computacional permite antecipar as distorções e tensões residuais de um componente, no entanto, o processo de simulação apresenta vários desafios e limitações que precisam de ser ultrapassados.

O objetivo desta dissertação é utilizar um software de simulação numérica para estudar algumas das tecnologias de fabrico aditivo de metal, nomeadamente o processo de Powder Bed Fusion e o processo de Direct Energy Deposition. O Abaqus foi o software utilizado para simular estes processos. O seu módulo de Additive Manufacturing – AM possui uma interface que permite ao utilizador uma adaptação mais rápida. A obtenção de resultados para a previsão das distorções e tensões residuais é conseguida através de uma análise termo-mecânica de elementos finitos. Estas tecnologias de fabrico são caracterizadas pelo elevado número de parâmetros que influenciam a simulação numérica, por isso um dos objetivos foi tentar entender a influência de alguns desses parâmetros.

Numa fase inicial o foco desta dissertação foi o estudo de benchmark recorrendo a uma geometria de ponte, obtida pelo processo de Powder Bed Fusion. Foi realizada uma comparação entre os dados numéricos e experimentais relativos às tensões residuais e à deflexão da benchmark bridge quando se remove gradualmente parte do substrato, permitindo tirar conclusões quanto à precisão do modelo desenvolvido.

O projeto GEAR3D consiste na reconstrução 3D de dentes de engrenagens de grande dimensão para o setor eólico, via deposição direta por laser, garantindo propriedades mecânicas iguais ou superiores às dos componentes novos. No âmbito deste projeto foi realizado um estudo paramétrico para avaliar a influência nos resultados numéricos das tensões residuais e da distorção, através da simulação de elementos finitos para determinadas especificações de engrenagem.

Keywords: Powder Bed Fusion, Direct Energy Deposition, Tensões Residuais

Acknowledgements

First and above all, I would like to thank the supervisor of this dissertation, Professor Marco Parente for providing me with all of the necessary support and guidance in this project, allowing me to conduct such interesting and innovative work.

Moreover, I would also like to thank the co-supervisor of this dissertation, Professor Abílio Jesus for his expertise and advice, as well as his interest in this project and follow-up on the developed work.

To Engineer Jorge Gil from INEGI, for giving me access to the specifications of the gears used in the scope of the GEAR3D project.

To Engineer Maria Vila Pouca who kindly gave me the Python script to clean the Gcode file. To my friend Roberto Figueiredo for the precious help with the python programming language.

To Maria Pires for the work developed previously and which served as a basis for the initial phase of my thesis.

To my family, my parents, my sister, and my godson for all their support, encouragement, affection, and inspiration.

To my classmates, especially Ana Teixeira, for all the moments shared throughout these 5 years in good and bad times.

Finally, I want to thank my friends for their friendship, patience, and help in everything I needed throughout my life. My friends from Remelhe are the best.

*“A sabedoria significa uma visão global,
um olhar de conjunto que abarque não apenas a parte,
mas a completude;
não apenas o que fomos,
mas o que somos e seremos.
A sabedoria é uma narrativa capaz de conter o nosso nascer,
o nosso maturar e o nosso morrer,
essa espécie de sofreguidão e paz, de delícia e dor,
essa singular poeira enamorada que a vida constitui. ”*

José Tolentino Mendonça

Contents

1	Introduction	1
1.1	Objectives	1
1.2	Outline	2
1.3	GEAR3D Project	2
2	State of the Art	5
2.1	Additive Manufacturing	5
2.2	AM Process description	6
2.2.1	Development phase	7
2.2.2	Production phase	8
2.2.3	Post-processing phase	8
2.3	Classification	10
2.4	Metal Additive Manufacturing	11
2.4.1	Powder Bed Fusion - PBF	12
2.4.2	Directed Energy Deposition - DED	14
2.4.3	Metal AM Applications	16
2.5	Finite Element Method - FEM	21
2.5.1	Introduction	21
2.5.2	Eigenstrain-Based Simulation	22
2.5.3	Thermo-mechanical simulation	22
2.5.4	Software	31
2.6	Residual Stresses	32
2.6.1	Definition	32
2.6.2	Origin	32
2.6.3	Measuring Techniques	34
2.6.4	Residual Stresses in AM	35
3	Simulation Details and Methods	37
3.1	Introduction	37
3.1.1	Physical specimens	37
3.1.2	Material Definition	40
3.2	Simulations	45
3.3	Benchmark Test AMB2018-01	45
3.3.1	Modeling	45
3.3.2	Initial Conditions	46
3.3.3	Mesh - Bridge	46
3.3.4	Progressive Element Activation	47
3.3.5	Scanning Strategy	48
3.3.6	Cooling	51

3.3.7	Postprocessing Simulation	51
3.4	Gear Simulation	52
3.4.1	Modeling	52
3.4.2	Mesh	53
3.4.3	Scan Strategy	54
3.4.4	Preheat Temperature	55
3.4.5	Time step influence	55
3.4.6	Material	56
4	Results and Discussion	57
4.1	NIST - Benchmark Bridge	57
4.1.1	Elastic strain	57
4.1.2	Residual strain comparison between XRD, ND and simulation results . .	58
4.1.3	Deflection analysis	59
4.2	Gear - Parametric simulations	60
4.2.1	Mesh size	60
4.2.2	Scanning strategy	62
4.2.3	Preheat Temperature	64
4.2.4	Time step influence	67
4.2.5	Material	70
4.2.6	Deformation Factor	72
5	Conclusions	73
5.1	Results	73
5.2	Further Work	74

List of Figures

Figure 1.1	GEAR3D project co-financing	3
Figure 1.2	SERMEC Group logo	3
Figure 2.1	Conceptual Comparison between Subtractive and Additive Manufacturing [9].	6
Figure 2.2	Generic process of CAD to part, showing all stages [10].	7
Figure 2.3	AM process - Development phase [10].	8
Figure 2.4	AM process - Production phase [10].	8
Figure 2.5	AM process - Post-processing phase [10].	9
Figure 2.6	Post-processing processes: (a) Heat treatment; (b) Support removal; (c) Cleaning; (d) Sand blasting; (e) UV curing; (f) Machining; (g) Sintering; (h) Coating or infiltration; (i) Dyeing. [10].	10
Figure 2.7	Additive manufacturing for metal [10].	12
Figure 2.8	Powder bed Fusion based processes: (a) PBF schematic machine (b) EBM [13].	13
Figure 2.9	Directed Energy Deposition (DED): (a) Powder DED (laser source) [16] (b) Wire DED (E-beam source) [17].	14
Figure 2.10	Directed Energy Deposition (DED) process parameters diagram [19].	15
Figure 2.11	Summary of metal additive manufacturing processes, along with their commercial machine supplier names [20].	16
Figure 2.12	Additive Manufacturing in automotive industry - BeamIt [21].	17
Figure 2.13	Relativity - 3D printed rocket: (a) Stargate; (b) Rocket structure [22].	18
Figure 2.14	Dental Model application [23].	18
Figure 2.15	Orthopaedic implants: (a) Knee implant and (b) Tibial implant [24].	19
Figure 2.16	3D printed metal sculpture: (a) Klein bottle (b) Quintrino [25].	19
Figure 2.17	Optomec LENS solutions for components repair [26].	20
Figure 2.18	3d printing headphones [27].	21
Figure 2.19	Distortion due to eigenstrains in a two-layer additive manufacturing process.	23
Figure 2.20	Recoater or roller blade motion in a powder bed-type AM process [33].	28
Figure 2.21	Point, infinite line, and box toolpaths	29
Figure 2.22	Point Toolpath-Mesh Intersection	29
Figure 2.23	Infinite Line Toolpath-Mesh Intersection	30
Figure 2.24	Box Toolpath-Mesh Intersection: (a) Subsegment approach and (b) Subelement approach	30
Figure 2.25	Residual stresses classification: Type I macro-stresses, Type II intergranular stresses and Type III lattice stresses [51].	33
Figure 2.26	Residual stresses measuring techniques [53].	34
Figure 2.27	Thermal gradient mechanism inducing residual stresses [55].	35

Figure 2.28	Effects of residual stress: a) reduced fatigue properties due to internal stress, b) distortion upon base plate removal and c) potential for process errors due to plastic deformation [51].	36
Figure 3.1	Benchmark Bridge structure and EDM cut location.	38
Figure 3.2	Bridge dimensions (in millimetres) [2].	38
Figure 3.3	Gear to repair: (a) gear before repair; (b) gear after repair; (c) machined gear [4].	39
Figure 3.4	Gear dimensions (millimetres).	40
Figure 3.5	Benchmark Bridge (AMB2018-01): (a) Bridge (b) Build plate.	45
Figure 3.6	C3D8, Linear element 8-node brick.	46
Figure 3.7	Benchmark Bridge Mesh: (a) Bridge (b) Substrate.	47
Figure 3.8	Benchmark Bridge progressive activation.	47
Figure 3.9	Scanning strategies (a) unidirectional scan; (b) bi-directional/zigzag scan; (c) island scan [68].	49
Figure 3.10	Scanning strategies: (a) alternate hatches - single pass, (b) alternate hatches - two passes and (c) cross hatches - single pass [69].	49
Figure 3.11	Description of scan pattern strategy [2].	50
Figure 3.12	Scan Strategy - Bridge Benchmark.	50
Figure 3.13	Nist benchmark bridge - Upward Deflection.	51
Figure 3.14	Gear Modeling - (a) gear and tooth belonging to the two-part model (b) one-part model.	52
Figure 3.15	Gear Mesh: (a) Two parts model (discontinuous mesh); (b) One part model (continuous mesh).	53
Figure 3.16	Mesh variation: (a) Mesh-1 (b) Mesh-2 (c) Mesh-3.	53
Figure 3.17	Scanning strategy I: (a) 90° (b) 120°.	54
Figure 3.18	Scanning strategy II: (a) 90° (b) 60°.	54
Figure 3.19	Scanning strategy III: (a) 90° (b) 0°.	55
Figure 3.20	Gear repaired with different materials: (a) IN625 + 42CrMo4 steel (b) Maraging steel + 42CrMo4 steel.	56
Figure 4.1	Comparison of elastic strain results in the x-direction.: (a) Simulation result EE11 (b) Strain measurements from NIST	57
Figure 4.2	Comparison of elastic strain results in the x-direction.: (a) Simulation result EE33 (b) Strain measurements from NIST	58
Figure 4.3	Benchmark bridge - Simulation result of elastic strain z at z=10.75 [mm]	59
Figure 4.4	Benchmark bridge - Upward Deflection	60
Figure 4.5	Nist benchmark bridge - Deflection	60
Figure 4.6	CPU time mesh simulations	61
Figure 4.7	Results of the parametric study of the mesh size: (a) Residual Stresses (b) Spatial Displacement	62
Figure 4.8	Results of mesh variation - Residual Stress: (a) Mesh 1; (b) Mesh 2 and (c) Mesh 3	63
Figure 4.9	Results of mesh variation - Spatial displacement: (a) Mesh 1; (b) Mesh 2 and (c) Mesh 3	63
Figure 4.10	Results of the parametric study of the scan variation: (a) Residual Stresses (b) Spatial Displacement	64
Figure 4.11	Scan strategy - Residual Stress: (a) Scan 1 (b) Scan 2 (c) Scan3	65
Figure 4.12	Scan strategy - Spatial Displacement: (a) Scan 1 (b) Scan 2 (c) Scan3	65

Figure 4.13 Preheat temperature variation	65
Figure 4.14 Results of the parametric study of the preheat temperature variation: Residual Stresses	66
Figure 4.15 Results of the parametric study of the preheat temperature variation: Spatial Displacement	66
Figure 4.16 Preheat temperature - Residual Stress: (a) Ph-1 (b) Ph-2 (c) Ph-3 (d) Ph-4 (e) Ph-5	67
Figure 4.17 Preheat temperature - Spatial displacement: (a) Ph-1 (b) Ph-2 (c) Ph-3 (d) Ph-4 (e) Ph-5	67
Figure 4.18 Results of the parametric study of the step time variation: (a) Residual Stresses (b) Spatial Displacement	68
Figure 4.19 Time step influence - Residual Stress: (a) TS-1 (b) TS-2 (c) TS-3 (d) TS-4 (e) TS-5	69
Figure 4.20 Time step influence - Spatial displacement: (a) TS-1 (b) TS-2 (c) TS-3 (d) TS-4 (e) TS-5	69
Figure 4.21 CPU time in incrementation time simulations	69
Figure 4.22 Material influence in Residual Stress	70
Figure 4.23 Material influence in spatial displacement	71
Figure 4.24 Material influence simulation residual stresses results: (a) IN625 (b) IN625 with 42CrMo4 steel	71
Figure 4.25 Material influence simulation spatial displacement results: (a) IN625 (b) IN625 with 42CrMo4 steel	71
Figure 4.26 Material influence simulation residual stresses results: (a) Maraging Steel (b) Maraging steel with 42CrMo4 steel	72
Figure 4.27 Material influence simulation spatial displacement results: (a) Maraging Steel (b) Maraging with 42CrMo4 steel	72
Figure 4.28 Deformation Scale Factor: (a) 0; (b) 25; (c) 50; (d) 75; (e) 100	72

List of Tables

Table 2.1	Seven categories of additive manufacturing according to American Society for Testing and Materials (ASTM) [11].	11
Table 2.2	Characteristic features of SLM and EBM [13].	13
Table 3.1	Parameters used in the DED process of gear simulation.	39
Table 3.2	Chemical composition (wt%) of Inconel 625 [23].	40
Table 3.3	Latent heat properties [57].	41
Table 3.4	Thermo-physical properties of IN625 [57].	41
Table 3.5	Young's modulus of IN625 [57].	42
Table 3.6	Thermo-physical properties of Maraging Steel [60].	43
Table 3.7	Johnson-Cook Plasticity coefficients for Maraging Steel 300 [62].	43
Table 3.8	Chemical composition (wt%) of 42CrMo4 Steel [63].	44
Table 3.9	Thermo-physical properties of 42CrMo4 Steel [64].	44
Table 3.10	Johnson-Cook Plasticity coefficients for 42CrMo4 Steel.	44
Table 3.11	42 CrMo4 latent heat properties.	45
Table 3.12	Parameters used in the AM process of the benchmark bridge.	50
Table 3.13	Mesh parameters - Elements number and mesh size.	53
Table 3.14	Preheat Temperature influence.	55
Table 3.15	Time Step Influence.	56
Table 4.1	Mesh Results	61
Table 4.2	Scan Strategy Results	63
Table 4.3	Preheat Results	66
Table 4.4	Results of the step time variation	67

Acronyms

AM	Additive Manufacturing
CFD	Computational Fluid Dynamics
DED	Directed Energy Deposition
DLF	Directed Light Fabrication
DMD	Directed Metal Deposition
DMLS	Directed Metal Laser Sintering
EBM	Electron Beam Melting
EDM	Electrical Discharge Machining
FE	Finite Element
FEA	Finite Element Analysis
FEM	Finite Element Method
FFF	Fused Filament Fabrication
GUI	Graphical User Interface
INEGI	Institute of Science and Innovation in Mechanical and Industrial Engineering
LBMD	Laser-Based Metal Deposition
LENS	Laser Engineered Net Shaping
LFF	Laser Freeform Fabrication
LNES	Laser Engineered Net Shaping
ND	Neutron Diffraction
NIST	Nation Institute of Standards and Technology
PBF	Powder Bed Fusion
SLM	Selective Laser Melting
SLS	Selective Laser Sintering
WWW	<i>World Wide Web</i>
XRD	X-ray diffraction

List of Symbols

ρ	Material density
C_p	Specific heat capacity
T	Temperature
t	Time
Q	Internal heat generation
r	Relative reference coordinate
q	Heat flux
k	Temperature dependent thermal conductivity
ε	Surface emissivity
σ_b	Stefan–Boltzmann constant
T_s	Surface temperature of the workpiece
T_∞	Temperature ambient
h	Convective heat transfer coefficient
σ	Stress
C	Fourth-order elastic stiffness tensor
ε_e	Elastic strain
ε	Total strain
ε_p	Plastic strain
ε_T	Thermal strain
P	Piola-Kirchoff stress tensor
J	Determinant of the deformation gradient
F	Deformation gradient
E	Green-Lagrange Strain
D	Displacement gradient
I	Identity matrix
ε_{inh}	Inherent strain
D_s	Stress-strain matrix
B	Strain-displacement matrix
K	Stiffness matrix
f	Nodal force vector
u	Displacement vector

Chapter 1

Introduction

Framework and motivation

Additive manufacturing is a process by which components are fabricated directly from computer models by selectively curing, depositing or consolidating materials in successive layers. These technologies have traditionally been limited to the fabrication of models suitable for product visualization but, over the past decade, have quickly developed into a new paradigm called additive manufacturing. Now additive manufacturing is beginning to be used for the fabrication of a range of functional end-use components. In this review, the evolution of additive manufacturing from its roots in accelerating product development to its proliferation into a variety of fields is briefly discussed. Here, the focus is on some of the key technologies that are advancing additive manufacturing and present some state-of-the-art applications [1].

The urgent challenge of protecting our common home includes the concern of joining forces in the pursuit of sustainable and integral development. My motivation throughout this work was to try and respond to the great challenge of becoming more sustainable. The GEAR3D project - 3D reconstruction of large gear teeth via directed laser deposition aims at rebuilding large gear teeth used in the wind power sector. In addition to the technical objectives to be achieved, this project also aims at reducing scrap by increasing the useful life of the components.

1.1 Objectives

The objective of this dissertation is the numerical simulation of the mechanical behavior of components obtained by two distinct production methods.

The two distinct types of laser printing are the PBF - Powder Bed Fusion methodology and the DED - Directed energy deposition methodology. These technologies are the predominant ones, in the equipment currently available in Portugal. The use of numerical simulation tools, based on the finite element method, is an extremely important tool in the context of companies in the productive sector.

It is intended in this dissertation to simulate the process of production, cooling and structural loading of the AMB2018-01 Benchmark bridge from NIST [2]. Another objective is to conduct a thermo-structural study of gear repair with DED using the finite element method via Abaqus to understand the origins of residual stresses and the impact of different parameters.

For this parametric study, the following simulations will be performed:

- Mesh*: Convergence studies to choose a mesh that allows for obtaining accurate results with the lowest possible computational cost under user-defined parameters;

- Step Time*: The time step has a direct influence on the number of elements that are activated and therefore it is also an important parameter to be studied;

- Preheat temperature*: Study of the influence of different preheat temperatures;

- Scanning strategies*: Comparison of different laser scanning strategies to study the impact of this parameter on the residual stresses;

- Material*: The use of different materials has a direct influence on the residual stresses produced, hence the importance of its study.

1.2 Outline

The remaining Chapters of this work are summarised in this Section.

Chapter 2 - The processes studied are described and the fundamental concepts related to additive manufacturing and finite elements are also presented.

Chapter 3 - The geometry of the parts used in the simulations is presented and described, as well as the materials used, the process parameters, and other important aspects of the simulations.

Chapter 4 - The numerical solutions to the simulations presented in the previous chapter are shown and discussed.

Chapter 5 - The main conclusions on the obtained results are presented and suggestions for future work are also presented to better understand additive manufacturing.

1.3 GEAR3D Project

The project "GEAR3D: 3D reconstruction of large gear teeth via directed laser deposition" is co-financed by the European Regional Development Fund (ERDF), Figure 1.1. The GEAR3D project aims to develop a methodology for 3D reconstruction of large dimensioned case-hardened gear teeth, for the wind power sector, via directed laser deposition with inductive local heating, guaranteeing equal/superior mechanical properties to new components [3].



Figure 1.1: GEAR3D project co-financing

This project is the result of a challenge presented by SERMEC Group - Figure 1.2, a precision metalworking business that provides maintenance solutions for the wind power sector.

With the consortium mobilized looks of INEGI and the Faculty of Engineering of the University of Porto (FEUP), it mobilized to answer one of the sector's greatest challenges: increasing the useful life of wind turbine components, while maintaining comparatively high levels of quality and reliability, when compared to that of a new component [4].



Figure 1.2: SERMEC Group logo

The additive manufacture of metals by directed laser deposition will allow the rebuilding and repairing of gears in wind turbine systems, ensuring mechanical properties equal to - or even superior to - those of the repaired components.

The main objectives of this project are [3]:

1. Develop an integrated methodology for 3D reconstruction of large gear teeth;
2. Create a numerical model for thermomechanical simulation of directed laser deposition as a complementary predictive tool to support parameter definition and process optimization;
3. Study deposition strategies using two or more types of filler material to create gradient deposits, to ensure good adhesion between them and the substrate;
4. Exploit synergies of different material properties to obtain a repaired gear tooth with the required characteristics;
5. Development of test protocols to validate quality/reliability of gear repair.

This thesis constitutes a contribution to objective 2 above described.

Chapter 2

State of the Art

Since AM technologies have the ability to produce near-net shape components layer-by-layer using 3D computer aided design (CAD) model data, they have many advantages over conventional subtractive methods. AM could reform the manufacturing industry by reducing component lead time, material waste, energy usage and carbon footprint [5].

2.1 Additive Manufacturing

Definition & Process description

Additive Manufacturing is defined as a process whereby parts or components are directly built from a solid model using a heat source and filler material. The process involves slicing a solid model of the part into multiple layers, creating a toolpath to trace the individual layers, and then building the part layer by layer using the filler material in a computer-controlled automated machine. Since the process relies on material addition in each layer leading to the final part geometry, it is called an additive process. In contrast, a conventional machining process starts with a block of material and follows a material removal technique to create the final part geometry and therefore is called a subtractive process [6].

In the figure 2.1 it is possible to observe the comparison between the conventional machining process and the additive manufacturing process.

Additive Manufacturing (AM) is defined by the International Organization for Standardization (ISO) and by the American Society for Testing and Materials (ASTM) as a “process of joining materials to make parts from 3D model data, usually layer upon layer, as opposed to subtractive and formative manufacturing methodologies” [7].

Additive manufacturing is the formalized term for what used to be called rapid prototyping and what is popularly called 3D Printing. The key to how AM works is that parts are made by adding material in layers; each layer is a thin cross-section of the part derived from the original CAD data. The thinner each layer is, the closer the final part will be to the original. All commercialized AM machines to date use a layer-based approach, and the major ways that they differ are in the materials that can be used, how the layers are created, and how the layers are bonded to each

other. Such differences will determine factors like the accuracy of the final part plus its material properties and mechanical properties [8].

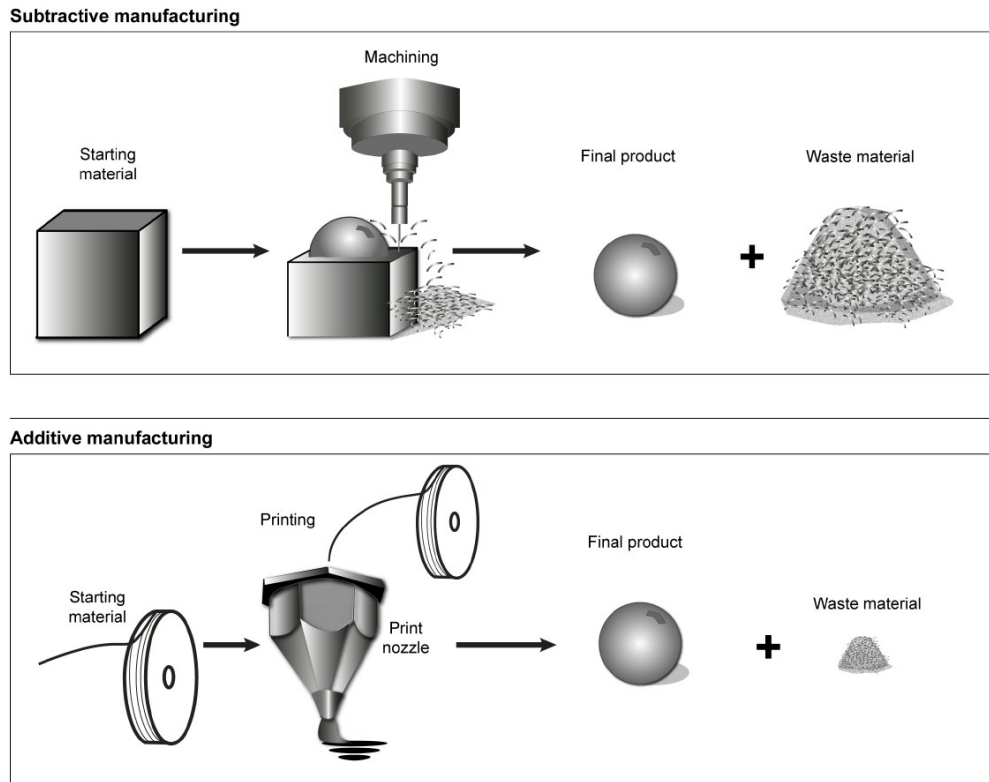


Figure 2.1: Conceptual Comparison between Subtractive and Additive Manufacturing [9].

2.2 AM Process description

Additive manufacturing involves a number of steps that move from the virtual CAD description to the physical resultant part. Different products will involve AM in different ways and to different degrees. Relatively simple products may only make use of AM for visualization models, while more complex products with greater engineering content may involve AM during numerous stages and iterations throughout the development process.

Early stages of the product development process may only require rough parts, with AM being used because of the speed at which they can be fabricated. At later stages of the process, parts may require careful cleaning and post-processing (including sanding, surface preparation, and painting) before they are used. Most AM processes involve, to some degree at least, the following nine steps as illustrated in Figure 2.2 [8].

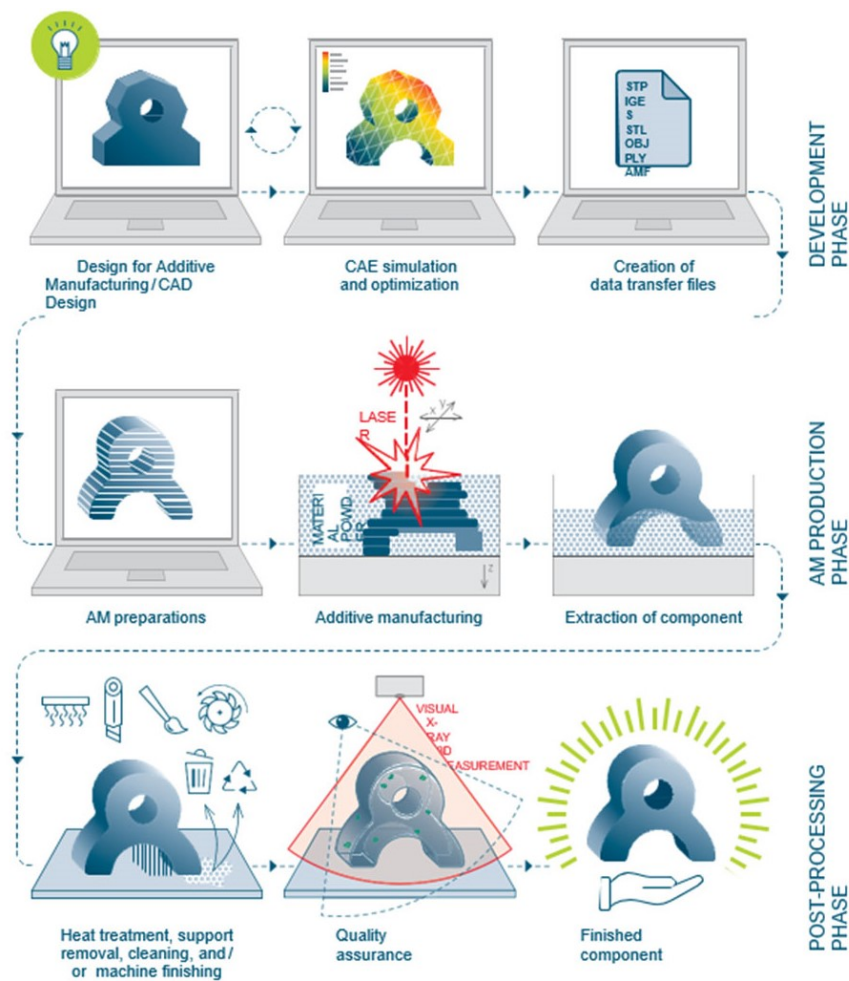


Figure 2.2: Generic process of CAD to part, showing all stages [10].

2.2.1 Development phase

During the development phase, Figure 2.3, additive manufacturing parts are modeled in a software model that creates a 3D solid or surface representation. Then this solid must be converted into STL file format, which has become a standard. This file describes the external closed surfaces of the original CAD model and forms the basis for the calculation of the slices [8].

In this phase, it is important to define the components and material properties that the AM component must-have. The material must be qualified or validated for the intended application. At this stage, it is also necessary to consider the specifics of the component and its influence on the design. It is also necessary to consider if a specific AM process is particularly well suited to the components in question.

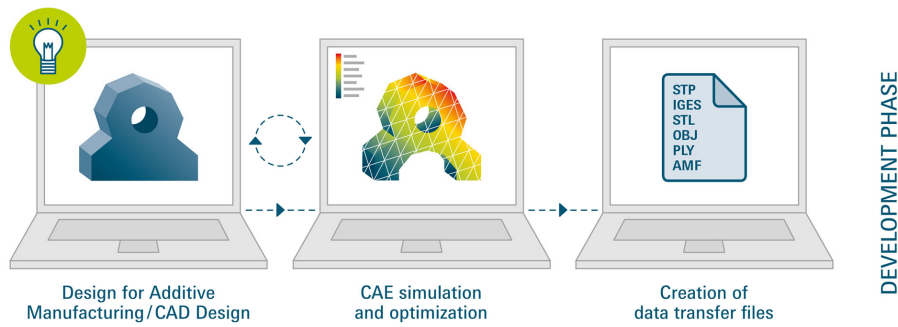


Figure 2.3: AM process - Development phase [10].

2.2.2 Production phase

In this phase, the AM machine must be properly set up prior to the build process. Such settings would relate to the build parameters like the material constraints, energy source, layer thickness, timings, etc. Building the part is mainly an automated process and the machine can largely carry on without supervision. Only superficial monitoring of the machine needs to take place at this time to ensure no errors have taken place like running out of material, power or software glitches [8].

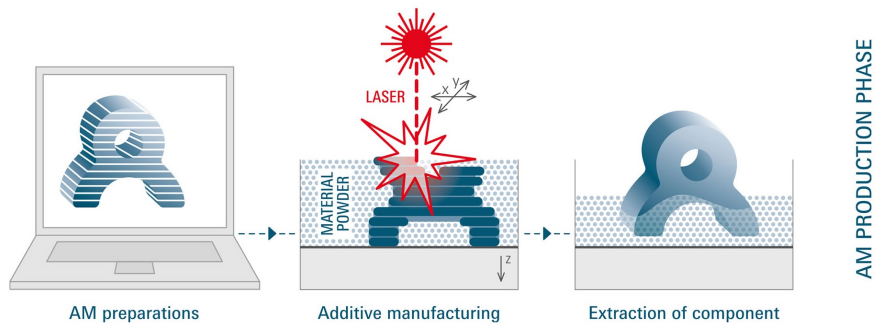


Figure 2.4: AM process - Production phase [10].

2.2.3 Post-processing phase

The amount of work involved in post-processing AM components, Figure 2.5 varies greatly depending on the application, material and process that have been used. Sometimes it can far outweigh the effort that went into the printing process itself. At the moment, a large proportion of the post-processing steps carried out after the actual printing process are manual, independent individual processes with a low level of automation. Some of these processes are described below [10].

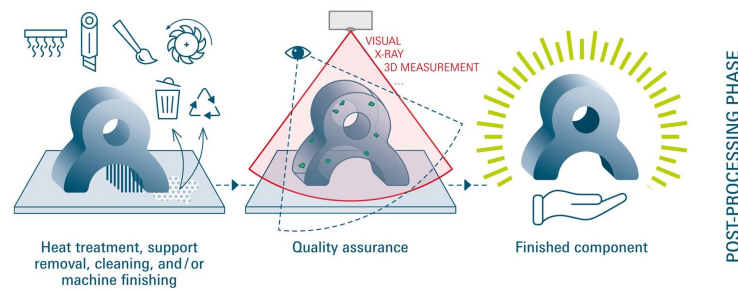


Figure 2.5: AM process - Post-processing phase [10].

Heat treatment: Figure 2.6 (a), usually follows the most common metal processes in order to relieve the internal stresses that is created by adding the layers. Only then are the components removed from their support.

Support removal: 3D components are attached to the corresponding base plates by scaffolding and support structures, Figure 2.6 (b), thus enabling overhanging structures to be created or reducing the degree of warp. These supports are then removed after the actual additive manufacturing process has been performed.

Cleaning: Components need to be thoroughly cleaned after additive manufacturing, Figure 2.6 (c). Excess material, such as metal powder or polymer powder, is therefore removed.

Sand blasting / Vibratory finishing: Normal cleaning is not sufficient for powder-based processes. Various blasting processes (such as sand blasting) or vibratory finishing processes serve to clean and, in particular, smooth the surfaces of the component, Figure 2.6 (d).

UV curing: Figure 2.6 (e) shows the components based on photopolymers that are exposed to UV light to fully cure them to achieve the ultimate material strength.

Machining: Machine post-processing, Figure 2.6 (f), can be done after practically all AM processes. It is absolutely essential for metal processes that are not really able to produce geometries that are close to the final contour.

Sintering: Some processes only produce what are known as "green" parts, or blanks. The component itself is not created until the sintering post-process is performed, Figure 2.6 (g). This method is always associated with considerable component shrinkage.

Coating or infiltration: Microporous components are infiltrated or coated with polymers to produce components that are completely gas-tight or liquid-tight, Figure 2.6 (h).

Dyeing: The visual appearance of powder based polymer components can be vastly improved with a dyeing post-processing step, Figure 2.6 (i).

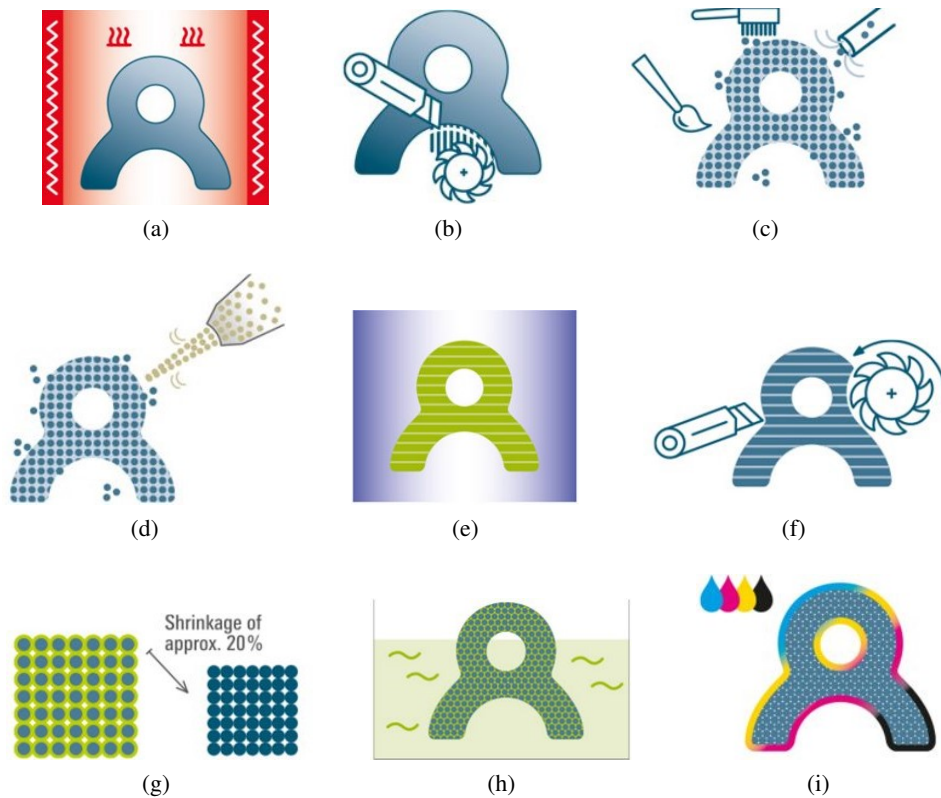


Figure 2.6: Post-processing processes: (a) Heat treatment; (b) Support removal; (c) Cleaning; (d) Sand blasting; (e) UV curing; (f) Machining; (g) Sintering; (h) Coating or infiltration; (i) Dyeing. [10].

2.3 Classification

With the evolution of Additive Manufacturing technologies, several terms were appearing. However, it is common for different terms to have the same meaning, therefore, a clear categorization is needed to correctly define and separate distinct processes. The ASTM terminology presents a suitable organization of AM process categories, terms, and nomenclature that can include the majority of existing technology and define it accordingly. It is, therefore, a useful reference when it comes to grouping AM technologies. The existing categories are described as follows:

Binder jetting (BJ): AM process that relies on a liquid bonding agent that is deposited selectively, joining powder-based material into consistent solid shapes;

Directed energy deposition: process that is based on fusing material, as it is selectively placed, by melting it with focused thermal energy;

Material Extrusion: additive process that consists on selective deposition of material through a nozzle or orifice;

Material Jetting: selective deposition of droplets of build material for additive manufacturing;








Powder Bed Fusion: process that relies on fusion of selected regions of a powder bed, using focused thermal energy;

Sheet Lamination: process consisting on bonding sheet-based material, in order to form a consistent object;

Vat Photopolymerization: AM process based on selective curing of a liquid photopolymer in a vat, by light-activated polymerization.

Only a few categories will be investigated for this project. As a result, because metal additive manufacturing will be the focus of the developed work, the directed energy deposition processes and powder bed fusion technology will be the most important categories.

Table 2.1: Seven categories of additive manufacturing according to American Society for Testing and Materials (ASTM) [11].

Categories	Technologies	Advantages/Drawbacks
	Vat-Photopolymerization	<ul style="list-style-type: none"> • High Building Speed • Good part resolution • Overcuring, scanned line shape • High cost for supplies and materials
	Material Jetting	<ul style="list-style-type: none"> • Multi-material 3d printing • High surface finish • Low-strength material
	Material Extrusion	<ul style="list-style-type: none"> • Inexpensive extrusion machine • Multi-material printing • Limited part resolution • Poor surface finish
	Binder Jetting	<ul style="list-style-type: none"> • Full-color objects printing • Require infiltration during post-processing • Wide material selection • High porosities on finished parts
	Powder Bed Fusion (PBF)	<ul style="list-style-type: none"> • High accuracy and details Fully dense parts • High specific strength • Powder recycling • Support and anchor structure
	Directed Energy Deposition (DED)	<ul style="list-style-type: none"> • High deposition rate compared to PBF process • Repair of damaged worn parts • Functionally graded material printing • Require post-processing
	Sheet Lamination	<ul style="list-style-type: none"> • High surface finish • Low material, machine, process cost • Decubing issues

2.4 Metal Additive Manufacturing

Metal working has played a key role in the development of human civilization. Metal is often hidden in nature and requires time, labor, and energy to extract and form into useful objects [12].

Plastic additive manufacturing has matured and 3D printers are being widely used in businesses, universities, and even consumers' homes, while metal additive manufacturing (MAM) is still in its early stages of development. MAM has the potential to revolutionize manufacturing scenario even surpasses its relative scenario because it is consistent in the use of expensive materials reducing material waste is even more urgent. The classification of metal additive manufacturing technologies is shown in Figure 2.7.

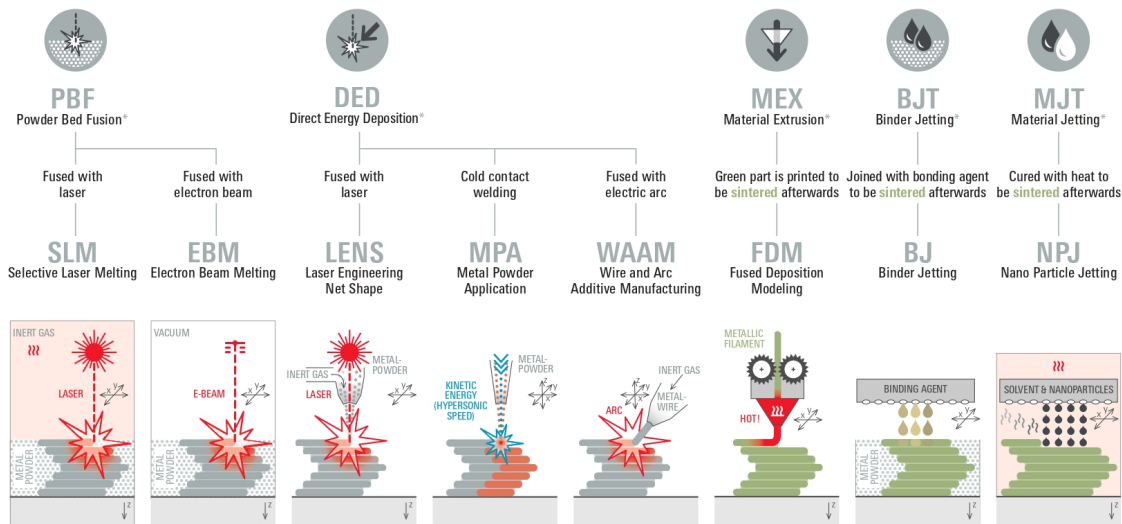


Figure 2.7: Additive manufacturing for metal [10].

2.4.1 Powder Bed Fusion - PBF

Powder bed fusion (PBF) processes were among the first commercialized AM processes.

All PBF processes share a basic set of characteristics. These include one or more thermal sources for inducing fusion between powder particles, a method for controlling powder fusion to a prescribed region of each layer, and mechanisms for adding and smoothing powder layers [8].

In the powder-bed fusion process, thin layers of powder are applied to a build plate, and an energy source (a laser or electron beam) is used to fuse the powder at locations specified by the model of desired geometry. When one layer is completed, a new layer of powder is applied and the process is repeated until a three-dimensional part is produced. The PBF process is alternatively known as selective laser sintering (SLS), selective laser melting (SLM), directed metal laser sintering (DMLS), directed metal laser melting (DMLM), and electron beam melting (EBM) [13].

A PBF machine, Figure 2.8 (a), requires a build substrate to give mechanical and thermal support to the build material. The substrate helps provide mechanical support because existing layers of the build must not move. The substrate also provides a thermal path to dissipate heat [14].

Figure 2.8 (b) show the Electron beam melting based process. As compared to the SLM system to EBM, in both processes residual stresses are developed. In EBM, high build chamber

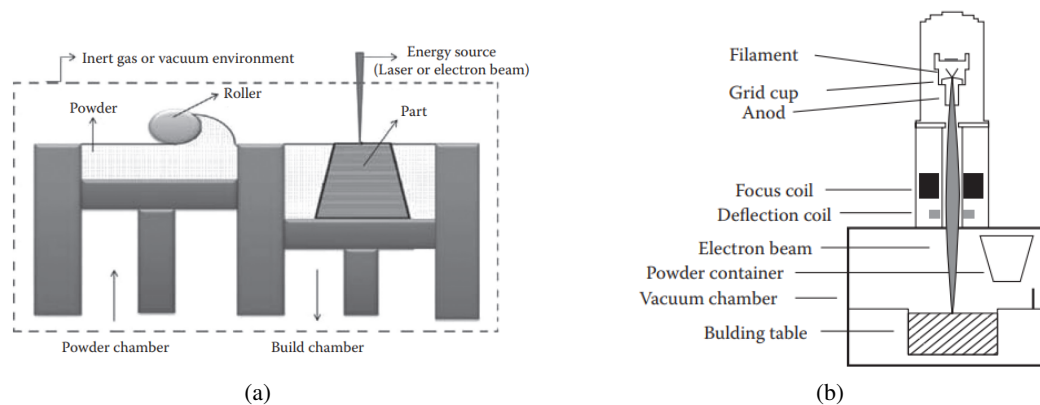


Figure 2.8: Powder bed Fusion based processes: (a) PBF schematic machine (b) EBM [13].

temperature is maintained by preheating the powder bed layer and the thermal gradient is reduced which reduces residual stresses in the part and eliminates postheat treatment required. In addition, entire EBM process takes place under vacuum, since it is necessary for the quality of the electron beam. Vacuum environment reduces thermal convection, thermal gradients, contamination and oxidation.

In SLM, part manufacturing takes place under argon gas environment for reactive materials to avoid contamination and oxidation, so it can be expected that EBM-manufactured parts have lower oxygen content than SLM-manufactured parts. In spite of having these advantages, EBM is not as popular as SLM because of its higher machine cost, low accuracy, and nonavailability of large buildup volumes [13].

Table 2.2: Characteristic features of SLM and EBM [13].

	SLM	EBM
Power source	One or more fiber lasers of 200–1000 W	High power electron beam of 3000 W
Build chamber environment	Argon or Nitrogen	Vacuum/He bleed
Method of powder preheating	Platform heating	Preheat scanning
Powder preheating temperature (°C)	100–200	700–900
Maximum build volume (mm)	500 × 350 × 300	350 × 380(Ø × H)
Maximum build rate (cm ³ /hr)	20–35	80
Layer thickness (µm)	20–100	50–200
Melt pool size (mm)	0.1–0.5	0.2–1.2
Surface finish (Ra)	4–11	50–200
Geometric tolerance (mm)	±0.05–0.1	0.2–1.2
Minimum feature size (µm)	40–200	100

Table 2.2 summarizes the characteristic features of the two processes, SLM and EBM.

2.4.2 Directed Energy Deposition - DED

This method is called directed energy deposition because the supply material is directed at the heat source, at the point of deposition. The utilized energy source can be laser, electron beam, or arc/plasma, as shown in Figure 2.9. Depending on the type of feedstock, a stream of metal powder is sprayed or a metal wire is pushed into the energy path. Then, the beam fires and creates a melt pool on the surface of the target plate to create the layer. After fusing multiple layers, a 3D solid metallic build is created [15].

Unlike powder bed fusion techniques, DED processes are not used to melt a material that is pre-laid in a powder bed but are used to melt materials as they are being deposited [8]. One of the most successful applications of DED is repairing metal parts by adding material to damaged components such as turbine blades.

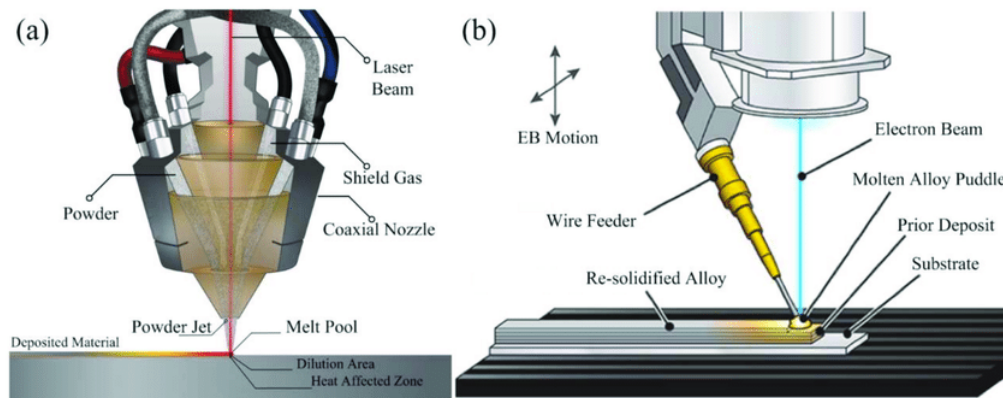


Figure 2.9: Directed Energy Deposition (DED): (a) Powder DED (laser source) [16] (b) Wire DED (E-beam source) [17].

A number of organizations have developed DED machines using lasers and powder feeders. These machines have been referred to as Laser Engineered Net Shaping (LENS), Directed Light Fabrication (DLF), Directed Metal Deposition (DMD), 3D Laser Cladding, Laser Generation, Laser-Based Metal Deposition (LBMD), Laser Freeform Fabrication (LFF), Laser Directed Casting, LaserCast, Laser Consolidation, LasForm, and others. Although the general approach is the same, differences between these machines commonly include changes in laser power, laser spot size, laser type, powder delivery method, inert gas delivery method, feedback control scheme, and/or the type of motion control utilized [8].

Processing variables in DED

The DED process has many processing variables; this process employs a focused heat source in the form of a laser beam, electron beam, or plasma/electric arc.

Thus, samples prepared using a DED process undergo repeated thermal cycling and very high melt pool cooling rates, resulting in fine, out-of-equilibrium microstructures with high residual stresses and, in some cases, cracking [18].

The process parameters influencing the deposited material in blown-powder DED processes are classified into three major branches, Figure 2.10:

1. System specifications,
2. Feedstock parameters,
3. Deposition variables.

The complex thermal history and the large number of processing parameters listed in Figure 2.10 make fully characterizing and studying each parameter's effect on the as-deposited material difficult. The DED process is highly dependent on the chemical composition, melting temperature, thermal conductivity, reflectivity, specific heat capacity, melt viscosity, melt surface tension, and spectral emissivity of the powder feedstock material [19].

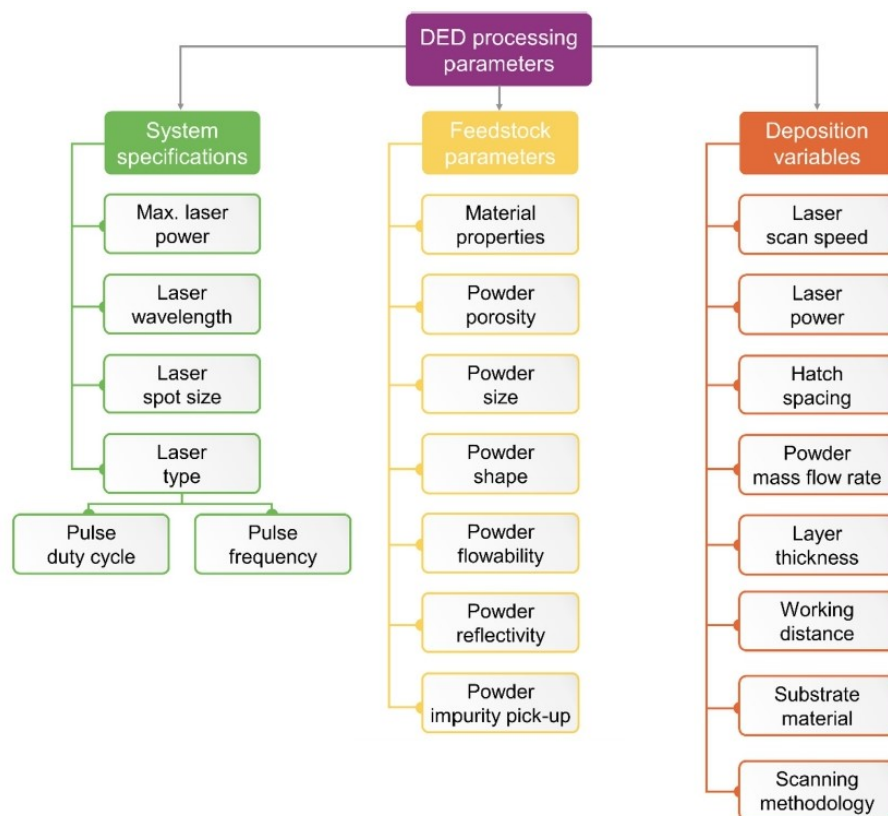


Figure 2.10: Directed Energy Deposition (DED) process parameters diagram [19].

Recent reviews of metal AM processes highlight some of the differences between the various processes. Figure 2.11 depicts the two major metal AM process categories discussed in this thesis: powder bed fusion (PBF) and directed energy deposition (DED), as well as the names of the commercial machine suppliers [20].

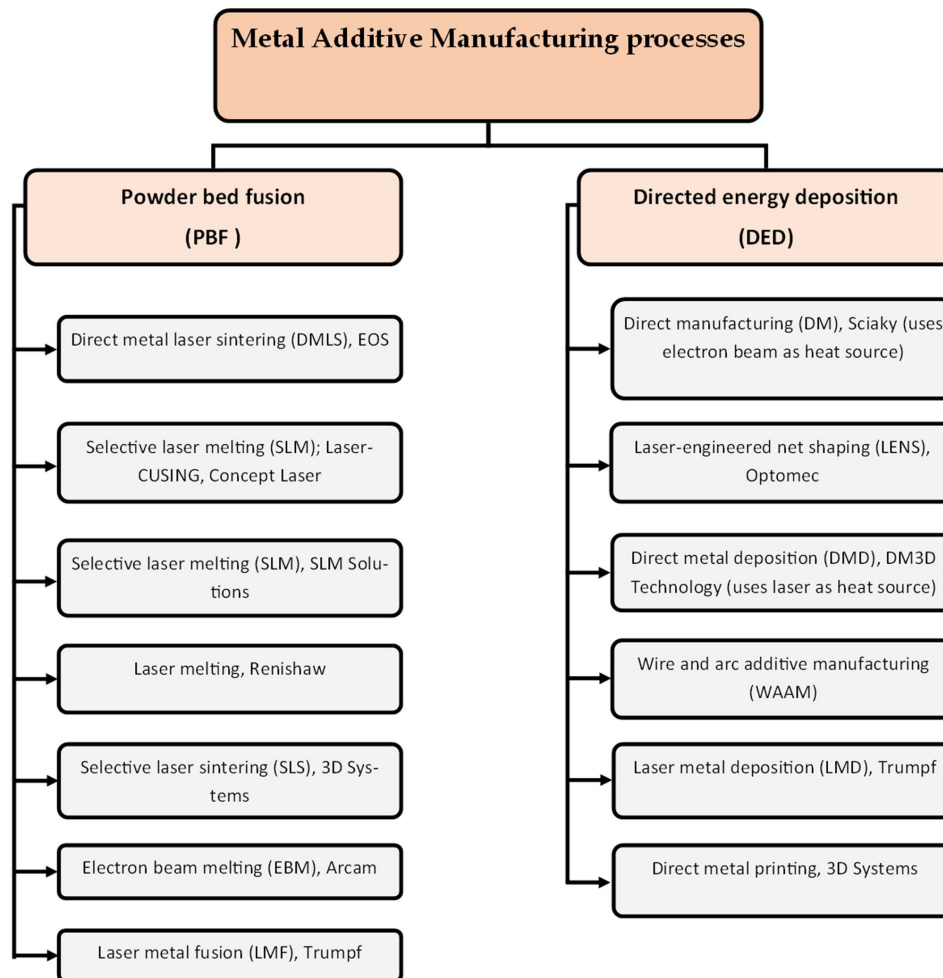


Figure 2.11: Summary of metal additive manufacturing processes, along with their commercial machine supplier names [20].

2.4.3 Metal AM Applications

Automotive

3D printing technologies have a very important role in the automotive industry, especially in the Motorsport sector. Formula 1 was one of the first to use 3D-printed components to keep up with continuously evolving technologies and the innovations needed race after race. This new technology can contribute to pushing cars to their limits and creating faster, lighter, and stronger cars. Selective Laser Sintering (SLS) and Directed Metal Laser Sintering (DMLS) are the two most common additive manufacturing methods in Formula 1, these methods allow for ultra-rapid prototyping, high precision, low weight, and part creation in complex shapes.

Figure 2.12 shows an AM printed exhaust manifold for the Motorsport sector. This sector was one of the first to use 3D-printed components to create complex designs for innovative components without limiting their inventive ingenuity. Time is a key factor in Motorsport, leaving little time



Figure 2.12: Additive Manufacturing in automotive industry - BeamIt [21].

available for optimizing vehicle performance. Conventional technologies require six months to produce a component. On the other hand, with additive technology, it is possible to produce new components in just two or three weeks.

Aerospace

Among the first to invest in Additive Manufacturing, the Aeronautical industry benefits vastly from this technology's potential, and the potential reduction in fabrication lead times and costs provides strong motivation for evaluating the AM technology.

Space and aerospace applications require strict procedures and certification for processes and components. Significant savings may be realized in reducing the number of certified parts and processes, such as joining, used to produce a component. The weight reduction can result in significant savings during the launch into space escaping the gravity well of earth or fuel-saving during commercial aircraft flights. Reducing material waste during the fabrication of expensive specialty materials such as nickel-based alloys or titanium is also an important factor in justifying the use of additive manufacturing [12].

Figure 2.13 shows the world's first entirely 3D printed rocket, Terran 1, that is entirely designed, built, and flown by Relativity Space, Inc. (Relativity). Relativity use a 3D printing platform that vertically integrates artificial intelligence, robotics and patented autonomous manufacturing technology. This company utilizes two types of 3D printing to produce over 90% of the dry mass of Terran 1. Relativity's large format, proprietary 3D printing process, known as Stargate 2.13 (a), is used to produce primary and secondary structures for Terran 1 from aluminum alloy. Stargate can currently print structures up to 3.4 meters diameter by 7.6 meters tall—the world's largest metallic printed parts. Relativity uses directed metal laser sintering (DMLS) to produce geometrically small, high fidelity components 2.13 (b) [22].



Figure 2.13: Relativity - 3D printed rocket: (a) Stargate; (b) Rocket structure [22].

Medical

“Disruptive” applications for AM are beginning to emerge into the manufacturing mainstream. One such application is that of dental devices, where small custom-fit crowns and dental implants are disrupting the historic methods for the fabrication of these components. Figure 2.14 shows dental crowns and bridges produced by directed metal laser sintering (DMLS). Small lot size, high precision and high value products such as these are seeing wide adoption [12].



Figure 2.14: Dental Model application [23].

Another example of medical applications is orthopedic implants. Conventional orthopedic knee and hip implants fixed with acrylic cement have produced excellent results in older patients, less success is generally achieved for younger, more active individuals. As alternatives to acrylic cement porous scaffolds because have exhibited considerable potential because promoting bone cell ingrowth for implant stabilization. The electron beam melting (EBM) technique has recently illustrated not only the potential for fabricating complex, porous, monolithic implant components but also the prospect of fabricating patient-specific implant components [24]. Figure 2.15 shows two biomedical implants built with a Co-29Cr-6Mo alloy - (a) and Ti-6Al-4V alloy - (b) using EBM technology.

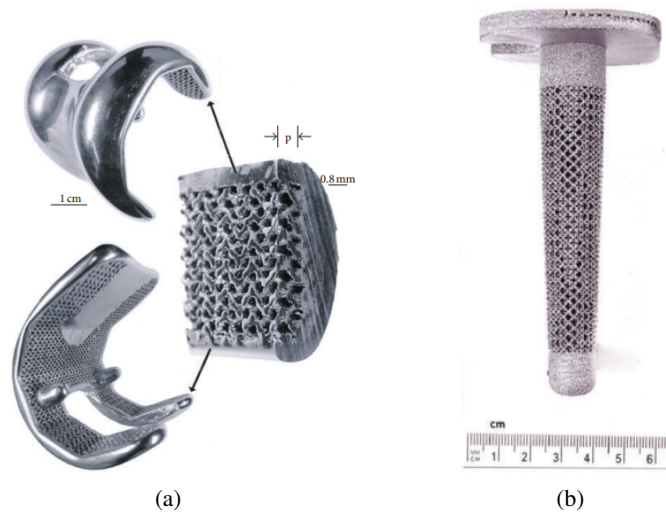


Figure 2.15: Orthopaedic implants: (a) Knee implant and (b) Tibial implant [24].

Artistic

Artistic applications of 3D metal printing are leading the way toward the exploration of entirely new designs, shapes, and processes. Artists stretch the boundaries of design with 3D printing in mind. Some of these capture the essence of freeform, emotional design. Complex and delicate geometric designs, not possible through traditional methods, enable artists to offer unique and bespoke creations. A design and part by Bathsheba Sculpture is one example, shown in Figure 2.16 [12].

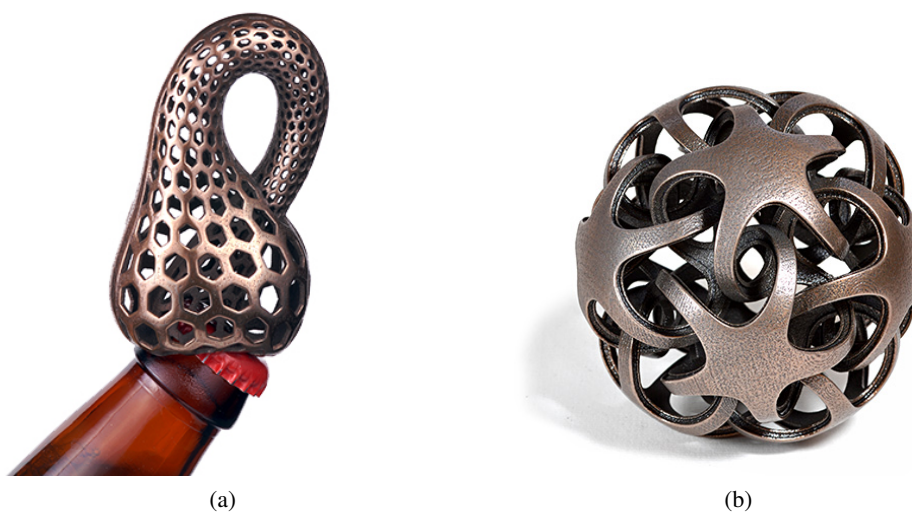


Figure 2.16: 3D printed metal sculpture: (a) Klein bottle (b) Quintrino [25].

Repair Industry

Optomec is an American company that works in the branch of additive manufacturing technology. The two technologies offered by Optomec are Aerosol Jet and LENS precision.

Aerosol Jet systems have the unique capacity to print very accurate features and electrical, structural, and biological patterns on practically all substrates.

The LENS (Laser Engineered Net Shaping) system is a cost-effective process that can fabricate in hands and repair high-value metal components. This technology enables customers to not only print full 3D parts but also to add materials to existing 3D parts that were produced using conventional manufacturing methods. The repair of high-value metal components is essential for maximizing part lifetime, reducing operating costs, and helping maintain a high level of readiness. Repair methods that add material to worn or damaged areas require exceptional process control and outstanding material quality [26].

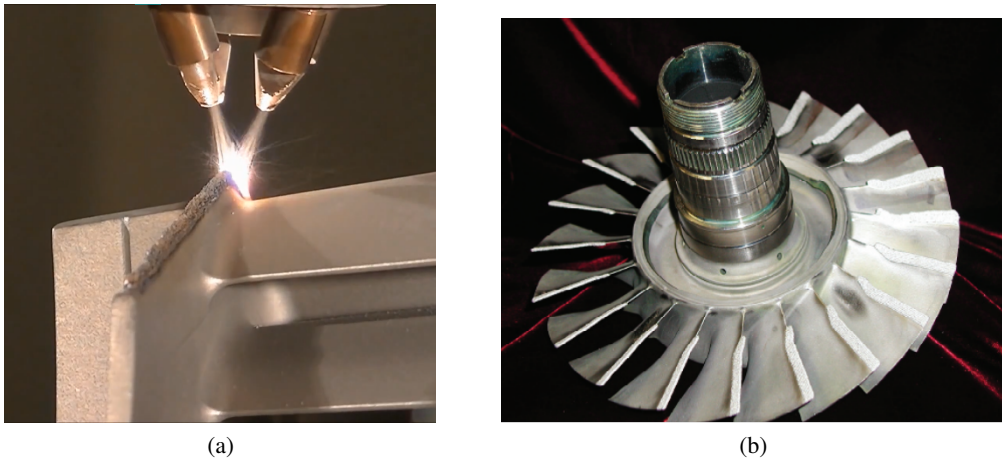


Figure 2.17: Optomec LENS solutions for components repair [26].

Other Applications

Sennheiser Headphones

To achieve a unique sound experience, the Sennheiser company developed a headphone that was fabricated using metal-powder-based 3D printing that can create any shape imaginable within tight tolerances. This headphone is made with zirconium alloy that has triple the hardness and flexural strength of high-performance steel. Shock-frozen during manufacturing, amorphous metals never have a chance to form a crystalline structure like conventional metals. The result is a lustrous, satiny surface that is extraordinarily resistant to corrosion and scratches. Chambers and channels form as part of this additive manufacturing process with no milling required. However, cost does limit the potential applications of this new material [27].

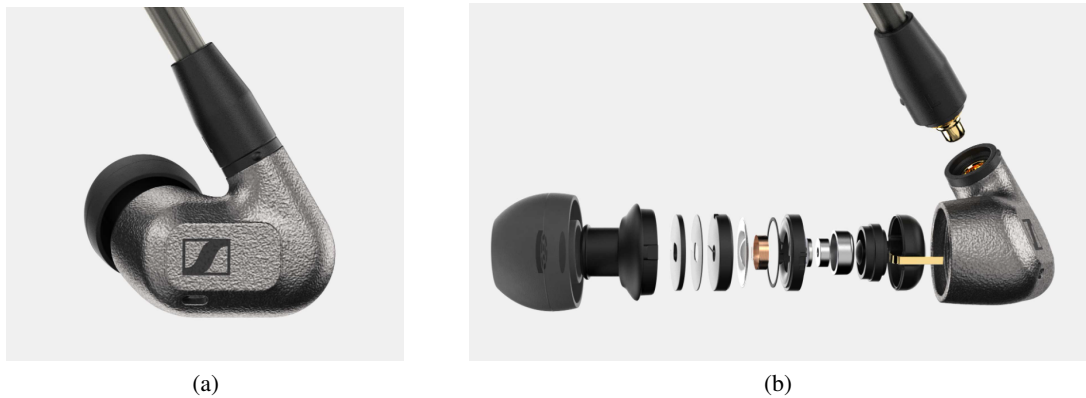


Figure 2.18: 3d printing headphones [27].

2.5 Finite Element Method - FEM

2.5.1 Introduction

The finite element method (FEM), or finite element analysis (FEA), is based on the idea of building a complicated object with simple blocks, or, dividing a complicated object into smaller and manageable pieces [28].

FEM is a reliable and efficient way to solve heat transfer problems. Over the past decades, FEM based techniques have been developed by many authors to simulate the metal additive manufacturing processes, however, the thermal process is quite complex and involves several physical phenomena such as moving heat source, material state change, and material deposition.

For example, in Abaqus, DFLUX user subroutine is developed to model a moving heat source by defining the heat flux distribution as a function of position and time, and UMATHT user subroutine is used to model the material state change and variation of thermal properties as a function of temperature and material state, and a built-in keyword *Model Change can be utilized to simulate the layer-by-layer building up process. Traditionally, these phenomena have been implemented using internal code or embedding. Some user subroutines in common commercial software packages such as Abaqus require considerable expertise. Fortunately, newer versions of Abaqus include AM Modeler, with a graphical user interface (GUI). This new plug-in tool provides a new and simple way to simulate additive manufacturing processes [29].

Thermal strains caused by the manufacturing process can result in residual stresses significant enough to cause failure during printing or throughout a part's service life. One of the primary goals of an additive manufacturing simulation is to:

1. Predict the residual stresses in a part.
2. Reduce the gap between the intended and manufactured parts by optimizing the manufacturing process.

3. Study how a manufactured item performs in an assembly with other components under realistic loading circumstances.

For the simulation of an additive manufacturing process, Abaqus offers two methods: a thermomechanical simulation and an eigenstrain-based simulation.

2.5.2 Eigenstrain-Based Simulation

'Eigenstrain' is a generic name given by the author to such nonelastic strains as thermal expansion, phase transformation, initial strains, plastic strains, and misfit strains [30].

Eigenstrain (also known as intrinsic strain, inherent strain, assumed strain, or "stress-free" strain) is a term in engineering that accounts for all types of inelastic deformation that result in residual stresses and distortions in produced components. Thermal strains are an eigenstrain subset.

An additive manufacturing process eigenstrain analysis consists of a single static stress analysis of a printed part with a specified field of eigenstrains applied to each element upon activation to represent the inelastic deformation generated by the process. Because inelastic deformations are the primary source of residual stresses and overall part distortion, the goal of an eigenstrain analysis is to forecast distortions and residual stresses in the part. Eigenstrains applied to a newly formed layer can cause residual stresses and distortion in the layers beneath it, Figure 2.19 [31].

1. The first layer has been added.
2. When negative eigenstrains are applied to the first layer, it contracts.
3. The second layer is placed on top of the first layer and bonded to it.
4. The bonding of the first layer constrains the contraction of the second layer, causing the part to deform and induce residual stresses.

This method eliminates the requirement for precise machine information; however, calibrating eigenstrain values from tests or thorough process-level thermomechanical models needs additional effort. An eigenstrain-based simulation produces more approximate findings than a thermomechanical simulation. In general, eigenstrain analysis is adequate for capturing distortion and residual stresses, but it may not capture higher-order deformation modes, such as buckling that might occur in thin-walled components during printing.

2.5.3 Thermo-mechanical simulation

Finite element modeling (FEM) can be used to predict distortion and residual stresses levels, allowing for optimization of the build plan prior to part manufacture and thus avoiding costly trial and error iterations. Residual stresses are caused by either plasticity due to contraction of the weld region or by solid-state phase transformations present in the material [32].

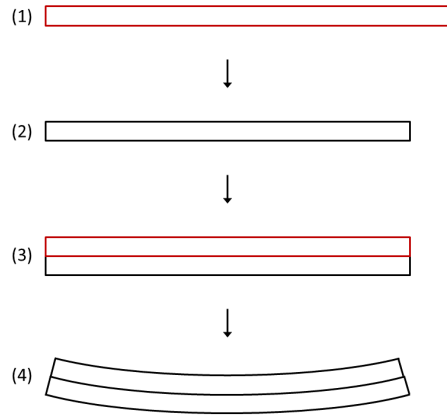


Figure 2.19: Distortion due to eigenstrains in a two-layer additive manufacturing process.

An additive manufacturing technique's sequential thermal-stress analysis comprises a transient heat transfer analysis of thermal loads introduced by the process on a printed part, followed by a static structural analysis driven by the temperature field from the thermal analysis [33].

The simulation provides detailed specifications of processing circumstances in time and space, as well as fine control over the quality of the solution. The simulation is accurate and thorough, but it becomes computationally expensive as time and spatial (mesh) resolution increase.

For the heat transfer analysis, the following aspects of the process must be included in the simulation.

2.5.3.1 Transient thermal analysis

Lagrangian reference frames are used in this work. Following a transient thermal analysis, an elastoplastic mechanical analysis is performed. Because the process is weakly coupled, the mechanical results will have a negligible effect on the thermal results.

The thermal analysis can be performed independently of the mechanical analysis because the plastic strain energy is small compared to the laser source energy, making the analyses weakly coupled [34].

The following is the governing equation for transient heat conduction:

$$\rho C_p \frac{dT}{dt} = -\nabla \cdot \mathbf{q}(\mathbf{r}, t) + Q(\mathbf{r}, t) \quad (2.1)$$

where ρ is the material density, C_p is the specific heat capacity, T is the temperature, t is the time, Q is the internal heat generation rate, \mathbf{r} is the relative reference coordinate, and \mathbf{q} is the heat flux.

The Fourier heat flux constitutive relation is given by:

$$\mathbf{q} = -k(T) \nabla T \quad (2.2)$$

where k is the temperature dependent thermal conductivity.

Thermal radiation q_{rad} is accounted for using the Stefan-Boltzmann law:

$$q_{rad} = \varepsilon \sigma_b (T_s^4 - T_\infty^4) \quad (2.3)$$

where ε is the surface emissivity, σ_b is the Stefan-Boltzmann constant, and T_s is the surface temperature of the workpiece, and T_∞ is the ambient temperature.

Newton's law of cooling accounts for the convective heat loss q_{conv} :

$$q_{conv} = h(T_s - T_\infty) \quad (2.4)$$

where h is the convective heat transfer coefficient.

2.5.3.2 Mechanical Analysis

Following the weakly coupled solution method described above, after the thermal simulation has been completed, which yields a temperature history for each node in the mesh, the quasi-static equilibrium of stress is determined for each time step. The governing stress equilibrium equation is:

$$\nabla \cdot \boldsymbol{\sigma} = 0 \quad (2.5)$$

where $\boldsymbol{\sigma}$ is the stress. A constitutive equation is required to relate stress, strain, and the material properties. The mechanical constitutive law is:

$$\boldsymbol{\sigma} = \mathbf{C} \boldsymbol{\varepsilon}_e \quad (2.6)$$

where \mathbf{C} is the fourth order material stiffness tensor and $\boldsymbol{\varepsilon}_e$ is elastic strain.

2.5.3.3 Small Deformation Theory

For small deformations, the total strain can be calculated as:

$$\boldsymbol{\varepsilon} = \boldsymbol{\varepsilon}_e + \boldsymbol{\varepsilon}_p + \boldsymbol{\varepsilon}_T \quad (2.7)$$

where, $\boldsymbol{\varepsilon}$, $\boldsymbol{\varepsilon}_e$, $\boldsymbol{\varepsilon}_p$ and $\boldsymbol{\varepsilon}_T$ are the total strain, elastic strain, plastic strain, and thermal strain, respectively [35].

2.5.3.4 Large Deformation Theory

The governing mechanical stress $\boldsymbol{\sigma}$ equilibrium equation when the current spacial location of the part \mathbf{x} in a deformed state may vary significantly from the undeformed reference configuration \mathbf{X} state is written as [36]:

$$\nabla_x \cdot \mathbf{P} = 0 \quad (2.8)$$

where the first Piola-Kirchoff stress tensor \mathbf{P} is defined as:

$$\mathbf{P} = J\boldsymbol{\sigma} \cdot \mathbf{F}^{-T} \quad (2.9)$$

where $\boldsymbol{\sigma}$ is the stress tensor and J is the determinant of the deformation gradient \mathbf{F} , which is defined as:

$$\mathbf{F} = \frac{d\mathbf{x}}{d\mathbf{X}} \quad (2.10)$$

The Green-Lagrange Strain \mathbf{E} is calculated as:

$$\mathbf{E} = \frac{1}{2}(\mathbf{D} + \mathbf{D}^T) + \frac{1}{2}(\mathbf{D} \cdot \mathbf{D}^T) \quad (2.11)$$

where the displacement gradient \mathbf{D} is defined as:

$$\mathbf{D} = \mathbf{F} - \mathbf{I} \quad (2.12)$$

where \mathbf{I} is the identity matrix. For small deformations the total Lagrangian formulation will simplify and equate to the small deformation formulation [35].

2.5.3.5 Inherent strain

Mura [37] developed a mathematical framework for determining the residual stresses corresponding to a given eigenstrain distribution in the case of an infinite three-dimensional body based on the concept of eigenstrain. However, it was Ueda who presented a series of papers between 1975 and 1994 in which he applied the inherent strain method to finite element models. The activation of experimentally measured or numerically computed eigenstrains within a simple finite element mechanical model to evaluate welding residual stresses and deformation is the basis for this method. Specifically, for a simple elastic FE model, the relation of the inherent strain $\boldsymbol{\varepsilon}_{inh}$ with elastic strains $\boldsymbol{\varepsilon}_e$ or stress $\boldsymbol{\sigma}$ produced by $\boldsymbol{\varepsilon}_e$ at an arbitrary point of a three-dimensional body can be expressed by the following elastic response equations [38]:

$$f = \int_V \mathbf{B}^T \mathbf{D} \boldsymbol{\varepsilon}_{inh} dV \quad (2.13)$$

$$u = \mathbf{K}^{-1} f \quad (2.14)$$

$$\boldsymbol{\varepsilon}_{tot} = \mathbf{B}u \quad (2.15)$$

$$\boldsymbol{\varepsilon}_e = \boldsymbol{\varepsilon}_{tot} - \boldsymbol{\varepsilon}_{inh} \quad (2.16)$$

$$\boldsymbol{\sigma} = \mathbf{D}\boldsymbol{\varepsilon}_e \quad (2.17)$$

where \mathbf{B} is strain-displacement matrix, \mathbf{D} stress-strain matrix \mathbf{K} stiffness matrix, u is the displacement vector and f is the nodal force vector.

2.5.3.6 Progressive Element Activation

During an analysis, the elements in each step increment can be activated. These elements must first be defined, and then they must be referred to in each analysis step where they can be activated.

Both full and partial element activation are supported. The material volume fraction added must be equal to 0 (inactive) or 1 (fully active) for full activation. For partial activation the material volume fraction added can be arbitrary; however, in practice the volume fraction in an element should not be too small to prevent numerical singularity problems.

In stress-displacement analyses it is assumed that the material added to an element is stress-free. Therefore, for full activation the configuration at which an element is activated is the stress-free configuration from which the strains used to compute the material response are measured. For partial activation the newly added material and the material already present are at different states. To obtain the material response, Abaqus/Standard uses the rule of mixtures to compute homogenized state variables [39].

Activation Methods

In additive manufacturing, material deposition is modeled using inactive or quiet elements that are activated as the added material (powder or wire) solidifies. For modeling material deposition, two metal deposition methods are reported:

- (1) Quiet Activation Strategy
- (2) Inactive Activation Strategy

In the quiet approach, the elements are present in the analysis but are assigned properties so they do not affect the analysis. In the inactive element approach, elements are not included in the analysis until the corresponding material has been added [40].

1. Quiet Activation Strategy

The elements representing metal deposition regions are present from the start of the analysis in the quiet element method. Their properties, however, are assigned so that they have no effect on the analysis. Thermal conductivity k is set to a lower value for heat transfer analyses to minimize conduction into the quiet elements, and specific heat C_p is set to a lower value to adjust energy transfer to the quiet elements [35]:

$$k_{quiet} = s_k k \quad (2.18)$$

$$C_{p_{quiet}} = C_p C_p \quad (2.19)$$

where, k_{quiet} and $C_{p_{quiet}}$ are the thermal conductivity and specific heat used for quiet elements, and s_k and S_{C_p} are the scaling factors used for the thermal conductivity and specific

heat, respectively. The quiet element method has the following advantages:

- It is simple to implement and can be applied to general-purpose finite element codes through the use of user subroutines.
- Because the number of elements does not change, the number of equations remains constant throughout the analysis, and no additional equation renumbering or solver initialization is required.

The quiet element method has the following disadvantages:

- If the scaling factors s_k and s_{Cp} are too large, thermal energy conducts into inactive elements, resulting in errors.
- The Jacobian may be ill-conditioned if the scaling factors s_k and s_{Cp} are too small.
- Using the quiet element method to model additive manufacturing, where the majority of the analysis domain is made up of quiet elements, may result in lengthy computer runs.

2. Inactive Activation Strategy

In the inactive element method, the elements representing metal deposition regions are removed from the analysis and only nodal degrees of freedom corresponding to active elements are considered. Numerical implementation involves computing the element residual and Jacobian for the active elements only and solving for the active nodal degrees of freedom only.

The inactive element method has the following advantages:

- There are no errors or ill-conditioning introduced by the scaling factor as in the case of the quiet element method.
- Element residual and Jacobian calculations are performed for active elements only.
- Only the active nodal degrees of freedom are considered at a time resulting in smaller algebraic systems by the Newton–Raphson linearization.

The inactive element method has the following disadvantages:

- The method cannot be easily incorporated into general purpose commercial codes using user subroutines.
- The equation numbering and solver initialization have to be repeated every time elements are activated. This may negate the computational advantage of solving for a reduced active number of degrees of freedom.
- When elements are activated, nodes shared by active elements may not be at the initial temperature which may result in artificial energy being introduced into the model.

3. Hybrid Activation Strategy

The hybrid element activation strategy was originally proposed as an improvement over both the quiet and inactive activation strategies. Elements are initially set as inactive. Then, layer-by-layer elements are switched to quiet, and then switched individually to active, based on the heat input. In this approach, equation numbering and solver initialization is repeated only when each layer is activated resulting in faster computer run times and equivalent results.

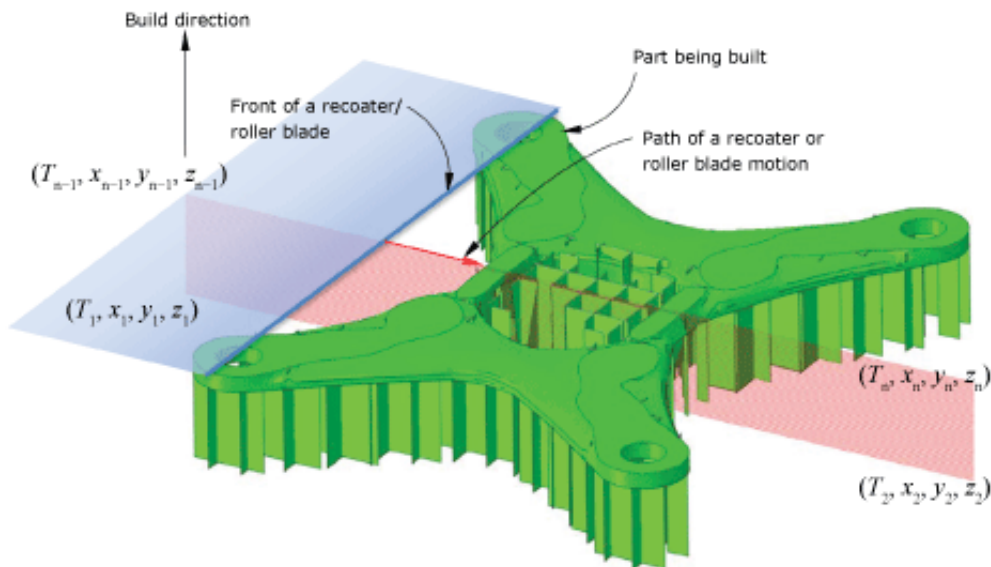


Figure 2.20: Recoater or roller blade motion in a powder bed-type AM process [33].

2.5.3.7 Event Series

An event series defines the collection of points. The first field defined in the event series describes a state of the tool, such as the laser power, the "on/off" state for a recoater roller, or a wire-feed nozzle. This field is assumed to be constant between two consecutive points. A zero-valued field indicates the "off" state of the tool [33].

Event series can be used to define fields that vary in both time and space. The field described with the event series is a piece wise-defined function. The events define the start and end points of path segments. Each segment of that path has a constant value of the field. Abaqus doesn't interpolate field values between events. In the INP file path, segments are defined using *EVENT SERIES keyword. Each data line of the keyword defines an event. The first data field defines time and the 2nd, 3rd and 4th data fields define the point in space of the event [41].

2.5.3.8 Toolpath-mesh

A toolpath represents the motion of a given component of a machine tool such as a laser source, a recoater roller, or a wire-feed nozzle. The toolpath-mesh intersection module is used to find

geometric intersections between various toolpaths used in additive manufacturing processes and a finite element mesh of the part to be manufactured.

A toolpath is defined by connecting a collection of points in space and time. For example, in a typical metal powder bed simulation, you can define the time-location history of both powdered metal deposition and a heating source (such as a laser) using an event series. The toolpath-mesh intersection module uses the event series data and automatically computes the relevant information required to activate elements and to apply the proper thermal energy to the model [42].

For toolpath-mesh intersection, three shapes are considered: a point, an infinite line, and a box Figure 2.21. Depending on the application, these shapes provide different levels of abstraction to characterize the shape of the tool.

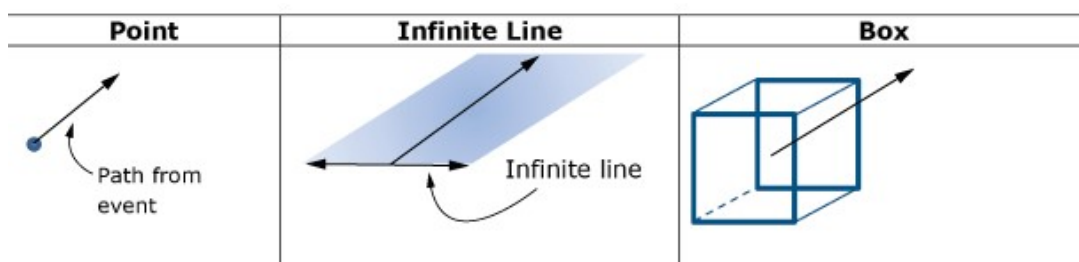


Figure 2.21: Point, infinite line, and box toolpaths

1. Point Toolpath-Mesh Intersection

When the action zone of the tool is very small compared to the mesh size and can be idealized as a point, Figure 2.22, such as when the laser beam radius is very small compared to the element size, the point representation of the tool shape is useful [43].

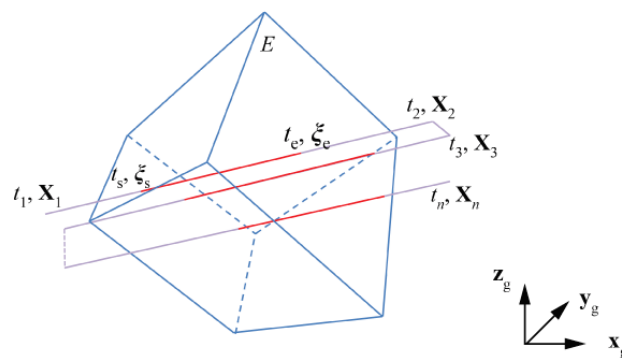


Figure 2.22: Point Toolpath-Mesh Intersection

2. Infinite Line Toolpath-Mesh Intersection

When describing the layer-by-layer material deposition process, such as the recoater roller's role in powder bed fabrication, the infinite line representation of the tool shape is helpful.

An infinite line toolpath and a finite element, E , are shown intersecting in Figure 2.23. An infinite line that is connected to a reference point and moves along the path connecting points defines the toolpath. It is assumed that the tool moves along a segment connecting two points in the path at a constant speed while the infinite line remains perpendicular to the segment [44].

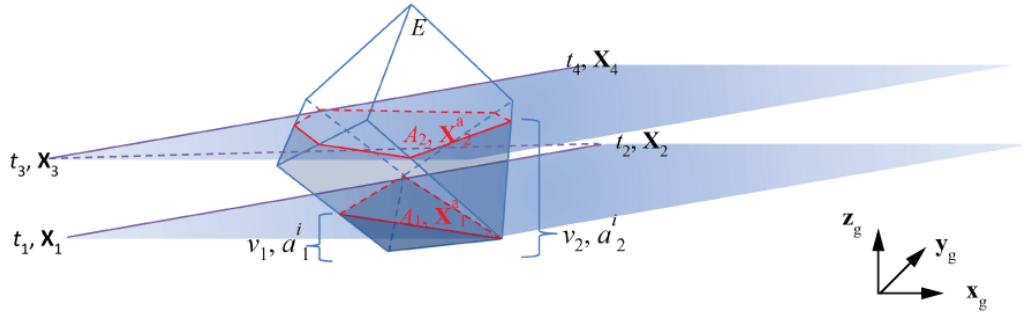


Figure 2.23: Infinite Line Toolpath-Mesh Intersection

3. Box Toolpath-Mesh Intersection

When the tool's action is best described as a spatially varying distribution, the box shape functionality is meant to be used. Intersections of a box toolpath and a mesh can be computed using two different algorithms or approaches; namely, the subsegment approach and the subelement approach.

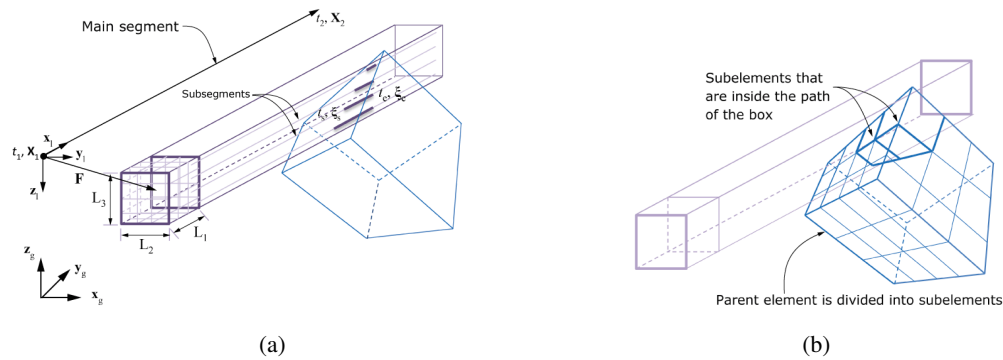


Figure 2.24: Box Toolpath-Mesh Intersection: (a) Subsegment approach and (b) Subelement approach

The toolpath is defined by a box attached to a reference point that is moving along the path connecting points. The box is divided into a user-defined number of smaller boxes, Figure 2.24 (a). For a given element, the toolpath-mesh intersection module computes the number of intersections of subsegments with the element, the coordinates of the start and end points.

In the subelement approach, the box is not divided into smaller boxes. Instead, the element is subdivided into subelements of the same topology, Figure 2.24 (b) [45].

2.5.4 Software

ANSYS - Analysis Systems

Analysis Systems - ANSYS offers general-purpose capabilities from both the computational fluid dynamics (CFD) and finite element analysis (FEA) disciplines.

The ANSYS multifield solver technologies for structural mechanics, fluid mechanics, electromagnetics, multiphysics, and system simulation as well as multiphysics heat transfer simulations and optics. Besides that, ANSYS solves a wide variety of coupled physics problems, that is, thermal–structural, thermal–electric-magnetic, electromagnetic–structural, and fluid-structure interactions. With sequential coupling, each physics discipline is solved sequentially, and results are passed from one physics discipline to another. The ANSYS workbench™ platform supports a collaborative environment for developing multiphysics solutions.

ANSYS is widely used in the aerospace industry for component design. The user needs to license various modules to fully model AM. ANSYS has been used to model certain features of some AM processes [13].

In ANSYS Additive Suite each finite element layer represents several real metal powder layers, assuming thermal continuity with the next layer. The program does not consider a moving heat source, such as when the thermal gradient in the build direction dominates over the thermal gradient in the plane direction due to its effect on residual deformations [46].

SIMULIA - ABAQUS

SIMULIA delivers a scalable suite of unified analysis products that allow all users, regardless of their simulation expertise or domain focus, to collaborate and seamlessly share simulation data and approved methods without loss of information fidelity.

The Abaqus Unified FEA product suite offers powerful and complete solutions for both routine and sophisticated engineering problems covering a vast spectrum of industrial applications. In the automotive industry engineering work groups are able to consider full vehicle loads, dynamic vibration, multibody systems, impact/crash, nonlinear static, thermal coupling, and acoustic-structural coupling using a common model data structure and integrated solver technology.

Best-in-class companies are taking advantage of Abaqus Unified FEA to consolidate their processes and tools, reduce costs and inefficiencies, and gain a competitive advantage [33].

COMSOL

The COMSOL Group provides software solutions for multiphysics modeling. The product line includes a suite of discipline-specific modules for structural mechanics, high and low-frequency electromagnetics, fluid flow, heat transfer, chemical reactions, microelectromechanical systems, acoustics, and more. COMSOL multiphysics simulations can be integrated with CAD models. Multipurpose tools are available to boost the functionality of the software and to verify and optimize the solutions.

Since COMSOL is basically a partial differential equation solver, the user has the freedom to add extra equations and boundary conditions for any new application. COMSOL is used widely around the world by researchers and engineers working for technical enterprises, research labs, and universities. COMSOL has been used to model certain features of some AM processes [47].

2.6 Residual Stresses

2.6.1 Definition

Residual stresses can be defined as stresses that remain in a material after manufacturing, heating, or other alterations and occur when a material undergoes non-uniform plastic deformation. The nonconformity that causes residual stresses can be introduced in many ways [48].

From a measurement perspective, the residual stress component is classified according to three characteristic length scales with which they operate [49]–[51].

1. *Type I*

Type I residual stresses are macroscopic stresses that act on the component geometry at the scale of the component and can cause global distortion. These might arise from plastic bending of a bar for example.

2. *Type II*

Type II micro stresses are microstructurally related stresses acting on a scale of a few grain diameters and are generally termed intergranular. These stress types tend to arise from inhomogeneity at the grain scale.

3. *Type III*

At a finer scale still are type III microstresses arising from heterogeneous behavior at the atomic scale.

Type I residual stresses are frequently mentioned in the literature concerning AM components. Large and anisotropic Type I stresses have a direct impact on fatigue properties in manufactured materials, resulting in distortion during or after production, and so dominate the literature discussion.

It has also been stated that type I stresses are more important in terms of mechanical properties, and that type II and III stresses are more difficult to measure [51].

2.6.2 Origin

Most manufacturing processes that involve material deformation, heat treatment, machining, or processing operations that change the shape or properties of a material generate residual stresses. Residual stresses can be large enough to cause local yielding and plastic deformation on both a microscopic and macroscopic level, affecting component performance significantly.

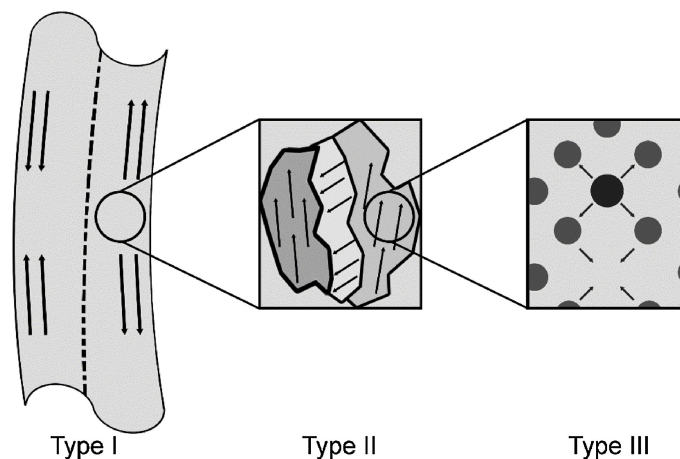


Figure 2.25: Residual stresses classification: Type I macro-stresses, Type II intergranular stresses and Type III lattice stresses [51].

Stress equilibrium must be maintained in any free-standing body, which means that the presence of tensile residual stresses in the component must be balanced by compressive stress.

Tensile Residual Stresses

Tensile residual stresses in the surface of a component are generally undesirable since they can contribute to fatigue failure, quench cracking and stress corrosion cracking.

Compressive residual stresses

Compressive residual stresses in the surface layers are usually beneficial since they increase both fatigue strength and resistance to stress-corrosion cracking, and increase the bending strength of brittle ceramics and glass.

In general, residual stresses are beneficial when they operate in the plane of the applied load and are opposite in sense (for example, a compressive residual stresses in a component subjected to an applied tensile load). The origins of residual stresses in a component may be classified as:

1. Mechanical

Mechanically generated residual stresses are frequently the result of non-uniform plastic deformation during manufacturing processes. Wire drawing, welding, machining, and grinding are examples of operations that produce undesirable surface tensile stresses or residual stresses gradients.

2. Thermal

Thermally generated residual stresses are frequently the result of non-uniform heating or cooling operations, such as quenching of steel or aluminum alloys. Microscopic thermally generated residual stresses can also form in a material during manufacturing and processing

as a result of a mismatch in the coefficient of thermal expansion between different phases or constituents.

3. Chemical

Chemically generated stresses can form as a result of volume changes caused by chemical reactions, precipitation, or phase transformation. Chemical surface treatments and coatings can cause significant residual stresses gradients in the component's surface layers.

2.6.3 Measuring Techniques

During the past years many different methods for measuring the residual stresses in different types of components have been developed. Residual stresses measurements can be divided into two categories depending on whether damage will be caused to the specimen or not: Mechanical release methods (destructive or semi destructive) and physical determination (non-destructive) as shown in Figure 2.26 [52].

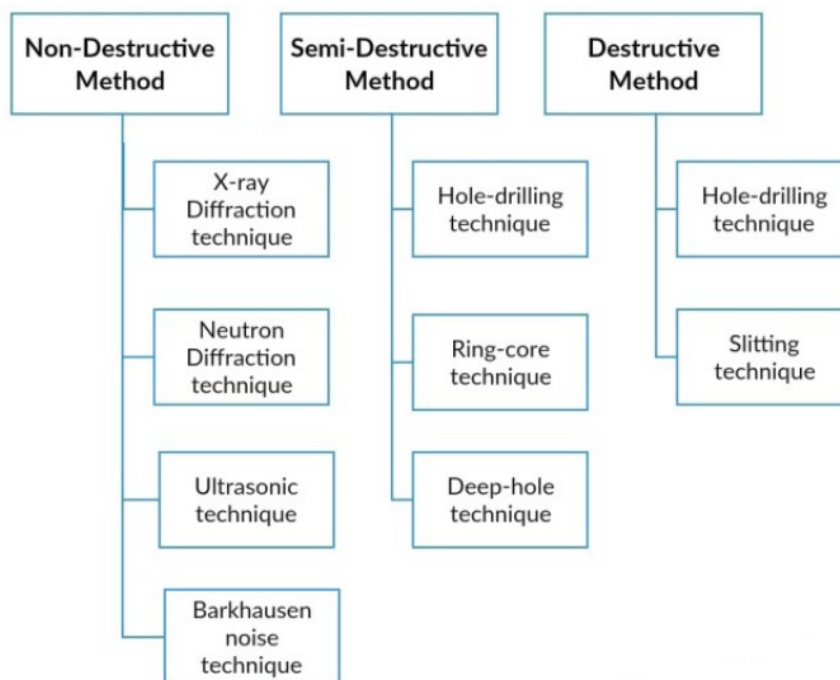


Figure 2.26: Residual stresses measuring techniques [53].

Mechanical methods

The destructive and semi destructive techniques, also called mechanical method, locally separate or split the component to release the residual stress, resulting in damage. Sectioning, contour, hole-drilling, ring-core and deep-hole are the principals destructive and semi destructive techniques used to measure residual stresses in structural members.

Physical determination

Non-destructive methods include X-ray or neutron diffraction, ultrasonic methods and magnetic methods which are all relatively expensive. X-ray diffraction can only be used to measure the surface of certain crystalline materials and is affected by surface preparation. Magnetic testing methods, which are based on the changing relationship between stress and the magnetization curve during the process of ferromagnetic saturation, can only be used on magnetic materials. And, in theory, ultrasonic testing is simple and suitable for depth varying residual stresses measurements, though there are some challenges to overcome, such as distinguishing sound velocity changes caused by material defects or stress [54].

2.6.4 Residual Stresses in AM

Laser based processes are known to introduce large amounts of residual stresses, due to the large thermal gradients which are inherently present in the processes. Figure 2.27 represents the temperature gradient mechanism - TGM [55].

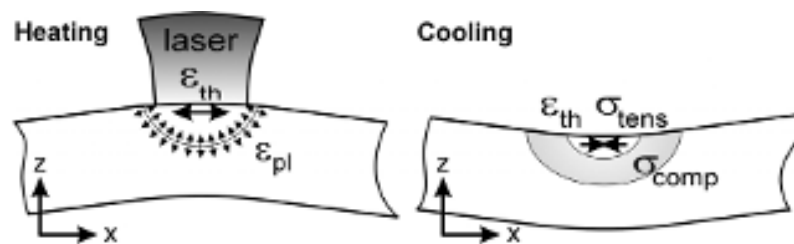


Figure 2.27: Thermal gradient mechanism inducing residual stresses [55].

When a new layer is added and heated much higher than the underlying part's temperature, the new layer of material will first expand uniformly. The much cooler underlying part will limit this expansion, resulting in the formation of compressive stresses in the new layer and tensile stresses in the underlying part [51].

This mechanism is also present in SLS and SLM, where the underlying layers prevent the heated top layers from expanding. It is important to note that this mechanism does not necessitate molten material [55].

Figure 2.28 shows the principal negative impacts of residual stresses in additive parts.

While the static mechanical properties of AM components, such as ultimate tensile strength or yield strength, have frequently been shown to match or exceed those of conventionally produced (due largely to the fine grain size produced during AM due to the fast cooling rates), fatigue properties can be dramatically lower Figure 2.28 (a).

During cyclic loading, significant tensile stresses act in addition to the applied load to accelerate crack propagation, increasing the crack growth rate ($\frac{da}{dN}$) and decreasing fatigue life.

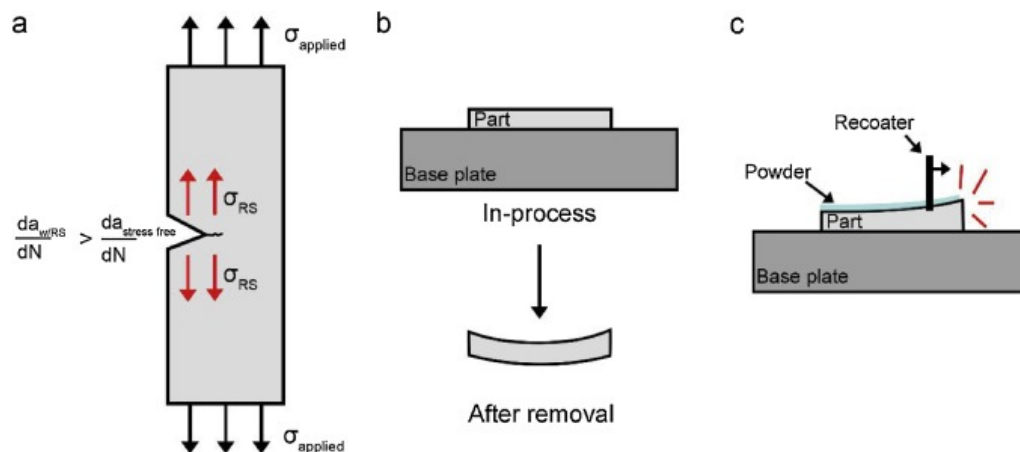


Figure 2.28: Effects of residual stress: a) reduced fatigue properties due to internal stress, b) distortion upon base plate removal and c) potential for process errors due to plastic deformation [51].

AM parts are manufactured on a large metal base plate, which limits part distortion during printing. When the part is removed from the plate, the residual stresses in the part causes permanent deformation to accommodate the redistribution of stresses to maintain equilibrium at the new free surface, affecting the geometric tolerances of the final part, Figure 2.28 (b).

Furthermore, large Residual Stresses values that exceed the yield strength during manufacturing can cause plastic deformation in-process, which may disrupt the process's continuation by interfering with powder spreading, Figure 2.28 (c) [51].

Chapter 3

Simulation Details and Methods

In this chapter, the simulations performed are described. The materials used, models and parameters are presented in this chapter. Subsequently, in the chapter 4, the results obtained will be presented and commented on.

3.1 Introduction

The purpose of this work is to develop and implement numerical modeling in Abaqus, of the PBF process and to compare the results obtained in the simulation with the experimental results provided. In the PBF process, the case study AMB2018-01 of NIST - National Institute of Standards and Technology was used [56]. This case study focuses on residual stress, distortion, and microstructure.

Regarding the DED process, the objective was to obtain a numerical model for the refurbishing of worn-out gears and pinions. In addition, a parametric study of this process was made, and the scanning strategy, the mesh, and the preheating temperature were some of the variables.

The purpose of this chapter is to make a framework for the problem and specify the parameters and materials used.

3.1.1 Physical specimens

Benchmark Bridge

The AMB2018-01 tests consist of laser powder bed fusion (LPBF) 3D metal alloy builds of a bridge structure geometry that has 12 legs of varying sizes. The 12 legs consist of 4 replications of a section described in the green box in Figure 3.1. The primary objectives of AMB2018-01 tests are to investigate residual stress within the structure, the part distortion which occurs after a section of the part is cut via wire electron discharge machining (EDM) [2].

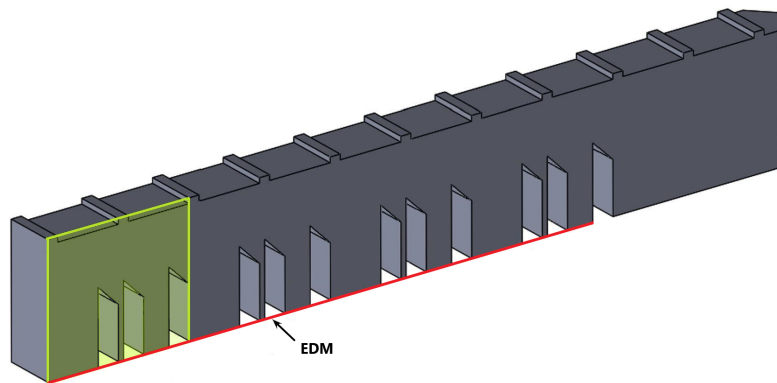


Figure 3.1: Benchmark Bridge structure and EDM cut location.

As shown in Figure 3.2, the bridge structure is 75 [mm] long, 5 [mm] wide, and 12 [mm] tall with with twelve legs that are of three different sizes - 5 [mm], 0.5 [mm], and 2.5 [mm], respectively. The thickness of 0.5 [mm] requires a refined mesh for reasonable results. Additionally, the bridge has eleven prominences at the top with 1x5x0.5 [mm] and with a spacing between them of 6 [mm].

The bridge is positioned on a build plate. The build plate structure is 90 [mm] long, 15 [mm] wide, and 12.7 [mm] tall.

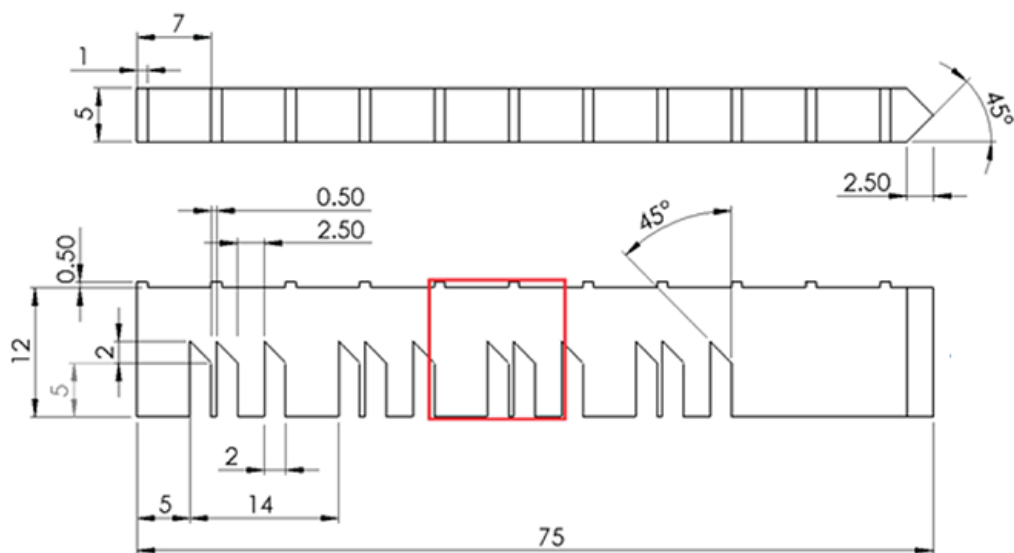


Figure 3.2: Bridge dimensions (in millimetres) [2].

Gear repair

As already mentioned in Chapter 2, the DED process can be used to repair various mechanical components, including gears.

Gears are a very useful transmission mechanism that is used to transmit rotation from one axis to another. The gear system can be used to decrease the speed (and also increase the torque). Gears are commonly used in high-load situations because the teeth of the gear allow finer, more discreet control of the movement of a shaft. Due to the high load situations to which gears are subjected, it is important to ensure that your repair is capable of withstanding these efforts.

To simulate the repair of the damaged gear, two main elements were considered, the tooth and the gear with a cut tooth, as shown in Figure 3.3, kindly provided by INEGI. In this figure, it is possible to observe the three stages of the gear rebuilding process. In this thesis, only the residual stresses caused by the DED process will be considered, the residual stresses resulting from the machining, Figure 3.3 (c), may be studied in future work.

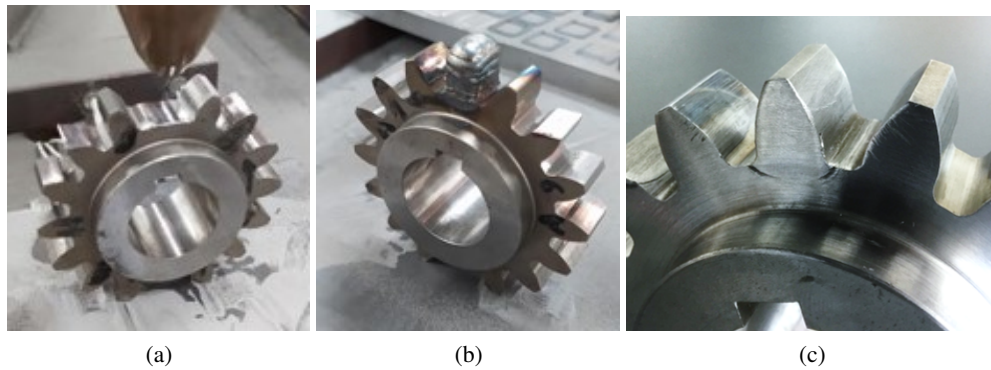


Figure 3.3: Gear to repair: (a) gear before repair; (b) gear after repair; (c) machined gear [4].

The parameters used in the DED process to repair the gear in Figure 3.3 are in Table 3.1. The repair of this gear was carried out at INEGI and served as a starting point for the parametric study carried out.

Table 3.1: Parameters used in the DED process of gear simulation.

Layer Height [mm]	Line With [mm]	Laser Power [w]	Scan Speed [mm/s]	Hatch Space [mm]
1.1	1.0	1800	111	1.0

The models for numerical simulation were created from the technical drawing of the pinion, Figure 3.4. This pinion is type C and has 14 teeth and an internal diameter of 30 [mm], the remaining dimensions are indicated in Figure 3.4.

from a lower (solidus) temperature to an upper (liquidus) temperature, Table 3.3. To model a pure material with a single phase change temperature, these limits can be made very close.

The latent heat is the extra energy required to make the phase change in the material in the form of thermal energy absorption (melting) or release (solidification). Latent heat can be combined with any other material behavior in Abaqus, but it should not be included in the material definition unless necessary; it adds an extreme non-linearity to the thermal solution which may inhibit convergence.

Table 3.3: Latent heat properties [57].

Latent heat of fusion [mJ/ton]	Solidus Temperature [°C]	Liquidus Temperature [°C]
272×10^9	1290	1350

The temperature dependence properties can be visualized in Table 3.4. In order to couple the thermal with the mechanical simulation the temperature field result is introduced as a time-dependent boundary condition for the static solution. A gradient of temperature causes a deformation in the solid which linearly depends on the expansion coefficient of the material.

Table 3.4: Thermo-physical properties of IN625 [57].

Temperature [°C]	Specific Heat [mJ/ton°C]	Conductivity [mW/mm°C]	Density [ton/mm ³]	Thermal expansion [1/°C]
21	4.10×10^8	9.8	8.44×10^{-9}	
93	4.27×10^8	10.8		1.28×10^{-5}
204	4.56×10^8	12.5		1.31×10^{-5}
316	4.81×10^8	14.1		1.33×10^{-5}
427	5.11×10^8	15.7		1.37×10^{-5}
538	5.36×10^8	17.5		1.40×10^{-5}
649	5.65×10^8	19.0		1.48×10^{-5}
760	5.90×10^8	20.8		1.53×10^{-5}
871	6.20×10^8	22.8		1.58×10^{-5}
982	6.45×10^8	25.2		
1093	6.70×10^8			

Young's modulus is a mechanical property of solids which gives the stiffness of the material. It can also be defined as the ability of the material to withstand changes in the shape of the material under expansion or compression. Young's modulus of a material is defined as the ratio of longitudinal stress to the linear strain, equation 3.1.

$$Young's\ modulus = \frac{stress}{strain} = \frac{F/A}{\Delta l/l} = \frac{\sigma}{\epsilon} \quad (3.1)$$

where σ is the uniaxial stress and ε is the strain, or proportional deformation. The length of the material increases as the temperature rises, reducing its stiffness. As a result, as the temperature rises, Young's modulus decreases, Table 3.5.

Table 3.5: Young's modulus of IN625 [57].

Temperature [°C]	Young's Modulus [MPa]
21	2.075×10^5
93	2.041×10^5
204	1.979×10^5
316	1.917×10^5
427	1.855×10^5
538	1.786×10^5
649	1.703×10^5
760	1.606×10^5
871	1.475×10^5

18Ni300 Maraging Steel

Maraging steels, first developed by the International Nickel Company in the 1960's, are a special class of high-strength steels that use nickel as the main alloying element. The term "maraging" is a portmanteau of martensite and aging and represents the age hardening of a low-carbon, iron-nickel martensitic matrix. Maraging steel is a class of high alloy, low carbon steel developed for structural applications requiring high strength. These steels are characterized by a large number of alloying elements and, consequently, they are expensive materials compared with many other engineering alloys. The excellent mechanical properties of maraging steel are attributed to the presence of Nickel and low Carbon content, with typically 0.04–1.7% C.

Unlike other tool steels, the martensitic microstructure is achieved by a relatively high concentration of nickel in the alloy composition rather than a relatively high percentage of carbon. This family of alloys has good weldability due to the practically complete absence of interstitial alloying components. As a result, they are susceptible to metal additive manufacturing procedures such as Laser Metal Deposition (LMD) and Selective Laser Melting (SLM) [59].

The qualities of this material are not as well established and documented as a result, the thermal property values were obtained experimentally and are shown in Table 3.6. The Poisson's ratio and Young's Modulus values were 0.3 and 190 [GPa], respectively. In terms of the material's plastic properties, a J-C model was used with values from the literature which are shown in Table 3.7.

Table 3.6: Thermo-physical properties of Maraging Steel [60].

Temperature [°C]	Specific Heat [mJ/ton·°C]	Conductivity [mW/mm·°C]	Density [ton/mm ³]	Thermal expansion [1/°C]
20	4.449x10 ⁸	15.81	8x10 ⁻⁹	1.8370x10 ⁻⁶
100	4.747x10 ⁸	17.46		1.0797x10 ⁻⁵
200	5.121x10 ⁸	19.52		2.1997x10 ⁻⁵
300	5.495x10 ⁸	21.58		3.3197x10 ⁻⁵
400	5.869x10 ⁸	23.64		4.4397x10 ⁻⁵
500	6.243x10 ⁸	25.70		5.5597x10 ⁻⁵
600	6.617x10 ⁸	27.76		6.6797x10 ⁻⁵
700	6.991x10 ⁸	29.82		7.7997x10 ⁻⁵
800	7.365x10 ⁸	31.88		8.9197x10 ⁻⁵
900	7.739x10 ⁸	33.94		1.00397x10 ⁻⁴
1000	8.113x10 ⁸	36.00		1.11597x10 ⁻⁴

The Johnson-Cook constitutive model is not based on traditional plasticity theory, which reproduces several important material responses observed in the impact and penetration of metals. Strain hardening, strain-rate effects, and thermal softening are the three main material responses. The Johnson-Cook constitutive model multiplicatively combines these three effects [61].

$$\sigma = (A + B\varepsilon^n)(1 + C \ln(\frac{\dot{\varepsilon}}{\dot{\varepsilon}_0}))(1 - (T_h)^m) \quad (3.2)$$

where ε is plastic strain, $\dot{\varepsilon}$ is the plastic strain rate, $\dot{\varepsilon}_0$ is the reference plastic strain rate, A is the static yield strength, B is the strain hardening coefficient, n is the strain hardening exponent, m is the thermal sensitivity parameter and T_h a non-dimensional homologous temperature defined as:

$$T_h = \left(\frac{T - T_{ref}}{T_m - T_{ref}}\right)^m \quad (3.3)$$

In Equation 3.2 the first bracketed term represents the strain hardening of the yield stress, the next term models the increase in the yield stress at elevated strain rates, and the final bracketed term is a softening of the yield stress due to local thermal effects.

Table 3.7 shows the values obtained in the literature [62] for a plastic property using the Johnson-Cook model.

Table 3.7: Johnson-Cook Plasticity coefficients for Maraging Steel 300 [62].

A [MPa]	B [MPa]	n	m	C	$\dot{\varepsilon}_0$
758.423	172.147	0.2258	0.7799	0.0522	70

42CrMo4 Steel

The 42CrMo4 (1.7225) steel is a low alloy steel that contains chromium, molybdenum, and manganese - Table 3.8. The presence of chromium and molybdenum increases corrosion resistance. Molybdenum is especially useful in resisting corrosion caused by chlorides. This steel has different grades, the European designation is 42CrMo4 (1.7225), and the USA grade is 4140.

Table 3.8: Chemical composition (wt%) of 42CrMo4 Steel [63].

C	Cr	Mn	Si	Mo	S	P	Fe
0.38 - 0.43%	0.80 - 1.10%	0.75 - 1.0%	0.15 - 0.30%	0.15 - 0.25%	0.040% max	0.035% max	Balance

This steel is widely used in a variety of industries like aerospace, oil and gas, and many other industries. It is often used for thin-walled pressure vessels, shafts, spindles, gears, collars, clamps, high-strength bolts, valve bonnet, screws, nuts, worms, collets, torsion bars, and various carburized parts because of its toughness, abrasion and impact resistance, and high fatigue strength. Material 42CrMo4 Thermo-physical properties are given in the Table 3.9.

Table 3.9: Thermo-physical properties of 42CrMo4 Steel [64].

Temperature [°C]	Specific Heat [mJ/ton·°C]	Conductivity [mW/mm·°C]	Density [ton/mm ³]	Thermal expansion [1/°C]
20	4.60x10 ⁸		7.8x10 ⁻⁹	
100	4.80x10 ⁸	42.7		1.22x10 ⁻⁵
200	4.73x10 ⁸	42.3		1.26x10 ⁻⁵
400	5.19x10 ⁸	37.7		1.36x10 ⁻⁵
600	5.61x10 ⁸	33.1		1.45x10 ⁻⁵

To characterize the plastic regime of this material, the Johnson-Cook constitutive model is used - Equations 3.2 and 3.3. In the table 3.10 are the values found in the literature [65] [66], respectively.

Table 3.10: Johnson-Cook Plasticity coefficients for 42CrMo4 Steel.

A [MPa]	B [MPa]	n	m	C	$\dot{\epsilon}_0$
595	580	0.133	1.03	0.023	70
852	1102	0.008	0.7	1	1000

The latent heat properties are showed in Table 3.11.

Table 3.11: 42 CrMo4 latent heat properties.

Latent heat of fusion [mJ/ton]	Solidus Temperature [°C]	Liquidus Temperature [°C]
250x10 ⁹	1399	1410

3.2 Simulations

The main objective of the simulations is to calculate the residual stresses and distortions resulting from the AM process. The prediction of these parameters, obtained through the simulations allows an optimization of the part design and its behavior when it is assembled with other components.

To perform the simulations of the AM process Abaqus has the toolpath-mesh intersection module. A toolpath represents the motion of a given component of a machine tool such as a laser source, a recoater roller, or a wire-feed nozzle.

For the simulation of AM process, Abaqus offers two options for additive process simulation that allows for the definition of appropriate boundary conditions, loads, interactions, constraints, and temperature-dependent material properties.

In the simulations performed, the thermo-mechanical simulation is used, which allows exact specification in time and space of processing conditions.

3.3 Benchmark Test AMB2018-01

3.3.1 Modeling

In the additive manufacturing benchmark test simulation, two parts are used - Figure 3.5. The bridge is positioned in the center of a build plate.

Several simulations were performed until the model was fine-tuned, to give consistent results. IN625 was used in both parts and the results obtained from this simulation will later be compared with the experimental results presented by NIST.

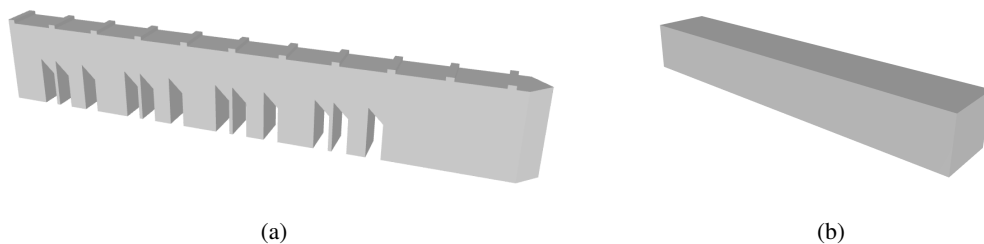


Figure 3.5: Benchmark Bridge (AMB2018-01): (a) Bridge (b) Build plate.

3.3.2 Initial Conditions

In the heat transfer analysis an initial temperature of 80°C is applied to the build plate. The initial temperature of the part is 40°C, which is the temperature at which the powder material is dispensed from the powder bed reservoir.

In structural analysis, the initial temperature of the assembly represents the relaxation temperature above which thermal strain results in negligible thermal stress. In material activation, it represents the temperature at which initial thermal shrinkage occurs [33].

In this analysis, the initial temperature of the bridge was set to 750°C. The initial temperature of the build plate is 80 °C.

3.3.3 Mesh - Bridge

A 3D 8-nodes linear brick element was employed in both the thermal and mechanical simulations, Figure 3.6. The structural element has the designation C3D8 and the heat transfer element is DC3D8. Along the printed area, the spatial distribution of the elements is uniform or "mapped." The printing simulation's results are influenced by the element sizes.

The first letter of the element's name indicates the family to whom the element belongs, in this case, the C in C3D8 indicates this is a continuum element. The number 3 represents the degrees of freedom.

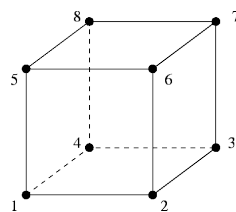


Figure 3.6: C3D8, Linear element 8-node brick.

The mesh of the bridge structure consists of 8-node linear diffusive heat transfer DC3D8 elements. The elements vary in size but have a common characteristic height of 0.2 [mm] so that there are approximately ten layers of material in each element. The build plate is more coarsely meshed with DC3D8 elements. In static analysis C3D8 solid elements are used for both the bridge and the build plate, maintaining the same mesh topology used in the heat transfer analysis, Figure 3.7.



Figure 3.7: Benchmark Bridge Mesh: (a) Bridge (b) Substrate.

3.3.4 Progressive Element Activation

A laser beam scans at a controlled speed the selected locations of the powder bed and fuses the powder, then the powder bed is lowered by the defined layer thickness and a new layer of powder is added. Progressive element activation can be used in Abaqus to represent layer-upon-layer raw material deposition in a thermal-stress analysis.

A sequential thermal-stress analysis of an additive manufacturing process consists of a transient heat transfer analysis of thermal loads introduced by the process followed by a static structural analysis that is driven by the temperature field from the thermal analysis [39].

During the analysis, it is possible to control the activation and the volume fraction of the material for each element in each increment. Any element that is defined as progressively activated is filled with material or remains empty (inactive). The figure 3.8 shows the progressive activation of the elements.

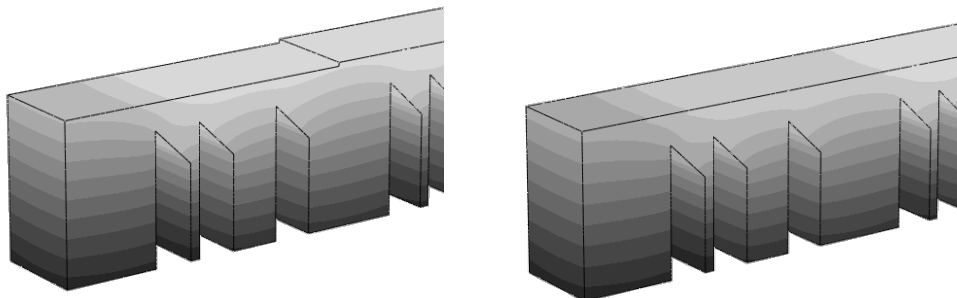


Figure 3.8: Benchmark Bridge progressive activation.

Material Deposition

To define the material deposition process, it is necessary to take care of the following steps [67]:

1. *Heating source*: The toolpath-mesh intersection module takes the time-location history and automatically computes all of the information required to activate elements and apply the proper thermal energy to the model. The time-location history of the heating source can be represented by an event series, in the form of a table of time, spatial coordinates, and process parameters.

2. *Recoater motion*: The infinite line representation is useful to describe this process of layer-by-layer material deposition. It is assumed that the tool travels at a constant velocity over a segment connecting two successive points in the path. All path segments when the tool is in the "on" state must be perpendicular to the global z-direction.
3. *Table collections*: Table collections that encapsulate parameter tables or property tables can be used to define additional process parameters needed for the simulation.

Thermal analysis

For the thermal analysis it is necessary to consider the following steps:

1. *Scanning trajectory*: every additive manufacturing process adds new material with time
2. *Heating*: Progressive heating of the deposited material - for some additive manufacturing processes, the newly deposited layer of material gets heated up to the melting point, causing the material to fuse to an underlying layer or a substrate.
3. *Cooling*: as the part is printed there is a progressive cooling, its cooling surface is continuously evolving with time.

Stress analysis

For the stress analysis,

1. Temperatures from the heat transfer analysis are used to drive the stress analysis.
2. Similar techniques of progressive material deposition as the heat transfer analysis can be used.
3. Temperature-dependent material properties can be used for accurate stress results.

3.3.5 Scanning Strategy

Scanning strategy is the spatial moving pattern of the energy beam (laser, electron beam, electrical arc, and so on). For a single-layer scan, the scanning strategy varies by different scanning directions, scanning sequence, scanning vector rotation angle, scanning vector length, scanning time, and hatch space [68].

The uni-directional, Figure 3.9 (a), and bi-directional or zigzag scanning strategy, Figure 3.9 (b), as the most common scanning strategies. These scanning strategies have a long vector, and the change in the scanning direction is where they diverge from one another. The chessboard, checkboard or island scanning strategy, Figure 3.9 (c), shortens the scan vector by segmenting the area into tiny square cells. Figure 3.10 shows the representation of the overlapping layers using different scanning strategies.

As a result, the scanning vectors' length, scanning direction, and rotation angle can be changed in accordance with the independent and distinct small units. The prolonged scanning line will result in excessive, accumulated stress, which compromises the component quality. The island

scanning technique can be used as an alternative to producing huge pieces with higher quality [68].

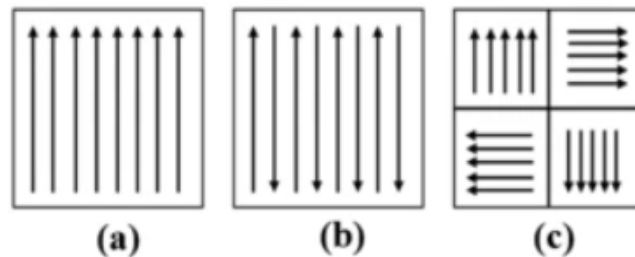


Figure 3.9: Scanning strategies (a) unidirectional scan; (b) bi-directional/zigzag scan; (c) island scan [68].

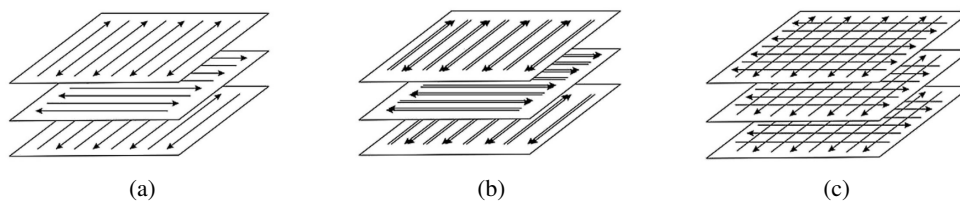


Figure 3.10: Scanning strategies: (a) alternate hatches - single pass, (b) alternate hatches - two passes and (c) cross hatches - single pass [69].

The impact of scanning strategies during the processing of different materials has been the subject of numerous research. The laser speed, the solidification direction imposed by the moving heat source, the hatch space and the cooling rate are some of the parameters that greatly influence the results obtained. These parameters influence the mechanical properties obtained, as well as residual stress, porosity levels and crystallographic texture of the material [70].

For this simulation, a Scan strategy was used in which for odd-numbered layers, the infill scans are horizontal lines (parallel to the X-axis) that are separated by 0.1 [mm] (hatch spacing), and for even-numbered layers, the infill scans are vertical lines (parallel to the Y-axis) that are also separated by 0.1 [mm]. Figure 3.11 show the scan pattern strategy description.

The process starts with the laser going through a full layer of the bridge, then the laser is disabled, and the roller is activated. The roller extends a thin layer of metallic powder and then the laser is activated again to go through another layer. This process is repeated until the final structure of the bridge is obtained. Each powder layer is 0.02 [mm] thick, and a total of 625 layers is needed to build the bridge structure. In the figure 3.12 can be seen the slicing done to obtain the necessary event series for the simulations.

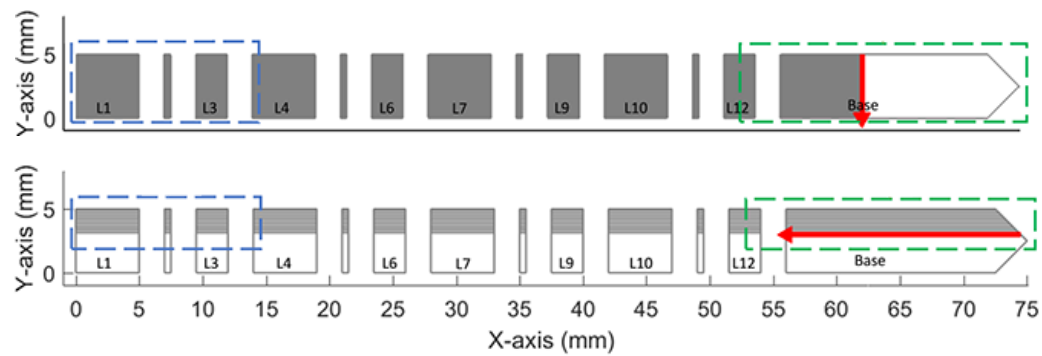


Figure 3.11: Description of scan pattern strategy [2].

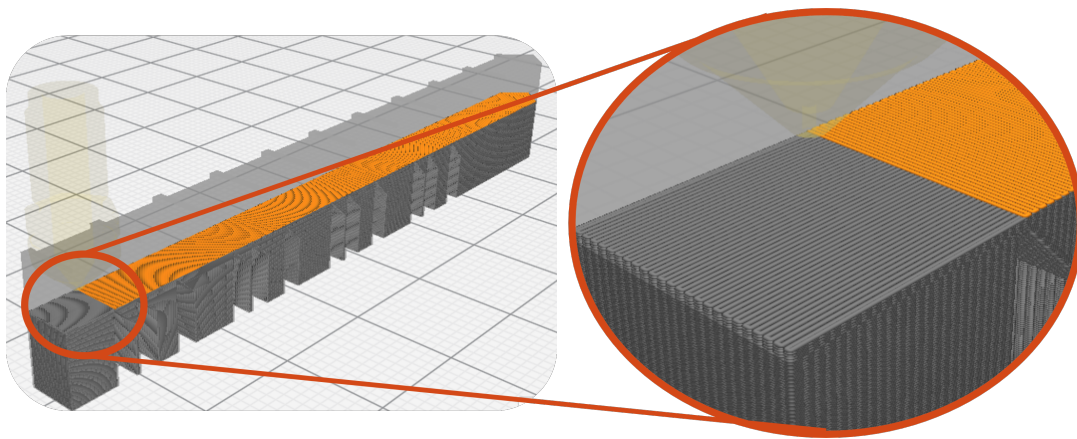


Figure 3.12: Scan Strategy - Bridge Benchmark.

The Table 3.12 shows the main parameters used to generate the path traveled by the laser.

Table 3.12: Parameters used in the AM process of the benchmark bridge.

Layer thickness	Laser Power	Scan Speed	Hatch Space
0.02 [mm]	195 [w]	900 [mm/s]	0.1 [mm]

3.3.5.1 Python Script

To obtain the Event Series required for simulations, a python script was developed. This script reads a ".gcode" file, obtained from the Ultimaker Cura software, and converts it into a series of events that describe the progressive activation of the elements. This software, similar to others, allows you to adjust various simulation parameters, from the height and thickness of the layer to the print speed and infill.

After the script was ready it was possible to export the files needed for the simulations. Both files obtained are in ".inp" format, one of which describes the movement of the heat source, simulating for example a laser and the other describes only a center line in which the z coordinate gradually increases, this intends to simulate the Roller which in the LPBF process is responsible for distributing a thin layer of powder. In the case of the LPBF process the script also allows you to set the laser power.

3.3.6 Cooling

The two heat-transfer mechanisms of cooling to the environment are convection and radiation. Both are subjected to a sink temperature of 25°C. Except for the bottom surface of the build plate, all of the model's free surfaces are set to a typical film coefficient for an inert gas atmosphere of 0.018 [mW/(mm²°C)]. The emissivity of the exposed surface to the atmosphere is a significant property of radiation, and the chosen value was 0.45.

3.3.7 Postprocessing Simulation

Additional postprocessing activities done on a printed item, such as wire electrical discharge machining (EDM) to remove a part from a build plate or to remove support structures, heat treatment, or other following machining processes, are frequently required to be simulated [67].

After the build was completed, the parts were cut by wire electrical discharge machining, so only the ends of the parts remained attached to the plate. In the simulation, the cutting process by wire EDM can be modeled using progressive removal of specified elements in the cutting region. This was modeled in a separate step using a model modification to remove a layer of elements near the bottom of the legs. One of the ends of the part is still attached to a portion of the build plate. The cut part of the bridge bends upward due to the relaxation of residual stress, Figure 3.13.

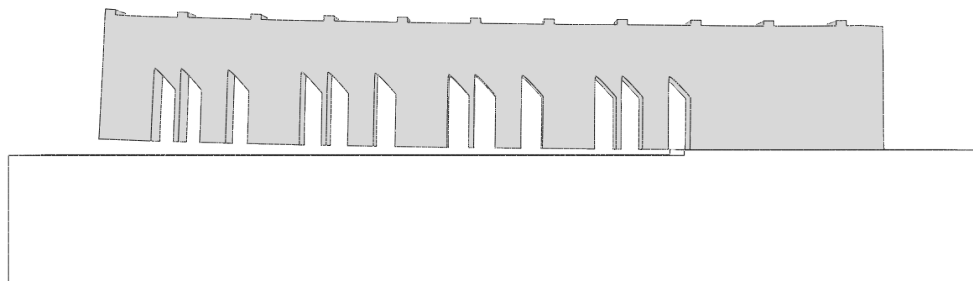


Figure 3.13: Nist benchmark bridge - Upward Deflection.

3.4 Gear Simulation

The GEAR3D project was the starting point for the simulations carried out in this chapter. This project aims to repair damaged mechanical components, namely wind turbine gears. Additive manufacturing is used to repair these gears, more specifically the DED process. The parameters used in the simulations were provided by INEGI - Instituto de Ciência e Inovação em Engenhariaia Mecânica e Engenharia Industrial.

The main objective was to make a parametric study that evaluated the influence of the various parameters of the simulation. Thus, the use of different materials, mesh size, scanning strategy, preheat temperature, and step time was the five parameters studied.

3.4.1 Modeling

During the process of modeling the gear, several attempts were made to obtain a reliable model. One of the first possibilities was to model two pieces separately. One of the pieces would be the substrate - the gear without the tooth that would be rebuilt, and the other piece would be the shape of the tooth to be rebuilt by DED. Both parts are represented in Figure 3.14 (a).

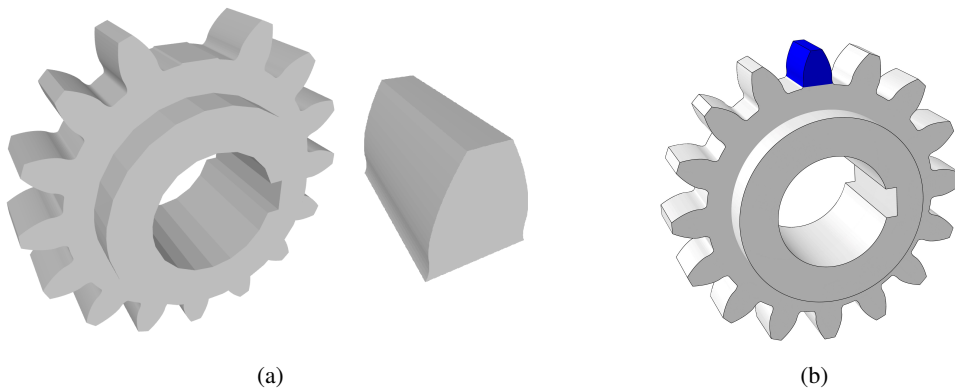


Figure 3.14: Gear Modeling - (a) gear and tooth belonging to the two-part model (b) one-part model.

Another possibility was the design of a single piece, Figure 3.14 (b). In order to simulate the tooth reconstruction, all elements are deactivated. The elements would later be activated as the part was DED printed.

Modeling two separate parts leads to different meshes on the parts. The simulation of two parts with different meshes can lead to the problem of discontinuity between meshes, Figure 3.15.

The mesh discontinuity problem becomes evident through the detachment of the two pieces when the obtained results are analyzed. Thus, only one of the mentioned possibilities can be considered for the simulations.

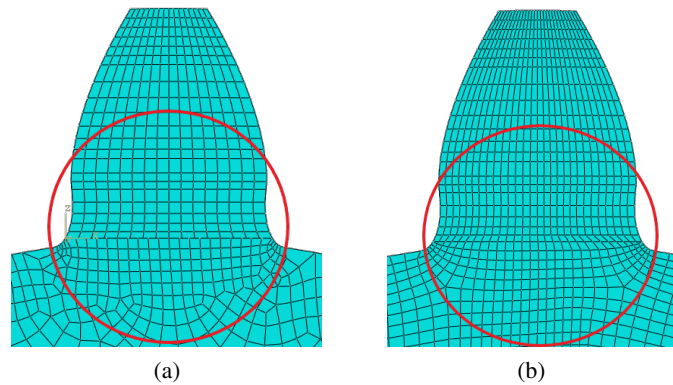


Figure 3.15: Gear Mesh: (a) Two parts model (discontinuous mesh); (b) One part model (continuous mesh).

3.4.2 Mesh

For the study of this parameter, three different meshes were used. The most discretized mesh has an approximate size of 0.25 [mm] and will be named Mesh-1, the second mesh has an approximate size of 0.5 [mm] and will be referred to as Mesh-2, finally, the coarser mesh has an approximate size of 1.5 [mm] and will be referred to as Mesh-3. In Figure 3.16 the three meshes used for these simulations can be observed.

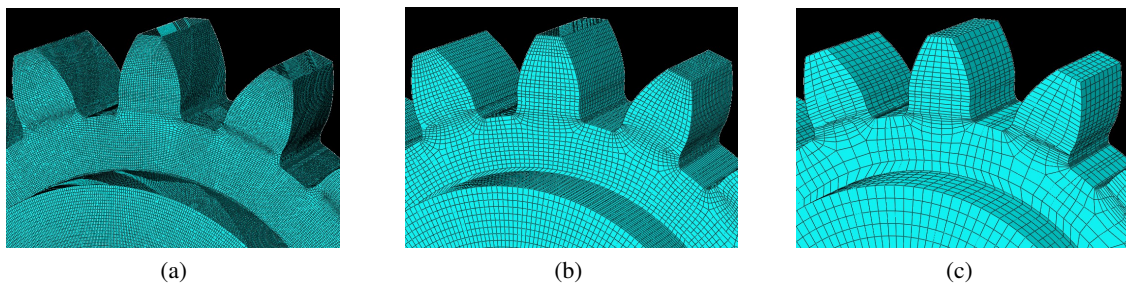
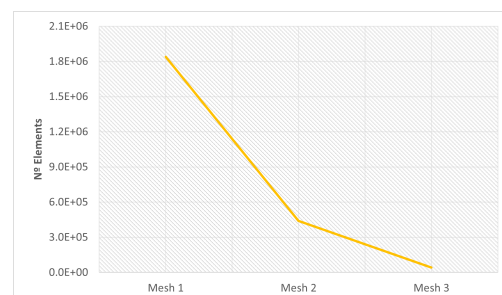


Figure 3.16: Mesh variation: (a) Mesh-1 (b) Mesh-2 (c) Mesh-3.

The material used in the mesh study was IN625, the same for the entire gear. The strategy chosen was the alternate hatches - single pass, Figure 3.10 (a).

Table 3.13: Mesh parameters - Elements number and mesh size.

	Number Elements	Mesh size [mm]
Mesh 1	1838455	0.25
Mesh 2	439768	0.50
Mesh 3	41832	1.50



The mesh size presented above, and the number of elements related to each mesh are organized in Table 3.13. The number of elements that each mesh has is represented in the graph on the right of the table. In this way, the difference between the number of elements of each mesh becomes more noticeable.

3.4.3 Scan Strategy

The literature describes various methods for mitigating residual stress effects of residual stress on the printed part. One of the most effective ways to reduce the impact of residual stress is to manipulate the scanning strategy. Scanning strategy refers to the manipulation of laser specifications such as laser power, scanning speed, and the laser scanning pattern.

For this parametric study, the strategies represented in Figures 3.17, 3.18, and 3.19 were used. These scanning strategies are zig-zag and angles of variation of 120° , 60° , and 0° are used.

The scanning strategies used are zig-zag, and the final piece is obtained by deposition of layers with different angles of deposition. In the first strategy, Figure 3.17 one of the layers is deposited with an angle of 90° and the next with an angle of 120° , this sequence repeats until the final piece is obtained. Before the filling material is deposited, a layer is deposited on the edge.

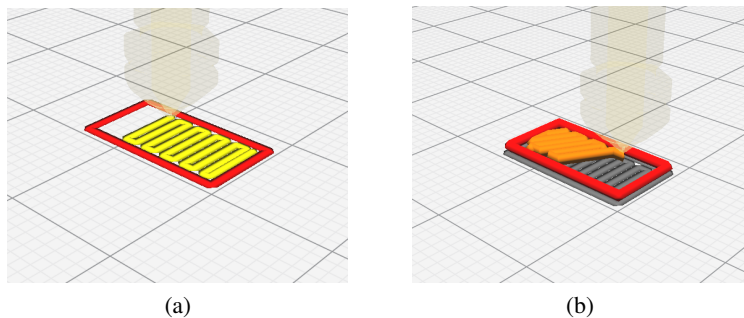


Figure 3.17: Scanning strategy I: (a) 90° (b) 120° .

In the second strategy the base layer is deposited with an angle of 90° , and the next with an angle of 60° , Figure 3.18. This sequence repeats until all piece is obtained.

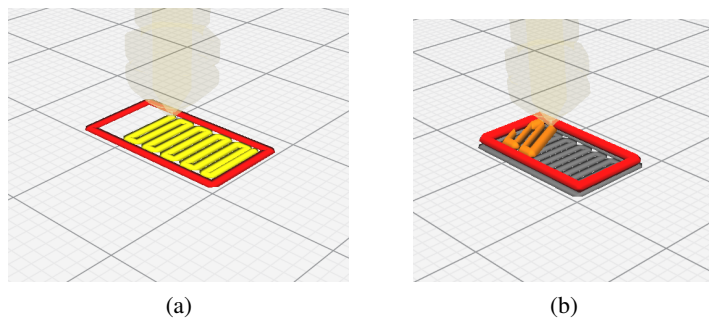


Figure 3.18: Scanning strategy II: (a) 90° (b) 60° .

In the third and last strategy, the layers are deposited perpendicularly, the base layer being deposited at 90° and the next at 0° , Figure 3.19.

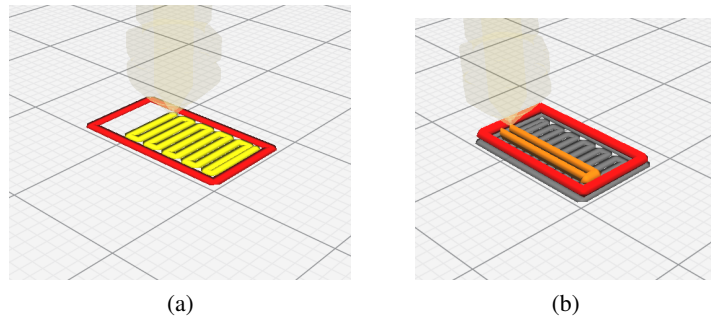


Figure 3.19: Scanning strategy III: (a) 90° (b) 0° .

3.4.4 Preheat Temperature

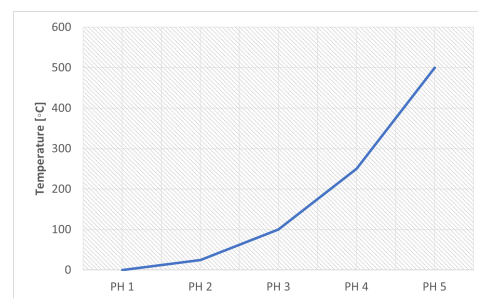
Preheating involves raising the temperature of the base metal above the ambient temperature before the DED process begins. By preheating the base plate, thermal gradients are lowered and stresses can be reduced avoiding cracks and delamination resulting from residual stresses [71].

During the initial depositions of the AM process, the reduction of thermal stresses is critical due to the presence of the substrate base, which acts as a heat sink and thus causes the formation of even higher thermal gradients and cooling rates [72].

Table 3.14 describes the preheating temperature values used in the study of this parameter. The figure on the right of the table graphically shows the preheat temperature variation.

Table 3.14: Preheat Temperature influence.

Name	Temperature [$^\circ\text{C}$]
Ph-1	0
Ph-2	25
Ph-3	100
Ph-4	250
Ph-5	500



3.4.5 Time step influence

The step time chosen influences the progressive activation of the material and can influence the final results.

Assume that two analyses are performed to simulate two different time increments: a small time increment activating one element per increment and a large time increment activating two elements per increment. In the two stress analyses, the initial configuration of every second element differs, resulting in different residual stresses and distortions [33].

Table 3.15 shows the variation of the step time parameters, the initial increment, and the maximum increment.

Table 3.15: Time Step Influence.

Name	Initial Increment	Max. increment
TS-1	5.0	15.0
TS-2	1.0	6.0
TS-3	0.5	3.0
TS-4	0.1	1.5
TS-5	0.05	0.3

3.4.6 Material

The objective of this work is to make a parametric study of some of the important variables in the repair of gears. Therefore, it is important to consider the use of different materials when repairing gears. So far in the simulations carried out, the same material (IN625) was considered in the substrate and part. However, this does not happen in the industry because IN625 is too expensive to be used in large gears. Normally, this type of gear is built with more economical materials such as 42CrMo4 steel and later receives a thermal treatment to acquire an adequate surface hardness.

Thus, to study the influence of the material, it was considered that the base plate (the gear) was built with 42CrMo4 steel and the tooth printed by DED was made of IN625.

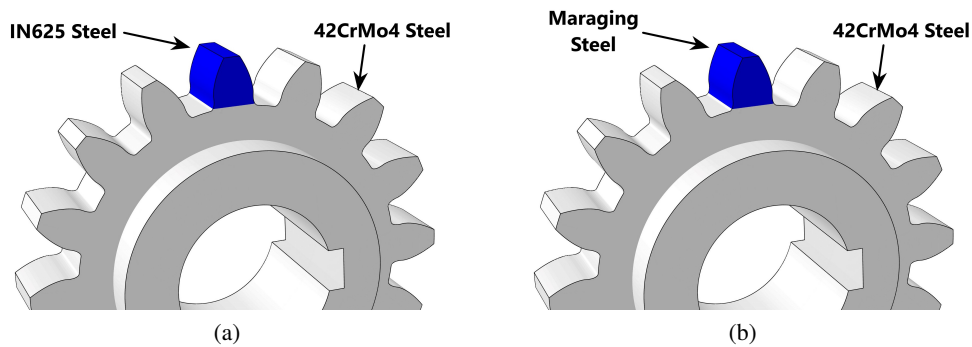


Figure 3.20: Gear repaired with different materials: (a) IN625 + 42CrMo4 steel (b) Maraging steel + 42CrMo4 steel.

Chapter 4

Results and Discussion

In this section, the results obtained for the parameters presented in Chapter 3 are presented. First, the results of the Benchmark Case are presented, and then the results of the gear's parametric study are presented.

4.1 NIST - Benchmark Bridge

4.1.1 Elastic strain

The results of the simulation are shown in Figure 4.1(a) and 4.2(a). Figure 4.1 shows a contour plot of the residual strain simulation results and experimental measure results in the x-direction. Similarly, Figure 4.2 shows the simulation and experimental results of the residual strain along the z-direction.

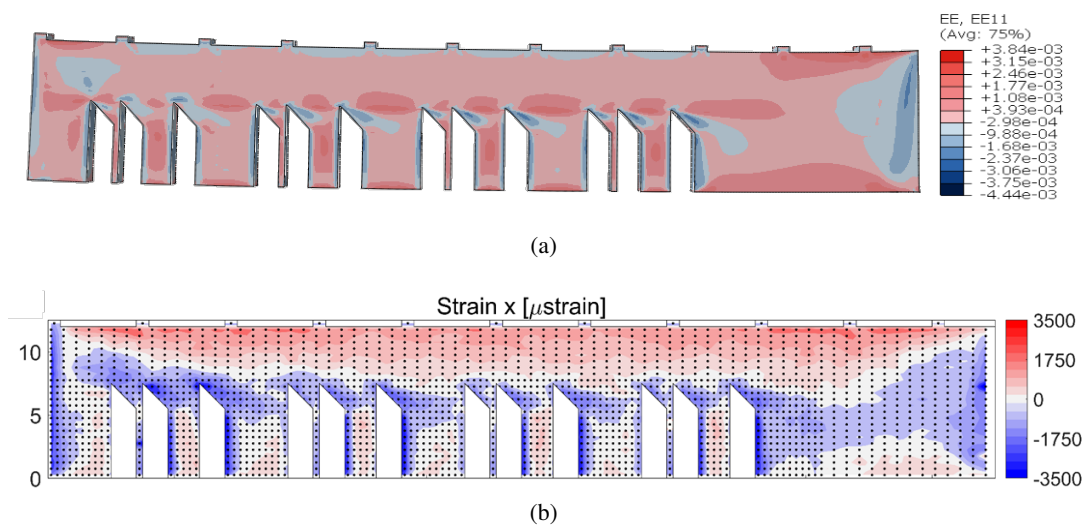


Figure 4.1: Comparison of elastic strain results in the x-direction.: (a) Simulation result EE11 (b) Strain measurements from NIST

The x strain components are mostly tensile, as shown in Figure 4.1. The highest tensile values are found near the top and bottom of the sample. When the sample is released from the substrate, the tensile region concentrated at the top of the sample causes a bending moment that drives the sample's distortion.

When the simulation results were compared to NIST results, a few key features show significant accord between simulation and experimental results. A comparison of the simulation and experimental contour plots, Figure 4.1, in the x direction shows that both results indicate tensile strains across the main body of the part, with compressive strains on the left side of each leg as well as at the ends. Besides that, the magnitude is on a very similar scale.

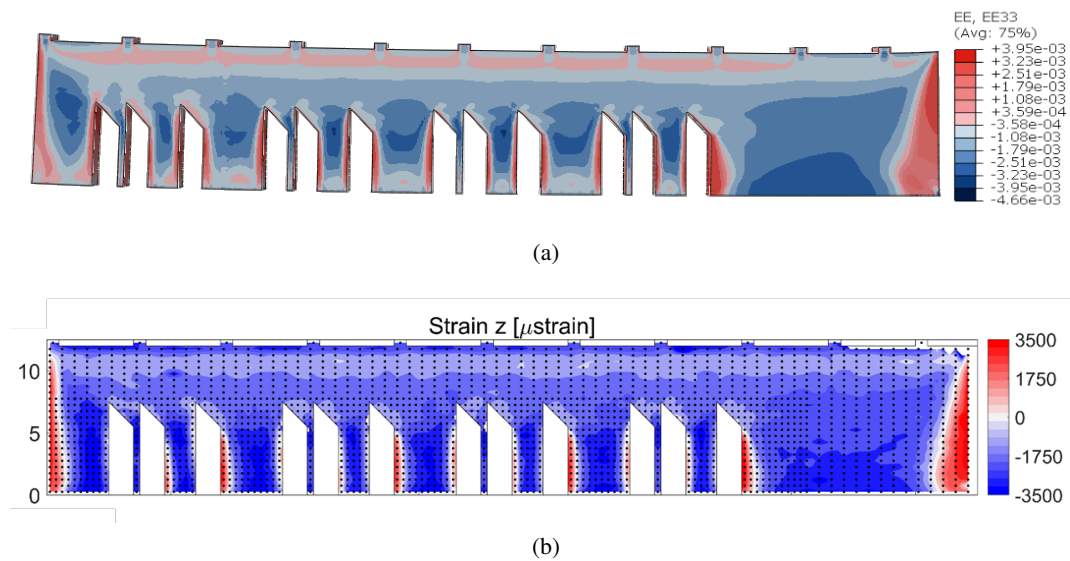


Figure 4.2: Comparison of elastic strain results in the x-direction.: (a) Simulation result EE33 (b) Strain measurements from NIST

In a similar manner, the comparison of contour plots in the z-direction reveals a very high level of convergence. Figure 4.2, shows that the Z strain component of the residual strain is compressive through the sample's interior while the sample's sides exhibit high-tensile regions. Again, the magnitudes are very close, with a peak value of $3.95e-3$ in simulations and $3.5e-3$ in experimental data.

4.1.2 Residual strain comparison between XRD, ND and simulation results

Because both neutron diffraction - ND and X-ray diffraction - XRD techniques measured lattice spacings, it is preferable to compare residual strains rather than calculated stresses. This is especially true because the synchrotron X-ray method could not measure all three orthogonal components required to calculate stresses reliably. Only strains in the X and Z directions can be directly compared using neutron and X-ray results [73].

Figure 4.3 shows the line profile for XRD measurement (yellow line), ND measurement (gray line), and simulation result (blue line) along the longitudinal (X direction) of the sample.

It should be noted that the XRD measurements and simulation results were taken from $X=0$ [mm] to $X=75$ [mm], and the ND measurements were taken from $X=0$ [mm] to $X=60$ [mm].

Figure 4.3 compares the strain results in the vertical (build) direction. Near the left edge of the sample ($X=0$ [mm]), ND shows near zero vertical strain, while XRD and simulation results consistently show a drastic change in strain from highly tensile (positive) to compressive (negative) from the left edge of the sample.

However, results near the edges of the sample once again reflect ND's inability to capture the large strain gradients.

On the other hand, the results obtained from the numerical simulation (blue line) are almost always slightly superior to those obtained from measurements.

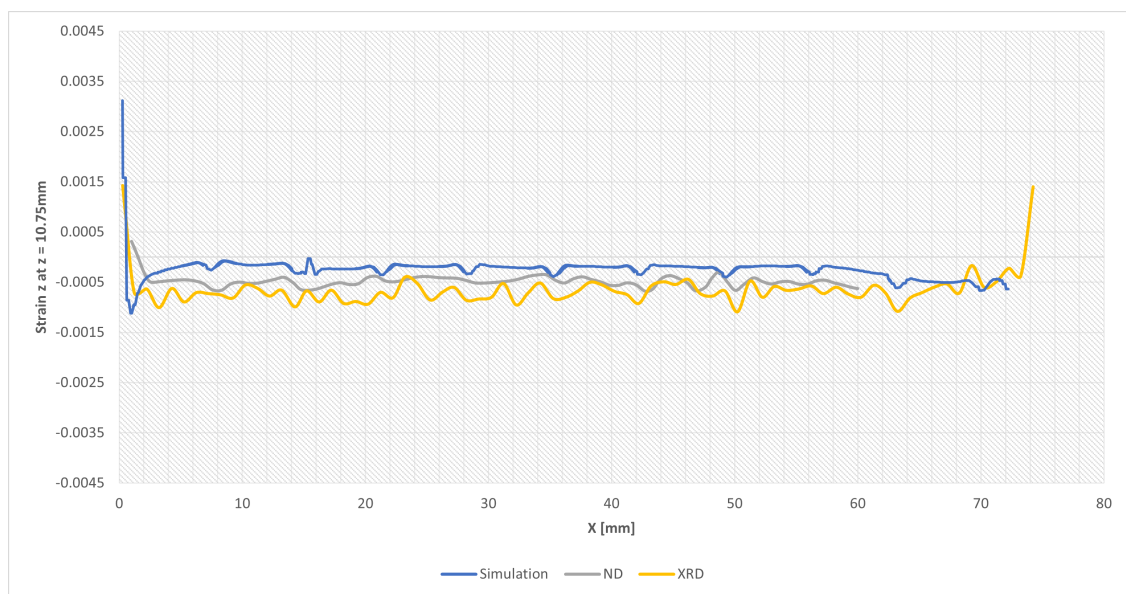


Figure 4.3: Benchmark bridge - Simulation result of elastic strain z at $z=10.75$ [mm]

4.1.3 Deflection analysis

After being built, the parts remain on the build plate. The tops of the 11 ridges are skim cut to remove the rough as-built surface. The vertical height, relative to the base plate, of the top of both side edges of each ridge is measured. The upward deflection results are presented in Figure 4.4, blue curve. Deflection measurements are all positive, indicating that the part was deformed upward after being separated from the build plate using EDM.

In Figure 4.5 it is possible to see the results obtained from the Abaqus simulation regarding the deflection of the bridge. As already shown in the graph – Figure 4.4, the deflection is maximum at the left end of the bridge and decreases until it is very close to zero at the opposite end.

The experimental values of deflection achieved by NIST are very similar to the numerical results, although at the right end of the bridge there is a small divergence.

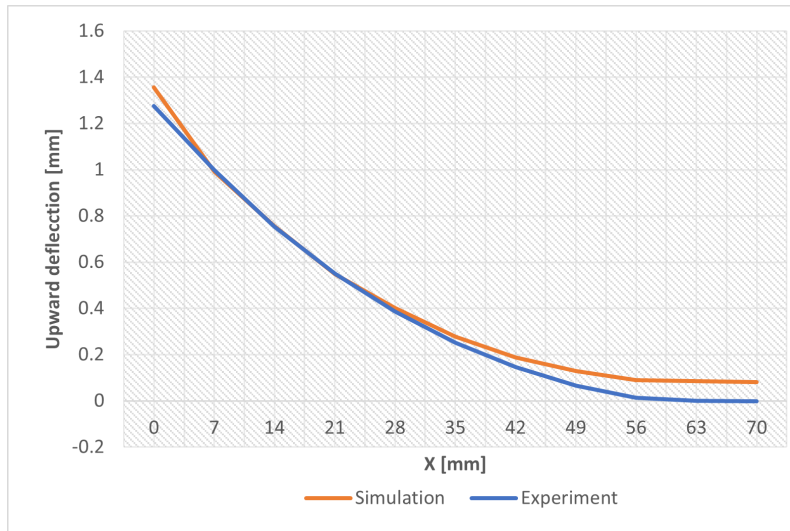


Figure 4.4: Benchmark bridge - Upward Deflection

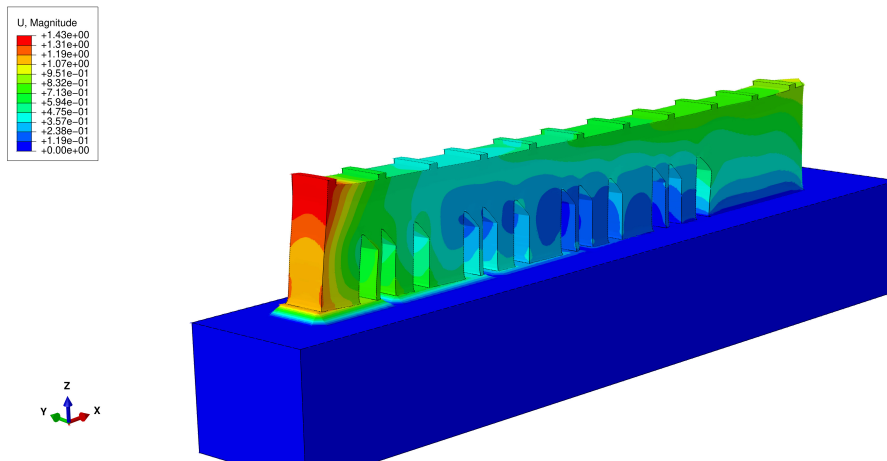


Figure 4.5: Nist benchmark bridge - Deflection

4.2 Gear - Parametric simulations

In this section, the results obtained from the parametric study performed will be shown. The residual stresses presented in this section correspond to the Von Mises stresses.

4.2.1 Mesh size

This section investigates the effects of mesh size on residual stress. For the three different sizes shown in Figure 3.16, three simulations were run using the same scanning strategy. The graphs that follow show the results of each variable's output.

The results obtained for the three meshes studied are grouped in Table 4.1. In the Figures 4.8 and 4.9 can be seen graphically see the results presented in the Table 4.1.

Analyzing the figure 4.7, it is noticeable that the results obtained for meshes 1 and 2 are very similar. On the other hand, the residual stress of mesh 3 is noticeably different, when compared to the other meshes. Given its mesh size of 1.5 [mm], mesh 3 may not promote an accurate description of the residual stresses developed in the gear during the AM process.

Table 4.1: Mesh Results

	Spatial Displacement [mm]	Residual Stress [MPa]	Number Elements	Mesh size [mm]	CPU Time [s]
Mesh 1	6.058E-02	804.4	1838455	0.25	420520.0
Mesh 2	6.072E-02	815.8	439768	0.50	25716.0
Mesh 3	3.182E-02	876.2	41832	1.50	1227.7

The computational cost is a parameter that must be taken into account because one of the objectives of this type of numerical simulation is to obtain results in the shortest possible time. This compromise between computational cost and accurate results must be balanced in order to be able to have credible results in an acceptable time frame.

In this way, the figure 4.6 makes the results related to computational time already presented in Table 4.1 more perceptible.

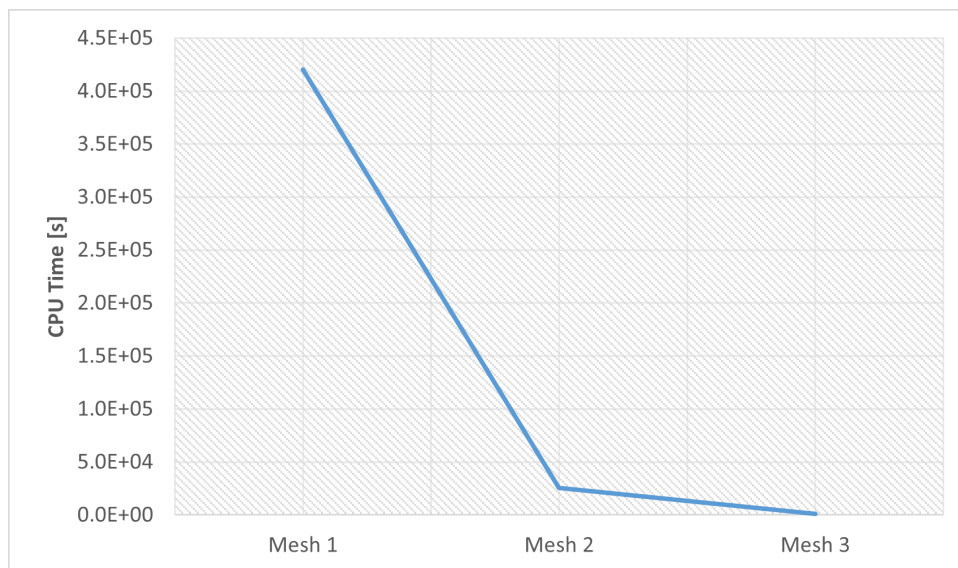
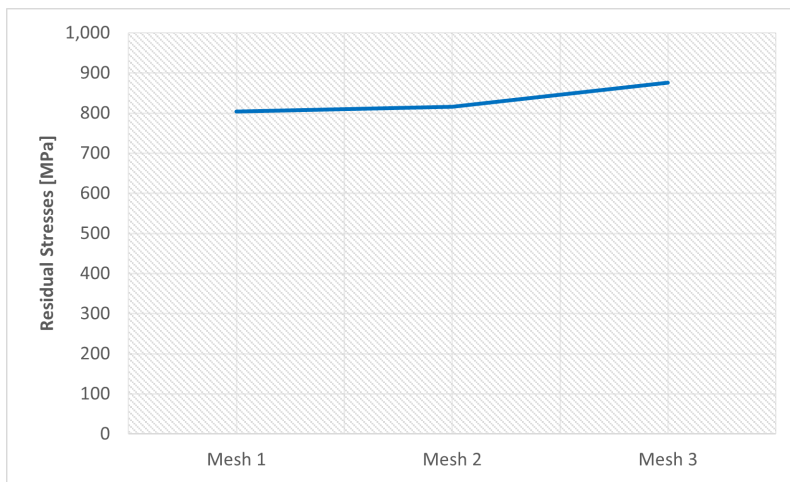


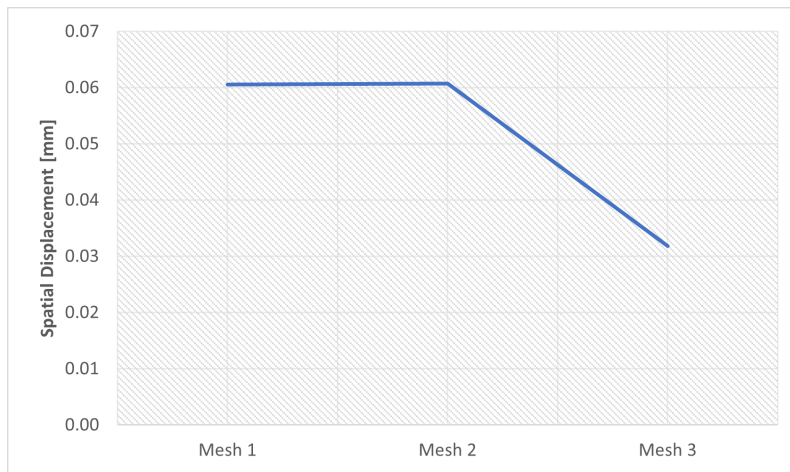
Figure 4.6: CPU time mesh simulations

After analyzing the results it becomes clear that Mesh 2 is the best option. This mesh presents results very similar to mesh 1 however the computational cost it's much lower due to the lower refinement of this mesh. Although mesh 3 has the lowest computational cost, the results obtained do not suggest that it presents an adequate description of the process.

Therefore, mesh 2 will be used in the remaining numerical simulations.



(a)



(b)

Figure 4.7: Results of the parametric study of the mesh size: (a) Residual Stresses (b) Spatial Displacement

Figures 4.8 and 4.9 show the results of the simulations of the mesh size influence for residual stresses and spatial displacement, respectively, for different mesh options. Concerning residual stresses, it is clear that Figure 4.8 (c) has the highest residual stress value and this is located at the root of the tooth.

Figure 4.9 show the results of the simulations of the mesh size influence for spatial displacement. As already shown in Figure 4.7 (b) meshes 1 and 2 have very similar values, on the other hand, the results of mesh 3 are much lower.

4.2.2 Scanning strategy

The scanning strategy is a key factor in determining the thermal history and melt channel combination within a part in a laser powder bed fusion (LPBF) process, which can significantly affect the microstructural evolution, defect formation, and mechanical properties of the part [74].

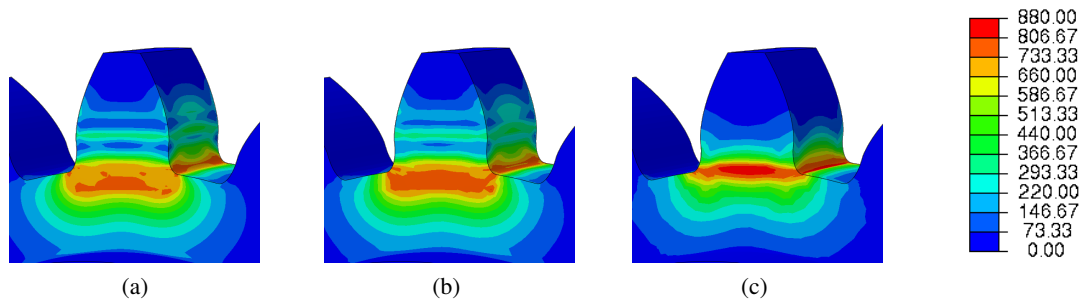


Figure 4.8: Results of mesh variation - Residual Stress: (a) Mesh 1; (b) Mesh 2 and (c) Mesh 3

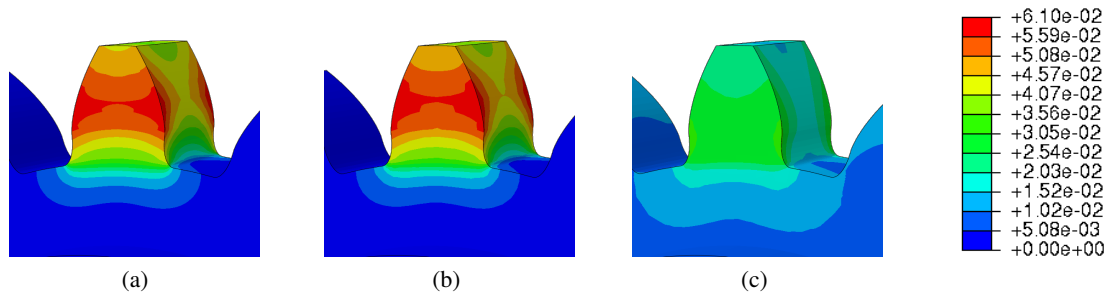


Figure 4.9: Results of mesh variation - Spatial displacement: (a) Mesh 1; (b) Mesh 2 and (c) Mesh 3

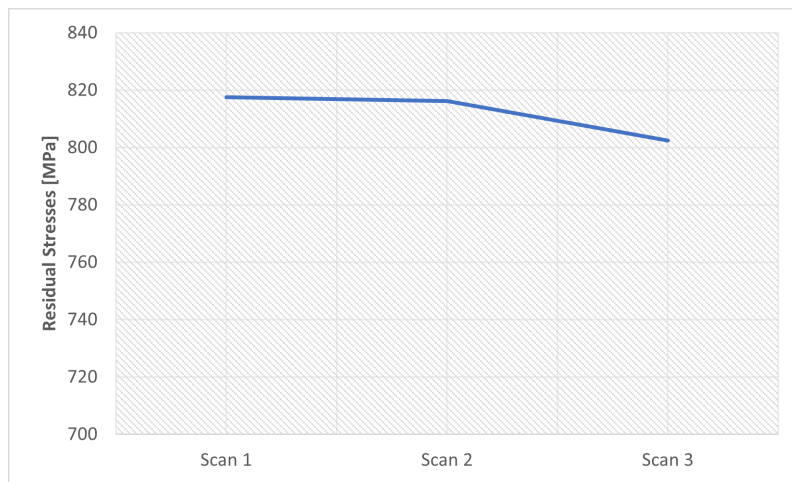
There are numerous ways to scan a single layer, and various scan strategies have been investigated in terms of residual stresses. In this section, the influence of three types of scanning [0° , 60° and 120°] already presented in the 3.4.3 section will be studied.

In Figure 4.10 the residual stress and spatial displacement results obtained for the three scanning strategies are graphically represented. Table 4.2 also shows the numerical results obtained for each of the scanning strategies.

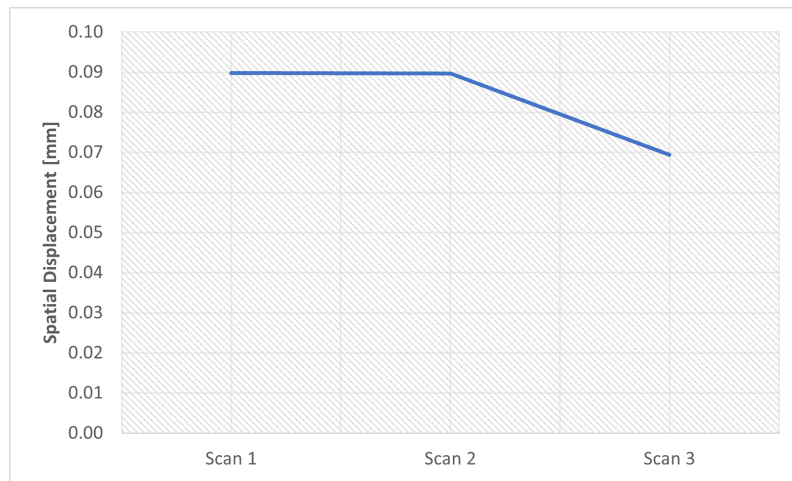
Analyzing the results, it is concluded that both strategies 1 and 2 present very similar results with a negligible variation. In turn, the third scanning strategy presents values lower than those obtained by the previous strategies.

Table 4.2: Scan Strategy Results

	Spatial Displacement [mm]	Residual Stress [MPa]	Angle [$^\circ$]
Scan 1	8.98E-02	817.5	[90,120]
Scan 2	8.97E-02	816.2	[90,60]
Scan 3	6.94E-02	802.5	[90,0]



(a)



(b)

Figure 4.10: Results of the parametric study of the scan variation: (a) Residual Stresses (b) Spatial Displacement

Figures 4.11 and 4.12 show the graphical results obtained from residual stress and spatial displacement, respectively.

Again, residual stresses are concentrated at the root of the tooth, however, in scanning strategies 1 and 2 they propagate along the tooth as shown in Figure 4.11 (a) and (b).

4.2.3 Preheat Temperature

The preheating temperature has a lot of influence on residual stresses and warpages. It is expected that by increasing the preheat temperature in the base plate (gear) the residual stresses and warping of the printed part (tooth) will decrease. Figure 4.13 represents the different preheating temperatures used in these simulations.

The numerical results obtained for the preheat temperature variation are summarized in Table 4.3.

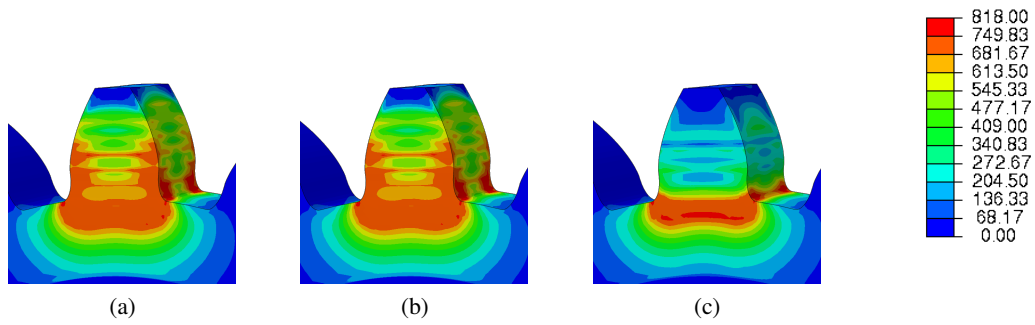


Figure 4.11: Scan strategy - Residual Stress: (a) Scan 1 (b) Scan 2 (c) Scan3

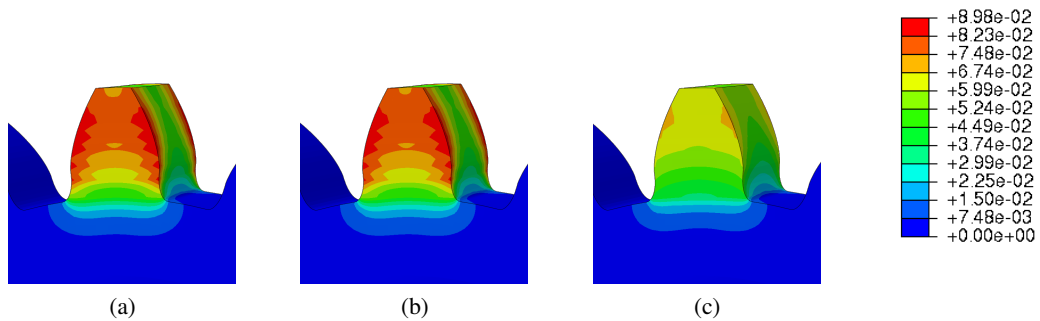


Figure 4.12: Scan strategy - Spatial Displacement: (a) Scan 1 (b) Scan 2 (c) Scan3

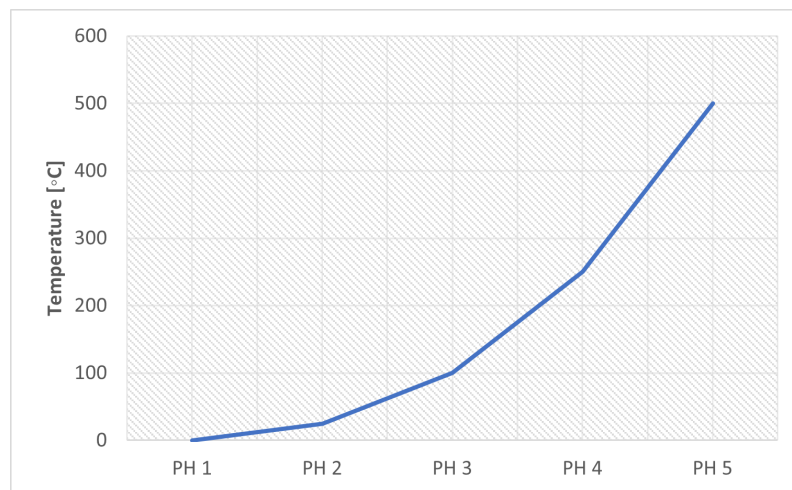


Figure 4.13: Preheat temperature variation

The results obtained are shown in Figures 4.14 4.15 and prove what was expected. With the increase in the preheating temperature, there was a decrease in the residual stresses of the gear. This reduction is significant since there is a reduction of 14% between the minimum preheat temperature of 0 degrees and the maximum preheat temperature analyzed.

Table 4.3: Preheat Results

	Spatial Displacement [mm]	Residual Stress [MPa]	Temperature [°C]
Ph-1	3.63E-02	893.2	0
Ph-2	3.15E-02	889.3	25
Ph-3	5.25E-02	875.0	100
Ph-4	1.14E-01	835.4	250
Ph-5	2.28E-01	767.8	500

Analyzing the obtained spatial displacement results, a high increase is visible as the preheat temperature also increases. Comparing the results obtained, an increase of 527% from the minimum preheating temperature to the maximum temperature is verified.

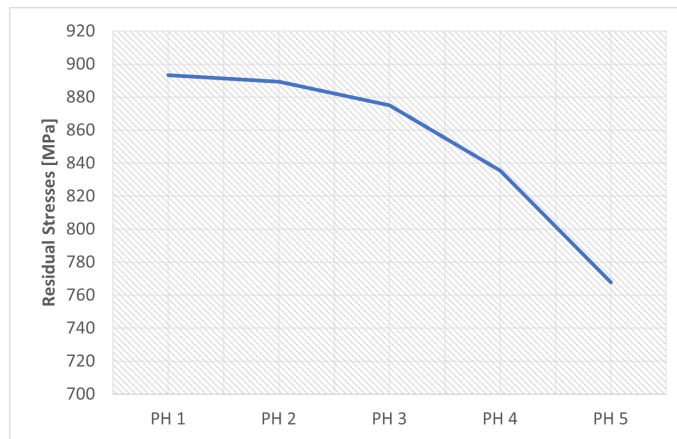


Figure 4.14: Results of the parametric study of the preheat temperature variation: Residual Stresses

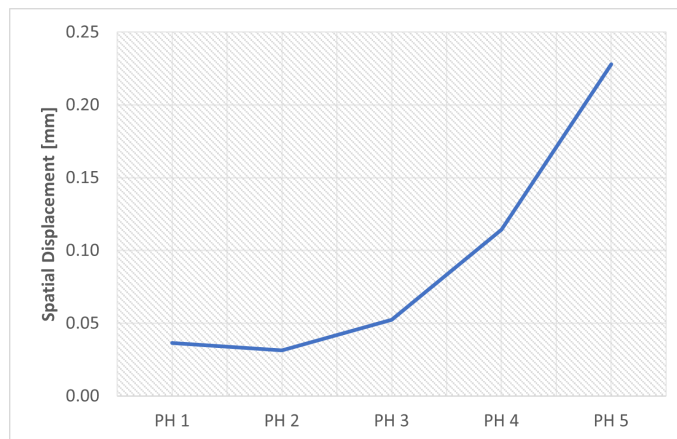


Figure 4.15: Results of the parametric study of the preheat temperature variation: Spatial Displacement

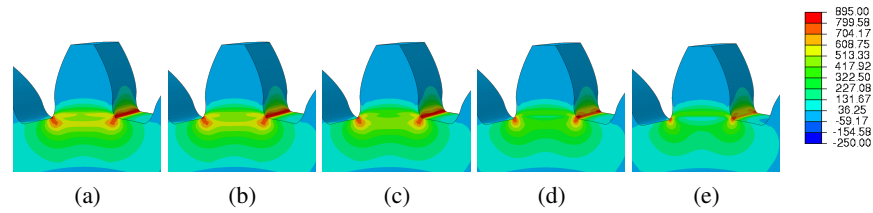


Figure 4.16: Preheat temperature - Residual Stress: (a) Ph-1 (b) Ph-2 (c) Ph-3 (d) Ph-4 (e) Ph-5

The images taken from Abaqus and grouped in Figure 4.17 illustrate the wide range of results obtained. For low preheat temperatures the spatial displacement is low (blue mark), on the other hand, for high preheat temperatures there is a high spatial displacement (red mark).

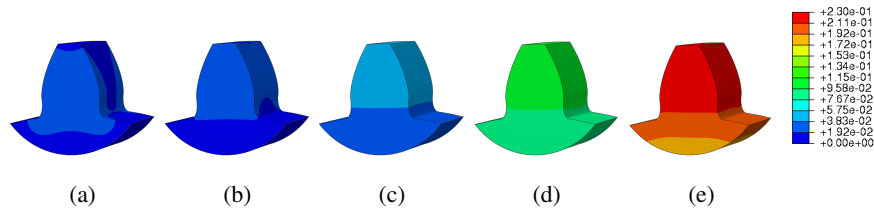


Figure 4.17: Preheat temperature - Spatial displacement: (a) Ph-1 (b) Ph-2 (c) Ph-3 (d) Ph-4 (e) Ph-5

4.2.4 Time step influence

The results obtained from the step time variation are now presented in Table 4.4 and in Figure 4.18. The study of this parameter aims to study the influence of step time on the results obtained in the simulation.

Table 4.4: Results of the step time variation

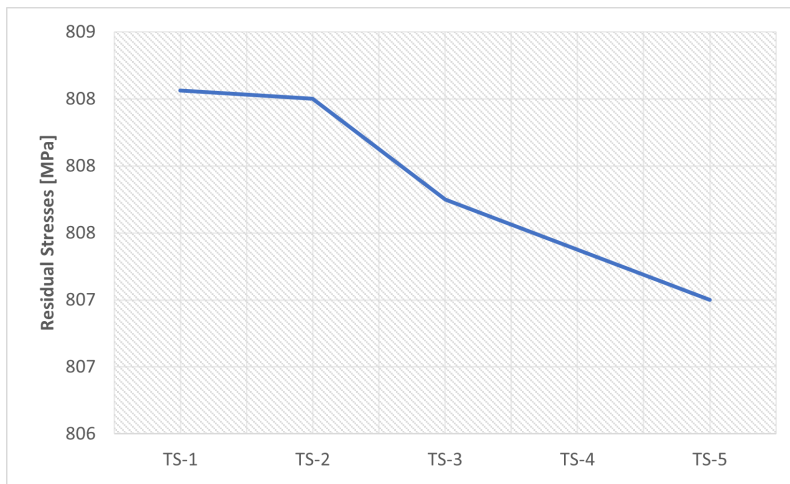
	Spatial Displacement [mm]	Residual Stresses [MPa]	Initial Increment	Max. increment
TS-1	3.53E-02	808.45	5.00	15.0
TS-2	3.33E-02	808.40	1.00	6.0
TS-3	3.29E-02	807.80	0.50	3.0
TS-4	3.28E-02	807.50	0.10	1.5
TS-5	3.23E-02	807.20	0.05	0.3

The time step is a parameter that influences the activation of the elements, so if the chosen step time is higher more elements will be active at once, which reduces the quality of the process simulation and consequently decreases the quality of the results obtained. Therefore, it is expected that

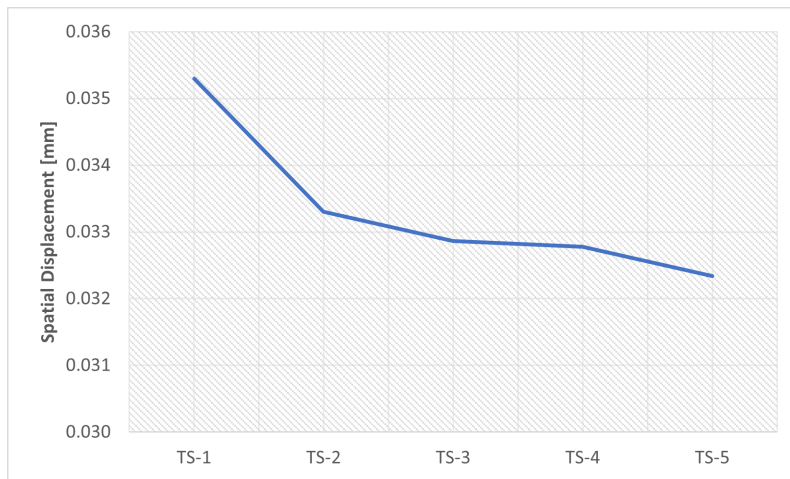
simulations with high time step values present less accurate results in counter-match simulations with lower time steps will present more accurate results.

Five simulations were performed, varying only the initial increment and maximum increment, the total step time is 60. Analyzing the results obtained, Figure 4.18, it is possible to verify that despite the significant variation of the parameters there is no significant difference in the results. Spatial displacement variation was approximately 8.4% however residual stress variation was less than 0.2%.

Note that the graphs in Figure 4.18 are on a custom scale to be able to see the small differences between the simulations.



(a)



(b)

Figure 4.18: Results of the parametric study of the step time variation: (a) Residual Stresses (b) Spatial Displacement

In the figure 4.19 is the graphic evolution of the simulations obtained through the variation of the time step. As can be seen, there is no significant difference.

In turn, in the figure 4.20 is the graphic evolution of the spatial displacement variation. Here,

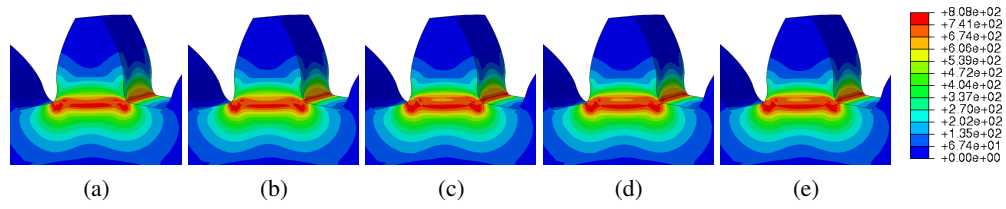


Figure 4.19: Time step influence - Residual Stress: (a) TS-1 (b) TS-2 (c) TS-3 (d) TS-4 (e) TS-5

there are no significant changes either, there is only a small decrease in the red spot (indicating higher spatial displacement values) as the time step decreases.

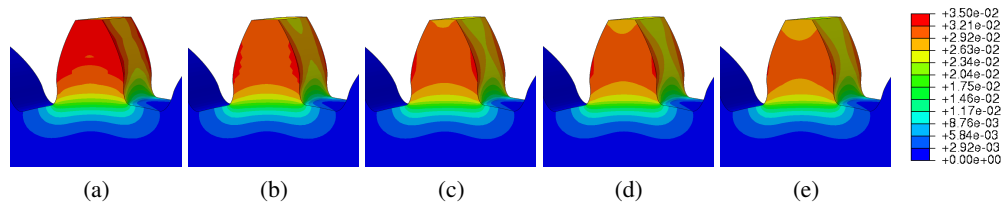


Figure 4.20: Time step influence - Spatial displacement: (a) TS-1 (b) TS-2 (c) TS-3 (d) TS-4 (e) TS-5

Although there is no significant difference in the results obtained from residual stresses and spatial displacements, the same does not happen with the CPU time values of the five simulations performed. By analyzing Figure 4.21, it can be seen that the smaller the increment used, the greater the computation time required.

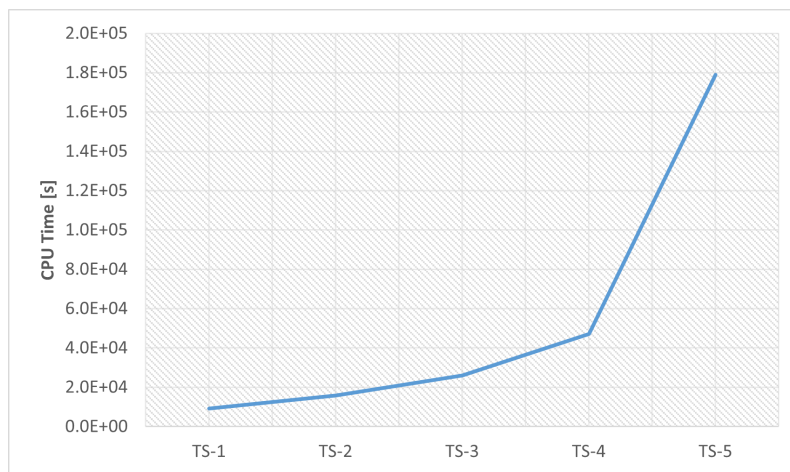


Figure 4.21: CPU time in incrementation time simulations

4.2.5 Material

In this section, two different materials were used for tooth reconstruction; IN625 and Maraging steel. To obtain reference values to analyze the evolution of residual stresses, it was first assumed that the gear and the reconstructed tooth were made of the same material. Subsequently, it was considered that the gear was made of 42CrMo4 and the tooth was made of IN625 or Maraging steel, as shown in Figure 3.20.

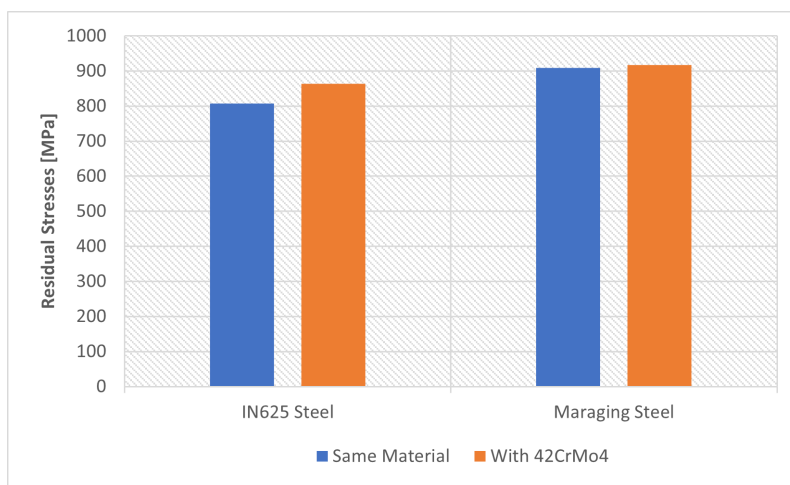


Figure 4.22: Material influence in Residual Stress

The figures 4.22 and 4.23 show the values obtained for the use of different materials. With the use of different materials, it is expected that there will be a discontinuity of properties and so the residual stresses will be higher. Note that the residual stresses in the gear are always concentrated at the root of the tooth, so with the use of different materials, the stresses will be even higher.

Analyzing the values in Figure 4.22, relative to the residual stresses induced by the DED process, it can be seen that stresses increase when different materials are used. However, this increase when using 42CrMo4 steel in the gear base is not very significant.

The results obtained for spatial displacement, figure 4.23, show a significant reduction when using 42CrMo4 steel. This reduction is more accentuated when Maraging steel is used, this may be related to the different thermal expansion of the materials.

One of the causes of this difference is that Maraging steel is more sensitive to temperature variation than 42CrMo4 steel, as can be seen in the properties tables 3.6 and 3.9, respectively.

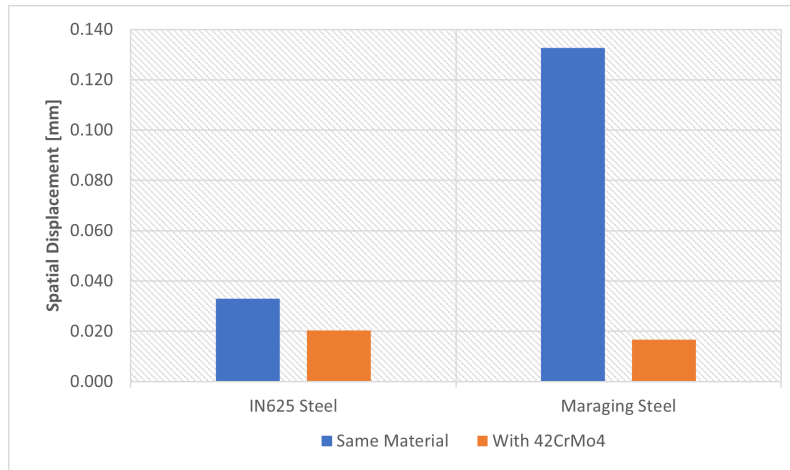


Figure 4.23: Material influence in spatial displacement

In Figures 4.24 and 4.25 it is possible to see the images obtained from the simulations carried out to study the influence of different materials on residual stresses and spatial displacement. In these figures, IN625 and 42CrMo4 steels were used.

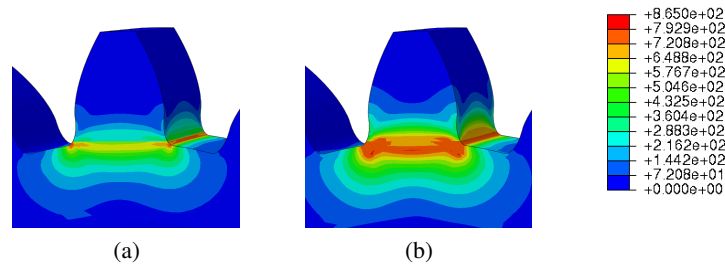


Figure 4.24: Material influence simulation residual stresses results: (a) IN625 (b) IN625 with 42CrMo4 steel

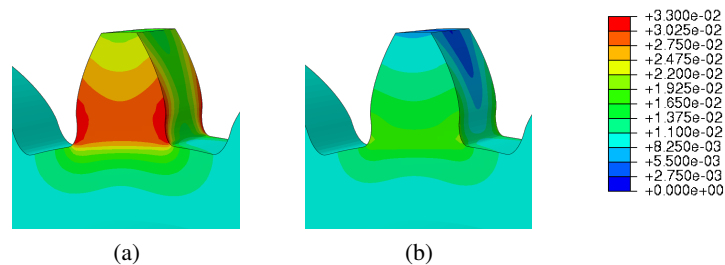


Figure 4.25: Material influence simulation spatial displacement results: (a) IN625 (b) IN625 with 42CrMo4 steel

In Figure, 4.24 it can be seen that the use of different materials increases the residual stresses at the root of the tooth. This increase can be seen through the increase in the reddish spot.

On other hand, the spatial displacement decreases as can be seen in Figure 4.25.

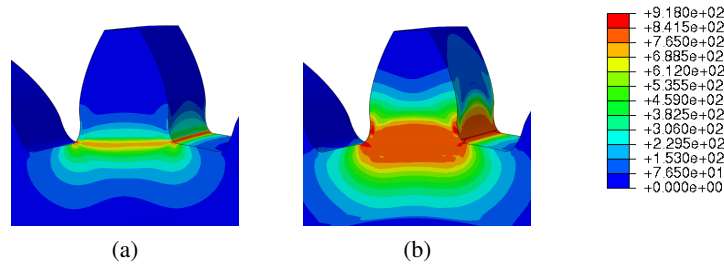


Figure 4.26: Material influence simulation residual stresses results: (a) Maraging Steel (b) Maraging steel with 42CrMo4 steel

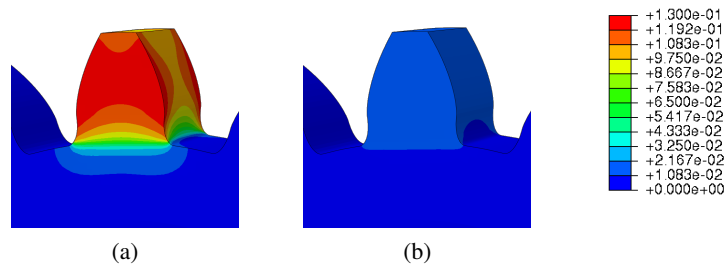


Figure 4.27: Material influence simulation spatial displacement results: (a) Maraging Steel (b) Maraging with 42CrMo4 steel

The results obtained with maraging and 42crmo4 steels, Figures 4.26 and 4.27 are similar to those obtained with IN625.

4.2.6 Deformation Factor

The images presented in this section, Figure 4.28, are a complement to understand more clearly how the deposited tooth deforms.

In Figure 4.28, several scale factors are represented in ascending order to be more visually perceptible the way the tooth is deformed. Five scale factors were used: 0, 25, 50, 75, and 100. As the scale factor increases, it becomes more evident that it tends to contract.

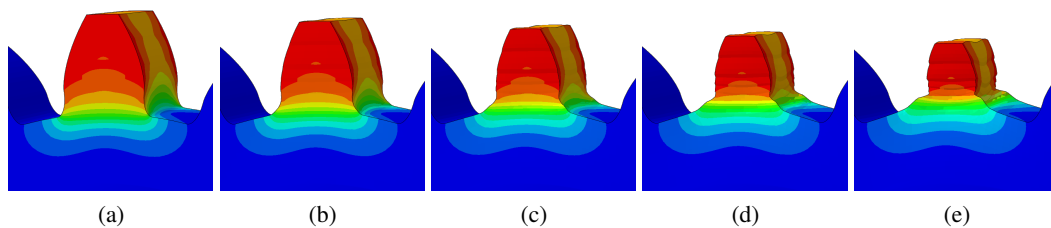


Figure 4.28: Deformation Scale Factor: (a) 0; (b) 25; (c) 50; (d) 75; (e) 100

Chapter 5

Conclusions

5.1 Results

The DED and PBF processes are the predominant technologies used worldwide and in Portugal, for that reason it is important to study the mechanical behavior of the parts obtained by these two processes. In this way, the use of numerical simulations becomes a very important tool to predict the distortions and residual stresses present in the produced parts.

The construction of numerical models for two AM processes took a long time since a large number of conditional variables necessitated a high number of simulation runs to improve the model as much as possible before properly analyzing the final findings.

Regarding the NIST Bridge benchmark, the objective initially set was achieved since the results obtained in the simulations were similar to the results measured experimentally. The case of the benchmark bridge was also a way of verifying and validating the work developed. In this first phase of the development of this work, the python script used to clean the Gcode file, to obtain the Event Series was improved. Obtaining the event series is important to correctly define the scanning strategy of the piece. The validation of the model developed for the NIST case was an important step to confidently advance to the parametric study of gear repair.

In the second phase of the work, the focus turned to the parametric study of the use of the DED process in gear repair. This study was motivated by the GEAR3D project. The objectives outlined for this project were also practically all achieved. The study of different parameters of the simulation was important to understand their influence on the simulations.

Despite the many parameters existing in the DED process, it was only possible to analyze five parameters: the influence of mesh refinement, scanning strategy, preheating temperature, step time, and the use of different materials.

The choice of mesh for the remaining simulations requires a compromise between the computational cost and the accuracy of the results obtained. The chosen mesh allows to obtain good

results with a relatively low computational cost, with a reduction of almost 94% when compared to other meshes.

Although the scanning strategies chosen only differed in the deposition angle, it was possible to conclude that the choice of an appropriate scanning strategy allows reducing residual stresses in 22.7% and therefore optimizes the part manufacturing process.

This parametric study allowed also to conclude that the preheating temperature is a parameter that strongly influences the values of residual stresses induced in the manufactured part. However, it is important to bear in mind that increasing the temperature significantly increases spatial displacement.

Regarding the study of the step time influence, there were no significant differences in the results obtained, mainly in the residual stresses. These results did not correspond well to what was expected, so a more detailed analysis could be carried out to understand the progressive activation of the material and its influence on the results.

Finally, taking into account the results obtained for the influence of the use of different materials, it was possible to verify that the residual stresses actually change with the use of different materials. On the other hand, the spatial displacement decreases substantially. One of the reasons for this may be related to the different expansion coefficients of the materials. Another reason may be the incomplete characterization of the constitutive laws of materials. Thus, it would be necessary to redo this simulation with well-defined constitutive models in order to be able to draw safe conclusions.

5.2 Further Work

For future work, there are several options that could be considered to consolidate the work carried out.

The experimental validation of the results obtained in the parametric simulation of the gear is very important to confirm or refute the developed models. For this, it would be necessary to compare the measurements of distortion and residual stresses obtained experimentally with the numerical results obtained.

Another aspect to be taken into account is the measurement of residual stresses. Using the von Mises criterion, the stresses obtained are always positive, which does not allow us to know whether they are in compression or in tension. In the design context, it is very important to know if the stresses are in compression or in tension, that is if they have a negative or positive sign. One of the future works could take this aspect into consideration.

Taking into account the possible phase changes that may occur in materials can be another aspect to be analyzed.

As already mentioned, another future work may involve the complete definition of constitutive models of materials, taking into account the variation of properties with temperature. In addition, also define the physical and thermal properties.

Perform a structural analysis for a fatigue load taking into account previous manufacturing stresses.

Post-processing by machining was not accounted for in the modeling but it must be accounted for in a proper evaluation of surface and subsurface residual stresses.

Bibliography

- [1] T. J. Horn and D. O. L. A. Harrysson, “Overview of current additive manufacturing technologies and selected applications,” *Science Progress*, vol. 95, no. 3, pp. 255–282, 2012. DOI: [10.3184/003685012X13420984463047](https://doi.org/10.3184/003685012X13420984463047). eprint: <https://doi.org/10.3184/003685012X13420984463047>. [Online]. Available: <https://doi.org/10.3184/003685012X13420984463047>.
- [2] National Institute of Standards and Technology, <https://www.nist.gov/>, Apr. 2022.
- [3] S. Group, *Gear3d: Reconstrução 3d de dentes de engrenagens de grande dimensão via deposição direta por laser*, <https://www.sermec2.pt/docs/ficha-projeto-idt-gear3d.pdf>, Jul. 2022.
- [4] INEGI, *Gear 3d project*, <https://www.inegi.pt/en/news/3d-metallic-printing-breathes-new-life-into-wind-turbine-gears/>, Apr. 2022.
- [5] D. Gu, W. Meiners, K. Wissenbach, and R. Poprawe, “Laser additive manufacturing of metallic components: Materials, processes and mechanisms,” English, *International Materials Reviews*, vol. 57, no. 3, pp. 133–164, 2012, ISSN: 17432804. DOI: [10.1179/1743280411Y.0000000014](https://doi.org/10.1179/1743280411Y.0000000014).
- [6] B. Dutta, S. Babu, and B. Jared, “Metal additive manufacturing,” in *Science, Technology and Applications of Metals in Additive Manufacturing*, Elsevier, 2019, ISBN: 978-0-12-816634-5. DOI: <https://doi.org/10.1016/B978-0-12-816634-5.00013-3>. [Online]. Available: <https://www.sciencedirect.com/science/article/pii/B9780128166345000133>.
- [7] I. O. for Standardization, *Additive Manufacturing – General principles – Terminology*, ISO 52900:2021. International Organization for Standardization, 2021. [Online]. Available: <https://www.iso.org/standard/74514.html>.
- [8] I. Gibson, D. Rosen, and B. Stucker, *Additive Manufacturing Technologies 3D Printing, Rapid Prototyping, and Direct Digital Manufacturing / by Ian Gibson, David Rosen, Brent Stucker*. 2nd ed. 2015. Springer New York : Imprint: Springer, 2015, ISBN: 1-4939-2112-6.
- [9] GAO, *Defense additive manufacturing*, <https://www.gao.gov/products/gao-16-56>, Jun. 2022.
- [10] Mesago Messe Frankfurt GmbH, <https://corporate.mesago.com>, May 2022.

- [11] N. Aamer, A. K. Mekonen, K. Ajeet, and J. Jeng-Ywan, “A state-of-the-art review on types, design, optimization, and additive manufacturing of cellular structures,” *The International Journal of Advanced Manufacturing Technology*, vol. 104, pp. 3489–3510, 2019, ISSN: 1433-3015. DOI: [10.1007/s00170-019-04085-3](https://doi.org/10.1007/s00170-019-04085-3). [Online]. Available: <https://doi.org/10.1007/s00170-019-04085-3>.
- [12] J. O. Milewski, *Additive Manufacturing of Metals: From Fundamental Technology to Rocket Nozzles, Medical Implants, and Custom Jewelry* (Springer series in materials science). Springer International Publishing AG, 2017, vol. 258, ISBN: 9783319582047.
- [13] M. Abdel Wahab, *Additive Manufacturing Handbook: Product Development for the Defense Industry*, 1st. CRC Press, 2017, p. 938, ISBN: 9781482264081. DOI: <https://doi.org/10.1201/9781315119106>.
- [14] W. J. Sames, F. A. List, S. Pannala, R. R. Dehoff, and S. S. Babu, “The metallurgy and processing science of metal additive manufacturing,” *International Materials Reviews*, vol. 61, no. 5, pp. 315–360, 2016. DOI: [10.1080/09506608.2015.1116649](https://doi.org/10.1080/09506608.2015.1116649). [Online]. Available: <https://doi.org/10.1080/09506608.2015.1116649>.
- [15] A. Selema, M. Ibrahim, and P. Sergeant, “Metal additive manufacturing for electrical machines: Technology review and latest advancements,” *Energies*, vol. 15, Jan. 2022. DOI: [10.3390/en15031076](https://doi.org/10.3390/en15031076).
- [16] Synergy Additive Manufacturing, LLC., <https://synergyadditive.com/>, Apr. 2022.
- [17] Sciaky Inc., <https://www.sciaky.com/>, Apr. 2022.
- [18] N. Eliaz, N. Foucks, D. Geva, *et al.*, “Comparative quality control of titanium alloy ti–6al–4v, 17–4 ph stainless steel, and aluminum alloy 4047 either manufactured or repaired by laser engineered net shaping (lens),” *Materials*, vol. 13, no. 18, 2020, ISSN: 1996-1944. DOI: [10.3390/ma13184171](https://doi.org/10.3390/ma13184171). [Online]. Available: <https://www.mdpi.com/1996-1944/13/18/4171>.
- [19] D. Svetlizky, M. Das, B. Zheng, *et al.*, “Directed energy deposition (ded) additive manufacturing: Physical characteristics, defects, challenges and applications,” *Materials Today*, vol. 49, pp. 271–295, 2021, ISSN: 1369-7021. DOI: <https://doi.org/10.1016/j.mattod.2021.03.020>. [Online]. Available: <https://www.sciencedirect.com/science/article/pii/S1369702121001139>.
- [20] J. J. Lewandowski and M. Seifi, “Metal additive manufacturing: A review of mechanical properties,” *Annual Review of Materials Research*, vol. 46, no. 1, pp. 151–186, 2016. DOI: [10.1146/annurev-matsci-070115-032024](https://doi.org/10.1146/annurev-matsci-070115-032024). [Online]. Available: <https://doi.org/10.1146/annurev-matsci-070115-032024>.
- [21] Beamit Group, <https://www.beam-it.eu/>, Apr. 2022.
- [22] Relativity, <https://www.relativityspace.com/>, Apr. 2022.

- [23] EOS GROUP, <https://www.eos.info/en>, Apr. 2022.
- [24] L. E. Murr, S. M. Gaytan, E. Martinez, F. Medina, and R. B. Wicker, “Next generation orthopaedic implants by additive manufacturing using electron beam melting,” *International Journal of Biomaterials*, vol. 2012, p. 14, 2012. DOI: [10.1155/2012/245727](https://doi.org/10.1155/2012/245727). [Online]. Available: <https://doi.org/10.1155/2012/245727>.
- [25] Bathsheba Sculpture LLC, <https://www.bathsheba.com/>, Apr. 2022.
- [26] I. Optomec, *Optomec - production equipment and digital solutions for the additive age*, <https://optomec.com/>, Sep. 2022.
- [27] Sennheiser electronic GmbH & Co. KG, <https://en-us.sennheiser.com/ie-600>, Apr. 2022.
- [28] X. Chen and Y. Liu, *Finite Element Modeling and Simulation with ANSYS Workbench*, 2nd ed. CRC Press, 2018, p. 471. DOI: <https://doi.org/10.1201/9781351045872>.
- [29] N. An, G. Yang, K. Yang, J. Wang, M. Li, and J. Zhou, “Implementation of abaqus user subroutines and plugin for thermal analysis of powder-bed electron-beam-melting additive manufacturing process,” *Materials Today Communications*, vol. 27, p. 102 307, 2021, ISSN: 2352-4928. DOI: <https://doi.org/10.1016/j.mtcomm.2021.102307>. [Online]. Available: <https://www.sciencedirect.com/science/article/pii/S2352492821002993>.
- [30] T. Mura, “General theory of eigenstrains,” in *Micromechanics of defects in solids*. Dordrecht: Springer Netherlands, 1987, pp. 1–73, ISBN: 978-94-009-3489-4. DOI: [10.1007/978-94-009-3489-4_1](https://doi.org/10.1007/978-94-009-3489-4_1). [Online]. Available: https://doi.org/10.1007/978-94-009-3489-4_1.
- [31] D. systemes, *Additive manufacturing process simulation*, <https://help.3ds.com/2022x/english/dsdoc/SIMA3DXANLRefMap/simaanl-c-amabout.htm?contextscope=cloud&id=72c7961c2f704c68a719193ba206587d>, Jun. 2022.
- [32] P. Michaleris, *Minimization of Welding Distortion and Buckling: Modelling and Implementation*, 1st edition. Woodhead Publishing, 2011, p. 471, ISBN: 9781845696627.
- [33] Dassault Systèmes SE, <https://www.3ds.com/products-services/simulia/products/abaqus/>, Apr. 2022.
- [34] L. Zhang, E. W. Reutzel, and P. Michaleris, “Finite element modeling discretization requirements for the laser forming process,” English (US), *International Journal of Mechanical Sciences*, vol. 46, no. 4, pp. 623–637, Apr. 2004, ISSN: 0020-7403. DOI: [10.1016/j.ijmecsci.2004.04.001](https://doi.org/10.1016/j.ijmecsci.2004.04.001).
- [35] G. M. and M. P., *Thermo-mechanical modeling of additive manufacturing*. Butterworth-Heinemann, 2018, p. 275. DOI: <https://doi.org/10.1016/C2016-0-00317-0>.

- [36] P. Michaleris, L. Zhang, S. R. Bhide, and P. Marugabandhu, "Evaluation of 2d, 3d and applied plastic strain methods for predicting buckling welding distortion and residual stress," *Science and Technology of Welding and Joining*, vol. 11, no. 6, pp. 707–716, 2006. DOI: [10.1179/174329306X147724](https://doi.org/10.1179/174329306X147724). [Online]. Available: <https://doi.org/10.1179/174329306X147724>.
- [37] T. Mura, *Micromechanics of defects in solids*. Springer Science & Business Media, 2013.
- [38] M. Bugatti and Q. Semeraro, "Limitations of the inherent strain method in simulating powder bed fusion processes," *Additive Manufacturing*, vol. 23, pp. 329–346, 2018, ISSN: 2214-8604. DOI: <https://doi.org/10.1016/j.addma.2018.05.041>. [Online]. Available: <https://www.sciencedirect.com/science/article/pii/S2214860417302877>.
- [39] Progressive Element Activation, <https://help.3ds.com/2022x/english/dsdoc/SIMA3DXANLRefMap/simaanl-c-elemactivation.htm?contextscope=cloud#simaanl-c-elemactivation>, Jun. 2022.
- [40] P. Michaleris, "Modeling metal deposition in heat transfer analyses of additive manufacturing processes," *Finite Elements in Analysis and Design*, vol. 86, pp. 51–60, 2014, ISSN: 0168-874X. DOI: <https://doi.org/10.1016/j.finel.2014.04.003>. [Online]. Available: <https://www.sciencedirect.com/science/article/pii/S0168874X14000584>.
- [41] M. Wierszycki, *Event series in abaqus*, https://www.linkedin.com/pulse/event-series-abaqus-marcin-wierszycki/?trk=pulse-article_more-articles_related-content-card, Jun. 2022.
- [42] Toolpath-Mesh Intersection - Abaqus, <https://help.3ds.com/2022x/english/dsdoc/SIMA3DXANLRefMap/simaanl-c-amtoolpathmeshintersect-toolpath-rep.htm?contextscope=cloud&id=bd19327f20184a1ab8f3040d19ffcf89>, Jun. 2022.
- [43] Point Toolpath-Mesh Intersection, <https://help.3ds.com/2022x/english/dsdoc/SIMA3DXANLRefMap/simaanl-c-amtoolpathmeshintersect-point-toolpath.htm?contextscope=cloud&id=ad22eb7ecb7b4a8ba5066a17a87a-ecd5>, Jun. 2022.
- [44] Infinite Line Toolpath-Mesh Intersection, <https://help.3ds.com/2022x/english/dsdoc/SIMA3DXANLRefMap/simaanl-c-amtoolpathmeshintersect-infinite-line-toolpath.htm?contextscope=cloud&id=12711f0d6b404874a0b0b-cc7c03b138a>, Jun. 2022.
- [45] Box Toolpath-Mesh Intersection, <https://help.3ds.com/2022x/english/dsdoc/SIMA3DXANLRefMap/simaanl-c-amtoolpathmeshintersect-box-toolpath.htm?contextscope=cloud&id=2f1724e631e443efb1c5ae4d4d3e-2f99>, Jun. 2022.

- [46] M. Pagac, J. Hajnys, R. Halama, *et al.*, “Prediction of model distortion by fem in 3d printing via the selective laser melting of stainless steel aisi 316l,” *Applied Sciences*, vol. 11, no. 4, 2021, ISSN: 2076-3417. DOI: [10.3390/app11041656](https://doi.org/10.3390/app11041656). [Online]. Available: <https://www.mdpi.com/2076-3417/11/4/1656>.
- [47] COMSOL Inc., <https://www.comsol.com/>, Apr. 2022.
- [48] P. J. Withers, “Residual stress and its role in failure,” *Reports on Progress in Physics*, vol. 70, no. 12, pp. 2211–2264, Nov. 2007. DOI: [10.1088/0034-4885/70/12/r04](https://doi.org/10.1088/0034-4885/70/12/r04). [Online]. Available: <https://doi.org/10.1088/0034-4885/70/12/r04>.
- [49] F. A. Kandil, J. D. Lord, A. T. Fry, and P. V. Grant, “A review of residual stress measurement methods - a guide to technique selection,” Teddington, NPL Report, Feb. 2001. [Online]. Available: <http://eprintpublications.npl.co.uk/1873/>.
- [50] P. Withers and H. Bhadeshia, “Residual stress. part 2 – nature and origins,” *Materials Science and Technology*, vol. 17, no. 4, pp. 366–375, 2001. DOI: [10.1179/026708301101510087](https://doi.org/10.1179/026708301101510087). [Online]. Available: <https://doi.org/10.1179/026708301101510087>.
- [51] J. L. Bartlett and X. Li, “An overview of residual stresses in metal powder bed fusion,” *Additive Manufacturing*, vol. 27, pp. 131–149, 2019, ISSN: 2214-8604. DOI: <https://doi.org/10.1016/j.addma.2019.02.020>. [Online]. Available: <https://www.sciencedirect.com/science/article/pii/S221486041930051X>.
- [52] N. Rossini, M. Dassisti, K. Benyounis, and A. Olabi, “Methods of measuring residual stresses in components,” *Materials & Design*, vol. 35, pp. 572–588, 2012, New Rubber Materials, Test Methods and Processes, ISSN: 0261-3069. DOI: <https://doi.org/10.1016/j.matdes.2011.08.022>. [Online]. Available: <https://www.sciencedirect.com/science/article/pii/S0261306911005887>.
- [53] G. M. A. A., M. Asmael, and Z. Qasim, “Recent applications of residual stress measurement techniques for fsw joints: A review,” *Jurnal Kejuruteraan*, vol. 32, no. 3, pp. 357–371, 2020, ISSN: 0128-0198. DOI: [https://doi.org/10.17576/jkukm-2020-32\(3\)-01](https://doi.org/10.17576/jkukm-2020-32(3)-01). [Online]. Available: <https://www.ukm.my/jkukm/volume-323-2020/>.
- [54] X. Huang, Z. Liu, and H. Xie, “Recent progress in residual stress measurement techniques,” *Acta Mechanica Solida Sinica*, vol. 26, no. 6, pp. 570–583, 2013, ISSN: 0894-9166. DOI: [https://doi.org/10.1016/S0894-9166\(14\)60002-1](https://doi.org/10.1016/S0894-9166(14)60002-1). [Online]. Available: <https://www.sciencedirect.com/science/article/pii/S0894916614600021>.
- [55] M. Peter, “Residual stresses in selective laser sintering and selective laser melting,” *Rapid Prototyping Journal*, vol. 12, pp. 254–265, 2006, ISSN: 1355-2546. [Online]. Available: <https://www.emerald.com/insight/content/doi/10.1108/13552540610707013/full/html>.

- [56] Y. Yang, M. Allen, L. Tyler, and O. Victor, "Residual strain predictions for a powder bed fusion inconel 625 single cantilever part," *Integrating Materials and Manufacturing Innovation*, vol. 8, 2019, ISSN: 2193-9772. DOI: [10.1007/s40192-019-00144-5](https://doi.org/10.1007/s40192-019-00144-5).
- [57] Special Metals Corporation, <https://www.specialmetals.com/>, May 2022.
- [58] J. Costes, Y. Guillet, G. Poulachon, and M. Dessoly, "Tool-life and wear mechanisms of cbn tools in machining of inconel 718," *International Journal of Machine Tools and Manufacture*, vol. 47, no. 7, pp. 1081–1087, 2007, ISSN: 0890-6955. DOI: <https://doi.org/10.1016/j.ijmactools.2006.09.031>. [Online]. Available: <https://www.sciencedirect.com/science/article/pii/S0890695506002586>.
- [59] E. A. Jäggle, Z. Sheng, P. Kürnstener, S. Ocylok, A. Weisheit, and D. Raabe, "Comparison of maraging steel micro- and nanostructure produced conventionally and by laser additive manufacturing," *Materials (Basel, Switzerland)*, vol. 10, 2017, ISSN: 1996-1944. DOI: <https://doi.org/10.3390/ma10010008>.
- [60] X. Jijin, G. Philippe, D. Yonggang, and Y. Chun, "Temperature and residual stress simulations of the net single-bead-on-plate specimen using sysweld.," *International Journal of Pressure Vessels and Piping*, pp. 51–100, 2012.
- [61] L. Schwer, "Optional strain-rate forms for the johnson cook constitutive model and the role of the parameter epsilon_0," in *6th European LS_DYNA Users' conference*, 2007, pp. 1–17.
- [62] P. I, "Finite element modeling of the behavior of armor materials under high strain rates and large strains.," *Theory of Computing Systems Mathematical Systems Theory*, 2010.
- [63] M. Supermarkets, *Aisi 4140 steel composition*, <https://www.metalsupermarkets.com/grade-guide-4140-steel/>, Sep. 2022.
- [64] T. world material, *Sae aisi 4140 steel properties*, <https://www.theworldmaterial.com/astm-sae-aisi-4140-steel/>, Sep. 2022.
- [65] O. Pantalé, J.-L. Bacaria, O. Dalverny, R. Rakotomalala, and S. Caperaa, "2d and 3d numerical models of metal cutting with damage effects," *Computer Methods in Applied Mechanics and Engineering*, vol. 193, no. 39, pp. 4383–4399, 2004, ISSN: 0045-7825. DOI: <https://doi.org/10.1016/j.cma.2003.12.062>. [Online]. Available: <https://www.sciencedirect.com/science/article/pii/S0045782504002269>.
- [66] V. I. Bartosz Gapiński Marek Szostak, *Lecture Notes in Mechanical Engineering*. Springer Cham, 2019, p. 653, ISBN: 978-3-030-16942-8. DOI: <https://doi.org/10.1007/978-3-030-16943-5>.
- [67] D. systemes, *Thermomechanical simulation of additive manufacturing processes*, <https://help.3ds.com/2022x/english/dsdoc/SIMA3DXANLRefMap/simaan1-c-amthermomechanical.htm?contextscope=cloud&id=adcdef5afb60447aa9-99ef7116c07413>, Jun. 2022.

- [68] H. Jia, H. Sun, H. Wang, Y. Wu, and H. Wang, "Scanning strategy in selective laser melting (slm): A review," *The International Journal of Advanced Manufacturing Technology*, vol. 113, no. 2, 2021/04/01, ISSN: 1433-3015. DOI: [10.1007/s00170-021-06810-3](https://doi.org/10.1007/s00170-021-06810-3). [Online]. Available: <https://doi.org/10.1007/s00170-021-06810-3>.
- [69] B. AlMangour, D. Grzesiak, and J.-M. Yang, "Scanning strategies for texture and anisotropy tailoring during selective laser melting of tic/316l stainless steel nanocomposites," *Journal of Alloys and Compounds*, vol. 728, pp. 424–435, 2017, ISSN: 0925-8388. DOI: <https://doi.org/10.1016/j.jallcom.2017.08.022>. [Online]. Available: <https://www.sciencedirect.com/science/article/pii/S0925838817327494>.
- [70] D. Koutny, D. Palousek, L. Pantelejev, *et al.*, "Influence of scanning strategies on processing of aluminum alloy en aw 2618 using selective laser melting," *Materials*, vol. 11, no. 2, 2018, ISSN: 1996-1944. DOI: [10.3390/ma11020298](https://doi.org/10.3390/ma11020298). [Online]. Available: <https://www.mdpi.com/1996-1944/11/2/298>.
- [71] K. Kempen, B. Vrancken, S. Buls, L. Thijs, J. Van Humbeeck, and J.-P. Kruth, "Selective Laser Melting of Crack-Free High Density M2 High Speed Steel Parts by Baseplate Preheating," *Journal of Manufacturing Science and Engineering*, vol. 136, no. 6, Oct. 2014, 061026, ISSN: 1087-1357. DOI: [10.1115/1.4028513](https://doi.org/10.1115/1.4028513). [Online]. Available: <https://doi.org/10.1115/1.4028513>.
- [72] L. Caprio, A. G. Demir, G. Chiari, and B. Previtali, "Defect-free laser powder bed fusion of ti-48al-2cr-2nb with a high temperature inductive preheating system," *Journal of Physics: Photonics*, vol. 2, no. 2, p. 024001, Feb. 2020. DOI: [10.1088/2515-7647/ab7080](https://doi.org/10.1088/2515-7647/ab7080). [Online]. Available: <https://doi.org/10.1088/2515-7647/ab7080>.
- [73] P. T. Q., S. Maria, H. M. R., *et al.*, "Elastic residual strain and stress measurements and corresponding part deflections of 3d additive manufacturing builds of in625 am-bench artifacts using neutron diffraction, synchrotron x-ray diffraction, and contour method," *Integrating Materials and Manufacturing Innovation*, vol. 8, 2019, ISSN: 2193-9772. DOI: [10.1007/s40192-019-00149-0](https://doi.org/10.1007/s40192-019-00149-0). [Online]. Available: <https://doi.org/10.1007/s40192-019-00149-0>.
- [74] L. Liu, D. Wang, Y. Yang, *et al.*, "Effect of scanning strategies on the microstructure and mechanical properties of inconel 718 alloy fabricated by laser powder bed fusion," *Advanced Engineering Materials*, p. 2200492, 2022. DOI: <https://doi.org/10.1002/adem.202200492>. [Online]. Available: <https://onlinelibrary.wiley.com/doi/abs/10.1002/adem.202200492>.